A CFD Model for a Fixed Bed Reactor for Fischer Tropsch Reaction using Ansys

by

Vidushi Chitranshi

Submitted in partial fulfilment of the requirements for the degree of

Master of Science in Engineering (Chemical Engg.)

September 2022

Process Modelling and Optimisation Research Group
Department of Chemical Engineering
University of Cape Town
Rondebosch, 7701
Republic of South Africa

"I know the meaning of plagiarism and declare that all the work in the document, save for that which is properly acknowledged, is my own. This thesis/dissertation has been submitted to the Turnitin module (or equivalent similarity and originality checking software) and I confirm that my supervisor has seen my report and any concerns revealed by such have been resolved with my supervisor."

Signed by candidate

Vidushi Chitranshi

Abstract

Fischer-Tropsch (FT) is a process which can convert synthesis gas derived from natural gas, coal or even biomass to a variety of products including saturated and unsaturated hydrocarbon chains, while keeping the emission of greenhouse gases minimum.

Among various types of reactors used for commercial FT, fixed bed tubular reactors are among the most common type of reactor. However, there is a big challenge faced by these tubular reactors. FT is a highly exothermic process and therefore, heat removal in these reactors is needed to be highly efficient to avoid a thermal runaway.

To improve the heat transfer in any reactor, it is necessary to estimate the heat production correctly. Therefore, the kinetics in the FT system needs to correctly represent the heat transfer behaviour in the system. This requires an effective description of the reaction kinetics. FT is a polymerisation reaction, so the rate expressions must be able to retain the chain reaction behaviour. This is not possible with a lumped approach model which is used by most researchers in literature. Therefore, a partial equilibrium approach was employed, where thermodynamic and kinetic models were coupled, and the reaction rates depended on the concentration of reactants as well as products. The kinetic model employed in the current project was taken directly from the work of Davies and Möller, 2021b.

The abovementioned partial equilibrium kinetics was used to develop a CFD model for the FT reaction system. This model was reproduced using COCO simulator for a plug flow reactor for same operating conditions as Ansys to compare the results from both the softwares. The results showed a close agreement and hence, assured that the CFD model could be used for further testing.

The other challenge with the FT in FBRs is the heat dissipation. To avoid the thermal runaway, some innovations in reactor design have been studied in literature. In terms of heat transfer capabilities, when shell and tube heat exchangers are compared with the plate and frame heat exchangers, various sources in literature claim that the latter is found to be more effective. However, plate type reactors have not yet been explored in detail for their heat transfer capabilities. Taking an idea from this, the CFD model developed for the tubular reactors was adapted for plate type reactors. The heat transfer capabilities of the plate type reactors were compared relative to the tubular reactors.

The tube reactor and plate type reactor were compared on the basis of two criteria. One criterion was based on physical similarity between the reactors. It included having equal Reynolds Number and equal surface area available per unit volume for both type of reactors. For a plate with plate spacing t and a tube with diameter D, the latter condition resulted in the expression, D = 2t. The factors that Reynolds number for a packed bed depends on were all same for both the geometries, so by default, the Reynolds Number was

identical for both cases. The other criterion was based on catalyst packing. It included having equal tube-to-particle diameter ratio for both geometries.

For tube reactors, diameter is an important parameter that determines the heat dissipation behaviour, so a parametric study was carried out to study the effect of a diameter and plate spacing on heat transfer behaviour for the same set of operating conditions. It was found that the plate type reactor had a hotspot temperature which was less than the hotspot temperature of corresponding tube reactor at all plate spacings. This indicated that the heat dissipation in a plate type reactor is better than in the corresponding tube reactor.

Since the tube reactors observed higher temperatures than corresponding plate reactors, the CO conversion observed in the tube reactors was higher. When the product distributions for the two geometries were compared at isothermal conditions, the results almost overlapped for the two geometries. But when they were compared for non-isothermal conditions, significant differences were observed. This showed that heat dissipation mechanisms in the system had a huge role in bringing out different performances for the two geometries. Effect of temperature and conversion on the product distribution were also studied.

On the basis of tube to particle diameter ratio criterion, tube reactor was found to outperform the plate reactors in terms of temperature control when compared using the tube-to-particle diameter ratio. Therefore, the superiority of one reactor over the other was dependent on the criterion they are being compared for.

The plate type reactor was then represented in PFR model by tuning the heat transfer coefficient of the tubular model in COCO. The difference between the CO conversions achieved between the plate type reactor in Ansys and the representative model in COCO was found to be very little. Hence, the plate type reactor representation could be successfully achieved in COCO.

There can be a lot of further research that can be done using the current model. The areas of reaction kinetics and reactor design were highlighted in this regard. The current model can be extended to a larger number of species, for a better representation of the FT product spectrum. Formation of liquids was completely neglected in the current project. It can be taken into account as presence of liquid can affect the FT reactor system by imposing internal and external mass transfer limitations to the reactions. The current model can also be used to study the HTFT process and also to study the isomeric products in the LTFT which were assumed to be not present in the current project.

In the areas of reactor design, the geometry of catalyst particles can be included in the reactor geometry. This model can also be used for plates of other shapes and sizes to study the effect of shape and size on heat transfer capabilities. Different types of corrugated plates are used in the Plate and Frame Heat exchangers nowadays. The corrugations increase the surface area available and also increase mixing. Using the current model, such modifications can be studied for their effect on the reactions in a reactive system.

Acknowledgement

In the name of Almighty, Lord Vishnu and Sheetla Mata.

> " Do your duty without expecting returns"
>
> -(Shrimad Bhagvad Gita, Chapter 2, Verse 47)

I would like to give all the honour, praise, and gratitude to the omnipresent Lord Vishnu, to give me this opportunity to gain knowledge and become a better person. You have been my constant saviour since the beginning. It was not in my capacity to do this work and come this far without you. In my darkest times, you were the one who put me together when I was broken. This step of my life has strengthened my faith and belief in you.

Undertaking this masters has been a life-changing experience for me, and it would not have been possible to do so without the support and guidance that I received from many people.

First and foremost, I would like to express my gratitude to my supervisor, Prof. Klaus Möller for bringing forward the project to me. Thank you for all the guidance, help and advice. I cannot thank you enough for teaching me to always be hopeful. Your assurance and encouragement helped me steer through difficult times in this project. You know so much!!!

My gratitude extends to my co-supervisor Dr Ryno Laubscher for always being my support system when it came to CFD. I can't thank you enough for your invaluable supervision and tutelage. I have learnt a lot from you. I also thank you for providing the resources that I needed.

To my parents, Avadhesh and Nootan, who have always given me every opportunity in my life to grow and develop. You both inspire me to go ahead and fulfil my dreams. You have seen me through all and stood by me in all the situations. Thank you for all the physical, emotional, and financial support. To my little brother Sarthak, thank you for all the fun and laughter.

To my pseudo parents, Lloyd Mulder, and Lorna Mulder, thank you for being such awesome human beings. This masters project wasn't possible without you accepting me into your lives and taking care of me like your own daughter.

To my partner in crime, Teja, thank you for living this thesis with me. Your support and encouragement made working on this thesis each day worth it.

To my friend Milda, thank you for listening to all my problems in depth and providing valuable support. To Moya, thank you for all the guidance and warm hugs. To Mufaro, thank you for being my lockdown partner.

To my fellow chem. engg. researchers, Zafar and Qiang, thank you for the companionship.

To Imaad and Bongani, thank you for all the support. Your works have been very helpful.

Table of Contents

Nomenclature

P	Pressure
R	Universal Gas Constant
T	Temperature (°C)
Re	Reynolds Number (dimensionless)
y_i	mole fraction of specie in gas phase
d_p	pellet diameter (m)
r	inner tube diameter (m)
r_{CO}	rate of CO consumption
C_i	Molar Concentration of i^{th} component
f_i	Fugacity of i^{th} component
ρ_f	fluid density
u_f	fluid velocity
L	Reactor length (m)
G	Mass flow rate of Gas

Greek Letters

ε	void volume of the bed
μ	viscosity (kg/ (m.s))

List of Figures

List of Tables

Part 1. Introduction and Literature Review

1. Chapter – Introduction

1.1 Energy Crisis and Alternative Sources of Energy

One of the biggest challenges currently faced by engineers is balancing the energy demand-supply cycle of the world's increasing population while also strategically reducing the harmful effects of production of energy on our environment. Possible alternate sources of energy other than the conventional crude oil, have been enjoying a lot of attention from academic and industrial divisions from past few decades majorly because of increase in global energy demand, concern over environmental degradation, political instabilities in the regions producing oil, discovery of numerous gas reservoirs in remote areas and the high price of crude oil in comparison to natural gas (Chabot *et al.*, 2015). They seem a viable option because of their promising nature in enabling us to achieve energy security and preparing us for post-oil energy needs in the long run.

Natural gas seems an attractive option because of recent discoveries of large reserves. The global spread of natural gas is demographically dispersed, and a large portion of the world's reserve is deemed 'stranded' majorly because it is economically unviable to access the gas reserves (Lee, 2011). There has been a hike in number of attempts to develop technologies pertaining to CO conversion of unconventional sources of energy to automobile fuels after the oil crisis of 1973 (Kauchali, McGregor and Hildebrandt, 2000). The Shell Middle distillates is one such example.

Fischer-Tropsch (FT) is one such process which can convert synthesis gas derived from natural gas, coal or even biomass to a variety of products including saturated and unsaturated hydrocarbon chains and oxygenates while keeping the emission of greenhouse gases minimum. These hydrocarbon chains can then be further upgraded subsequently to obtain high-quality liquid fuels. *Figure 1-1* shows the commercial FT activities worldwide as of 2016.

1.2 Background of Fischer Tropsch Synthesis

CO conversion of natural gas derived syngas and coal derived syngas to synthetic fuels is also known as Gas-to-liquid (GTL) and Coal-to-liquid (CTL) technologies, respectively (Lozano-Blanco *et al.*, 2006; van Steen *et al.*, 2018 & Zijlstra *et al.*, 2020). *Figure 1-2* shows the process of CO conversion of natural gas, coal, biomass etc. to hydrocarbon fuels through a block flow diagram.

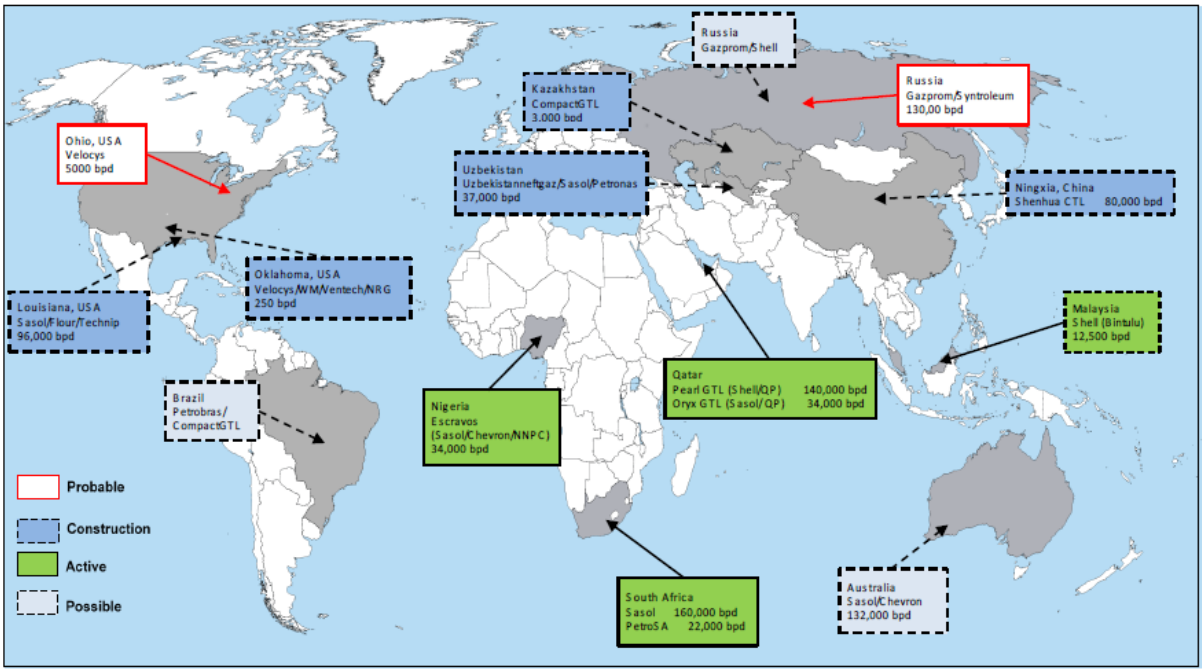

Figure 1-1: Commercial FT Activities worldwide as of 2016, Reproduced from: (Dry, 2002; Davis and Occelli, 2016)

FT processes usually include three main steps (Laan and Beenackers, 1999):

1. Production and purification of Syngas
2. FT synthesis
3. Product Upgradation

First step is the most expensive part of the process (Geerlings *et al.*, 1999; van Steen *et al.*, 2018). Therefore, the LTFT process should be designed such that maximum utilisation of syngas can be facilitated (Geerlings *et al.*, 1999).

LTFT follows a route of catalytic polymerisation converting natural gas derived or coal derived synthesis gas to linear and branched paraffins and α-olefins. The operating conditions for the LTFT are 180-260°C and 20-30 bar(a). Although the main products are a broad distribution of paraffins and olefins, significant amount of water is formed (Subiranas, 2008 & Saeidi *et al.*, 2015a). The oxygenates and the branched compounds constitute the side products. Their formation is favoured at higher pressures like 30-40 Bars (Andre and Dry, 2004).

The hydrocarbon fuels provided by Fischer Tropsch Synthesis (FTS) are known for their high cetane number and absence of environmentally harmful compounds like sulphur unlike the fuels obtained in the process of direct hydrogenation (Rofer-DePoorter, 1981).

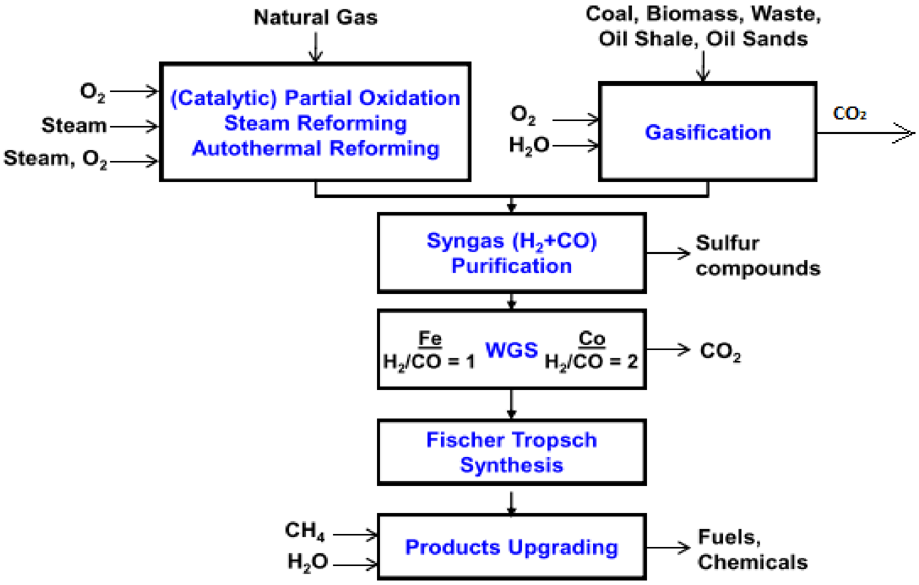

Figure 1-2: Overview of XTL process, Reproduced from: (Basha, 2016)

Fischer Tropsch is a highly exothermic process (ΔH_r = -170 kJ/mol_{CO}) and, hence, temperature control in a fixed bed FT reactor is a challenge. Heat removal from the reactor while operation is crucial because rise in the reactor temperature can lead to the over-heating of the catalyst particles which will result in the hot-spot formation, significant degradation of the catalyst activity and increased production of undesirable methane (Guettel, Kunz and Turek, 2008 & Dry, 2002).

1.3 Motivation and scope

The project derives its motivation from the literature review which follows in the next chapter.

The proposed 1D models in literature have neglected the resistance to heat and mass transfer in the radial direction and therefore have predicted uniform temperatures and CO conversions across the cross-section of the reactor. This is a serious simplification given that FT suffers from heat transfer inefficiencies (Jess and Kern, 2009).

While the 2D models have been developed, but by thoroughly reviewing the proposed CFD models, it can be understood that all such models do not follow chain reaction steps and therefore, are not able to represent the coupling between heat transfer and mass transfer. They have also overlooked the thermodynamics perspective to the FT kinetics.

Therefore, a comprehensive 2D model preserving the chain reaction behaviour of FT for the fixed bed reactor (FBR) does not exist. Such a model was developed in this project to get more realistic results for the FT reactor compared to conventional reactor models. It is expected that this work contributes to the enhancement of different existing models by adding insights about the heat transfer in a FBR.

Various reaction innovation designs have been proposed in literature to overcome the problem of thermal runaway in FBRs. A plate type reactor is one such innovation that can potentially enhance the heat transfer in an FB reactor. However, the behaviour of heat transfer in a plate type reactor has not been studied in detail in literature. In addition, excellent performance of plate type heat exchangers over shell and tube heat exchangers in terms of heat transfer abilities, as claimed by multiple sources in literature, gave a motivation for exploring the potential of plate type reactors for FTS and compare it to conventional tubular reactors. Therefore, the developed CFD model was used to conduct simulation studies to analyse temperature control in plate type reactors. To understand the importance of plate spacing and diameter for heat transfer aspect in a plate type reactor and tube reactor respectively, parametric studies were carried out for the same.

1.4 Aim and Objectives

The aim of the project is to compare Tube vs Plate geometry for their heat transfer capabilities and carry out a parametric study to explore how diameter and plate spacing affect the heat transfer in a plate type reactor and a tube reactor respectively, in an FBR for FTS.

The objectives include:

- Developing a steady state CFD model which is based on an approach that utilises the thermodynamics and the kinetics of the system in an integrated manner for a tubular geometry
- Comparing the obtained results with the results obtained through 1D mathematical models and accessing the reliability of the model
- Adapt the CFD model for a plate type geometry
- Compare heat transfer properties of a tubular geometry and a plate type geometry on the basis of surface area to volume ratio and tube to particle diameter ratio
- Carrying out a parametric study for the diameter of the tube reactor and plate spacing in the plate type reactor and compare the two cases

Furthermore, the CFD model developed in this work can serve as a basis for further research in modeling of various complex physical processes inside a FBR such as developing a geometry for the catalyst particles and taking account of the actual surface area available for the reactions to occur and/or considering the production of liquid phase into the system and simulating the vapor-liquid equilibrium.

2 Chapter – Literature Review

2.1 Modes of FT Operation

FT can be operated in the following two modes:

(1) **For maximising production of gasoline and linear low molecular mass olefins**: It is carried out at a temperature range of 300°-350° Celsius. It usually employs Iron based catalysts and is known as High Temperature Fischer Tropsch (HTFT).

(2) **For maximising production of high molecular mass Waxes**: It is carried out at a lower temperature range than HTFT. The temperature range is usually 200°-240° Celsius. It can employ either of Iron or Cobalt based catalysts and is known as Low-Temperature Fischer Tropsch (LTFT) (Dry, 2002).

Since the study was carried out to model a FBR to suit the production of long hydrocarbon chains, LTFT mode of operation was at focus.

2.2 FT Reactions

Although there have been numerous reaction mechanisms for the FT synthesis, it is well accepted that FTS is a polymerisation reaction consisting of a chain initiation, propagation, and termination steps. The chain initiation is facilitated by the methylene ($-CH_2-$) monomer.

The Fischer-Tropsch synthesis reactions comprise of hydrogenation of CO to give hydrocarbon and oxygenated products having various chain lengths. Water is a major product of these reactions. Water Gas shift reactions may also occur when there is significant catalyst activity or when there is low H_2/CO ratio present (Alba Mena Subiranas and Schaub, 2009; Rafiq *et al.*, 2011 & Bukur *et al.*, 2012).

The CO and H_2 molecules adsorb, dissociate on the surface of the catalyst, and undergo a series of steps to form ($-CH_2-$) monomer, initiator ($-CH_3-$) and water. The chain propagates with the addition of the ($-CH_2-$) monomer to the alkyl groups. The chain termination takes place when monomer ($-CH_2-$) inserts between the organometallic bond of the catalyst and then depending on the route followed i.e. hydrogenation or dehydrogenation, yields straight chain or branched paraffins or α-olefins respectively (Van Der Laan and Beenackers, 1999).

Main Reactions in the FTS are (Van Der Laan and Beenackers, 1999):

1. Paraffins	$nCO + (2n + 1)\ H_2 \longrightarrow C_nH_{2n+2} + nH_2O$
2. Olefins	$nCO + 2nH_2 \longrightarrow C_nH_{2n} + nH_2O$
3. Water Gas Shift (WGS)	$CO + H_2O \rightleftarrows CO_2 + H_2$

Side Reactions:

4. Alcohols	$nCO + 2nH_2 \longrightarrow C_nH_{2n+2}O + (n - 1)\ H_2O$
5. Catalyst oxidation/reduction	(a) $M_xO_y + yH_2 \longrightarrow yH_2O + xM$
	(b) $M_xO_y + yCO \longrightarrow yCO_2 + xM$
6. Bulk carbide formation	$yC + xM \rightleftarrows M_xC_y$
7. Boudouard reaction	$2CO \longrightarrow C + CO_2$

The water-gas shift reaction is usually considered for the iron catalysts and neglected for cobalt catalysts. Reactions 6 and 7 are undesired because of the carbon deposition which acts as a deactivation reaction and shifts the selectivity away from the higher hydrocarbons and renders safe reactor operation non-feasible. Reactions 1 and 2 have been considered in the current project and the rest are assumed to occur in negligible amounts and hence not considered here.

2.3 FT Catalysts

The catalysts generally used for Fischer Tropsch have Iron, Cobalt or Ruthenium as the active metal in them. Ruthenium is found to be the most effective metals as it is known to enhance the selectivity of higher paraffins. However, being super expensive makes it unattractive for commercial use (Subiranas, 2008).

The only used catalysts for industrial application are Iron(Fe) or Cobalt(Co) based. Out of Co and Fe, Cobalt-based catalysts are designed for maximum wax selectivity, and they are mainly used in fixed-bed reactors. Shell Middle Distillates Plant is one such example which utilises Cobalt-based catalysts for the Fischer Tropsch Reactions (Subiranas, 2008). The main reason behind preference for Cobalt-based catalysts is their high activity and low selectivity for oxygenates compared to the Iron counterparts (Botao *et al.*, 2007). K promoted Fe-based catalysts have a high activity for water gas shift reactions while Cobalt-based catalysts have negligible activity for the same (Jager and Espinoza, 1995). Due to these reasons, the current study was carried out using the Cobalt-based catalysts.

2.4 FT Reactors

There are two types of reactors majorly employed for FT process- Slurry Bubble Column Reactor (SBCR) and Tubular Fixed Bed Reactor (TFBR). Two other types of reactors, namely, Fluidised Bed Reactors and microchannel reactors are also used for FT but not at a commercial scale. The reasons are discussed below.

2.4.1 Fluidised Bed Reactors

Fluidised bed reactors are not suitable for LTFT because the formation of liquid phase products may cause particle agglomeration of catalyst particles which in turn hampers the fluidisation process in the reactor. These reactors are generally employed for HTFT processes where there is an absence of liquid phase. They are best suited for light alkanes rather than wax. They have an added advantage of excellent heat transfer and temperature equalisation characteristics which is important due to the large amounts of the heat that needs to be extracted in order to prevent formation of temperature hotspots (Lee, 2011)

2.4.2 Microchannel Reactors

Microchannel reactors are known for enabling usage of higher pressures, temperatures, and reactant concentrations due to their excellent heat transfer properties compared to the traditional ones (Saeidi *et al.*, 2015a).

However, scaling up a microreactor is a challenge because of the difficulties in the development of microreactor technologies that corresponds to plugging of small channels, replacement of deactivated catalyst and reactor costs (Saeidi *et al.*, 2015a).

2.4.3 Slurry & Fixed Bed Reactors

Commonly used commercial reactors for LTFT are Slurry reactors and Fixed Bed Reactors. Both the reactors have their advantages and disadvantages.

2.4.3.1 Slurry Reactors

Slurry reactors are well stirred CSTRs in which the reactants enter through the bottom and products in the form of light gases and wax is collected as shown in the schematic diagram in Figure 2-1. One of the biggest advantages of the slurry reactor include near isothermal operation. Slurry reactor offers low pressure drop across the reactor and allows ease of operation in terms of replacing the used catalyst compared to the FBRs. It also has an economic advantage over the FBRs in terms of construction cost (Espinoza *et al.*, 1999; Saeidi *et al.*, 2015b).

However, slurry bed reactor has its own challenges which include difficulties in scale up from pilot plant operations to large-scale operations, less ideal residence time behaviour and problems faced during separation of wax from the suspended catalyst resulting in the requirement of an additional equipment for the separation process (Saeidi *et al.*, 2015a).

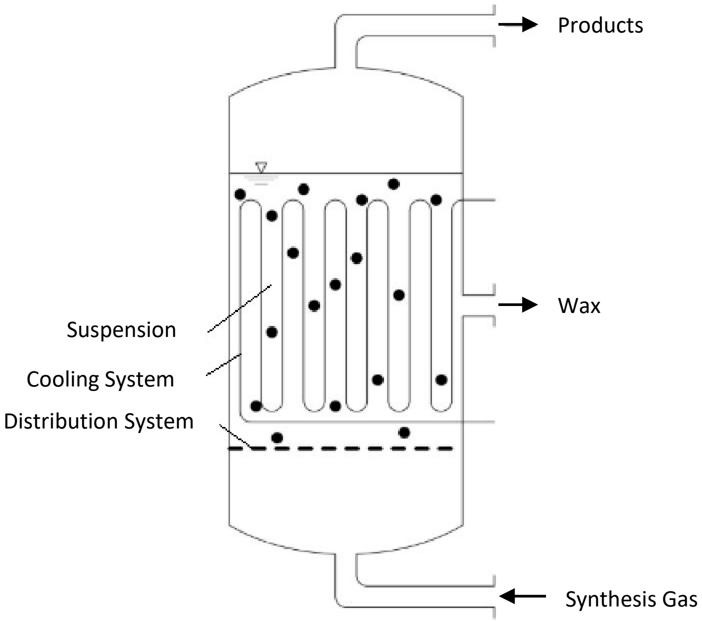

Figure 2-1: Slurry Bubble Column Reactor, reproduced from (Guettel, Kunz and Turek, 2008)

2.4.3.2 Fixed bed Reactors

Multitubular fixed bed reactors consists of parallel tubes carrying the catalyst particles firmly held, as shown in Figure 2-2. Their design can be considered like those of conventional shell and tube heat exchangers, wherein the reactions occur on the tube side and shell side has flowing water to enhance temperature control. They may have a random arrangement or a structured one.

The tubes behave similarly making the reactor easy to design, handle and scale-up as understanding the hydrodynamic behaviour of a single tube reactor in pilot-plant can give a lot of insight into the large scale multi-tubular reactors (Guettel, Kunz and Turek, 2008). It makes the use of FBRs feasible under a wide range of temperature conditions since the liquid or gaseous, or both products, can be easily accommodated. It also has a higher catalyst holdup relative to other types of reactors (Méndez, Ancheyta and Trejo, 2017).

Following are examples of some commercial scale plants employing FTS to convert natural gas or coal to liquid fuels. In 1973, Shell began the development of the Shell Middle Distillate Synthesis (SMDS) using FBR employing cobalt catalysts. In 1993, a plant for FTS was placed into operation based on natural gas with a capacity of 12500 bbl/day in Bintulu, Malaysia. Sasol and Qatar Petroleum started a FTS plant with a capacity of 70,000 bbl/day utilising natural gas obtained as by-product from oil production for the generation of syngas (Sie and Krishna, 1998).

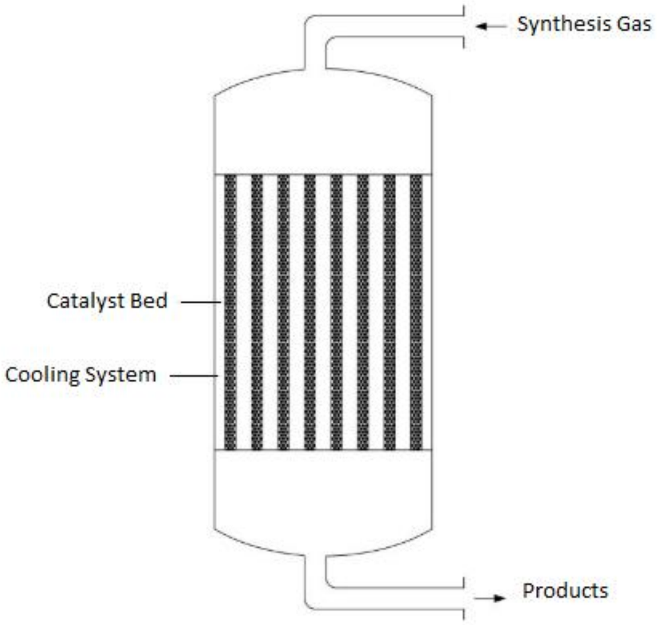

Figure 2-2 : Schematic diagram for a Multitubular Fixed bed reactor, reproduced from (Guettel, Kunz and Turek, 2008)

However, FBRs suffer from some serious drawbacks. They face high pressure drops and poor temperature control due to less heat transfer. FBRs also have drawbacks such as tube diameter restrictions, intraparticle diffusion limitations (Sie and Krishna, 1999).

The operation for FBRs is also labour intensive as it requires frequent replacement of catalyst due to their degradation after activity loss with time on stream. Narrower tubes can make the problem even more challenging.

Despite the drawbacks, multitubular fixed-bed reactors are the most well-known reactors that make it possible to achieve high CO conversion and liquid products selectivity (Sie and Krishna, 1998). Table 2-1 summarises the advantages and disadvantages of a fixed bed reactor and a slurry column reactor.

To overcome these abovementioned challenges with FBR operation, various researchers have proposed different process intensification solutions, especially based on optimising tube radius and catalyst particle size and shape. These have been summarised in the following sections.

Table 2-1: Advantages (+) and disadvantages (-) of FBRs and Slurry bubble column reactors for FTS, reproduced from (Guettel, Kunz and Turek, 2008)

S. no.		FBR	Bubble Column Reactor
1.	Pore Diffusion	-	+
2.	Catalyst content in Reactor	+	-
3.	Gas-Liquid Mass Transfer	+	-
1.	Isothermal Behaviour	-	+
2.	Catalyst Exchange	-	+
3.	Catalyst Attrition	+	-
4.	Need for liquid-solid separation	+	-
5.	Scale-up	+	-
6.	Reactor Costs	-	+

2.4.4 Influence of Reactor Parameters

2.4.4.1 Tube diameter

Since FT reactions are highly exothermic in nature, heat removal becomes extremely important as the efficiency of heat removal affects the reaction rates as well as the catalyst deactivation. Efficiency of heat removal depends on the heat transfer characteristics of the reactor system, which are highly dependent on the tube diameter. Therefore, the effect of tube diameter on the heat transfer characteristics should be understood in detail to be able to control the reactor temperature.

Chabot *et al.*, (2015) highlighted the effectivity of tubular millichannel catalytic reactors with respect to efficient heat removal yielding an almost isothermal operation. The low methane selectivity and production of long hydrocarbon chain was attributed to the near isothermal operation of the reactor. The millichannel reactors were used to study the effect of different tube diameters on the reactor performance. Hotspot temperature in the tube was seen to be rising with the diameter of the tube and can be attributed to the less efficient heat removal in the large diameter tubes. It was found that for tube diameters greater than 3.11 mm, temperature runaway was observed and hence no convergence was found due to strong coupling between other variables. For maintaining a hotspot which has a temperature difference less than 10 K, the optimum diameter was found to be 2.50 mm for a catalyst particle size of 90μm. Below this diameter, no significant temperature rise was seen, and isothermal operation was observed, which resulted in preventing the increase of light hydrocarbons selectivity.

To study the effect of tube diameter, particle size and pore diffusion, Jess and Kern, (2012) carried out detailed simulations on a single tube of a multitubular Fischer Tropsch Reactor with cobalt catalyst with the help of 1-D and 2-D models. For their operating conditions, it was found that for a given target CO conversion, tube diameter greater than an optimum value would result in temperature runaway, reinforcing the concept of an optimum tube diameter similar to Chabot *et al.*, 2015. This target CO conversion was 27% in their case and optimum tube diameter was found to be 39 mm. In simulations with a tube diameter greater than this value, the target CO conversion was progressively missed and to avoid a temperature runaway, a lower cooling temperature was needed. A lower cooling temperature in turn leads to a low reaction temperature and hence, lower reaction rate. Increasing particle diameter also increases the influence of the pore diffusion on the effective reaction rate of the syngas. This lowers the temperature sensitivity of the reactor and decreases the danger of temperature runaway.

2.4.4.2 Particle Size and Shape

Catalyst Pellet Size

The thermal behaviour of a multitubular FBR can be influenced by the pellet size of catalysts (Borkink and Westerterp, 1992). Simulation of a single-tube of a wall-cooled multitubular Fischer-Tropsch reactor indicates that the reactor performance can be improved by enlarging the catalyst particle diameter (Jess and Kern, 2012).

Increasing pellet diameter affects a number of parameters which in turn increase the overall heat transfer coefficient. One of these factors is the gas mixing within the bed. Reynolds number in a packed bed is given by:

$$Re = \frac{\rho_f v d_p}{\mu(1-\varepsilon)} \tag{2-1}$$

where d_p and ρ_f are equivalent particle diameter and density of fluid respectively. Increased particle diameter will result in an increased Reynolds number which in turn gives rise to turbulence which enhances mixing. Gas mixing is greatly enhanced by the large pellets, especially at the wall. This facilitates heat transfer. The other factor is the pressure drop. Large pellets exhibit smaller pressure drop and, hence, to achieve target CO conversions smaller bed lengths can be employed. Another factor is the pore diffusivity. The effect of pellet size on pore diffusivity is important as it is more pronounced than its effect on the pressure drop or the heat transfer. With increasing particle size, the effect of pore diffusion increases and hence the effective activation energy drops, which in turn helps avoid a thermal runaway (Jess and Kern, 2012).

However, increasing the pellet diameter, comes with some drawbacks, which affects the reaction rates adversely. Larger diameter pellets have long effective diffusion lengths L_{pe}, which is defined as:

$$L_{pe} = \frac{Pellet\ Volume}{Surface\ Area} \tag{2-2}$$

As L_{pe} increases (increasing d_{pe}, where d_{pe} is the effective pellet diameter), diffusion resistance increases and hence the effectiveness factor decreases, which makes the observed reaction rate decrease, which in turn results in requirement of a larger catalyst weight and hence, longer bed length as effectiveness factor denotes the ratio of observed reaction rate to hypothetical reaction rate in the absence of mass transfer limitations.

As the pellet size is reduced, the bed is tightly packed, this increases pressure drop. But increased bed density has opposite effect on the reaction rates. So, there is a trade-off between the effect of bed density and pressure drop on the required bed length for the reactor. So an optimal pellet size needs to be found out in order to get maximum reaction rates.

Catalyst Pellet Shape

The catalyst pellet shape has a direct effect on the hydrodynamics as well as the heat transfer of the FBR which is crucial because of the extreme exothermicity of the reaction.

The objective, in order to determine the most effective shape for the pellet, is to reduce the pressure drop and amount of catalyst required and increase the effectiveness factor.

The effects of different catalyst shapes on reactor performance were studied for the pressure drop, amount of catalyst required, effect on effectiveness factor and bed void fraction by Borkink and Westerterp, 1992, Lacroix *et al.*, 2009, Jess and Kern, 2012 and Brunner *et al.*, 2015.

The pellet shape which resulted in the least amount of catalyst required was found to be trilobes. In order of increasing catalyst weight, to achieve same CO conversion, the other shapes were given as hollow cylinders < cylinders < spheres. The rate of change of bed length with respect to effective pellet diameter is also the lowest for the trilobes (Brunner *et al.*, 2015). The effect of catalyst pellet shape on other parameters is summarised in Table 2-2.

Table 2-2 Effect of particle shapes on different characteristics for a reactor, reproduced from Borkink and Westerterp, 1992, Lacroix et al., 2009, Jess and Kern, 2012 and Brunner et al., 2015

S.No.	Characteristics	Order among different Shapes
1.	Pressure drop	spheres > cylinders > trilobes > hollow cylinders
2.	Least amount of Catalyst required for same CO conversion	trilobes > spheres > cylinders > hollow cylinders
3.	Effectiveness factor	trilobes > hollow cylinders > cylinders > spheres
4.	The bed void fraction	hollow cylinders > trilobes > cylinders > spheres

There is a trade-off between diffusion lengths and pressure drop for the optimum catalyst shape. Trilobes, among other available catalyst shapes, optimize this trade-off best as they require the minimum required catalyst mass to achieve a particular CO conversion value. This can be attributed to the maximisation of the catalyst effective ness by reduction of the diffusion resistance in the pores (Brunner *et al.*, 2015).

2.5 Mathematical Modelling

The kinetics and transport restrictions in Fischer–Tropsch synthesis are complex, and they complicate direct scale-up of the reactor. Mathematical modeling is a method through which development time and material losses can be reduced.

2.5.1 Kinetics

There are two approaches that are primarily employed to describe the kinetics of FTS reactions:

1. The basic assumption made in the first method is that the reaction products have no role in the monomer formation mechanism. Therefore, expressions are postulated to describe the reactant consumption rates based on their disappearance either empirically or through derivation of Langmuir-Hinshelwood-Hougen-Watson (LHHW) or Eley-Rideal type of rate equations. Different product distribution models can then be developed and employed to describe the product selectivity. The most popular product distribution model is the Anderson-Schulz-Flory (ASF) model. The products in the ASF model are lumped together based on number of carbon number in the hydrocarbons (Yang *et al.*, 2003; Visconti *et al.*, 2007 & Mthombeni, 2009).

2. An alternative approach for the kinetics involves proposing a reaction mechanism and developing kinetic expressions for the steps where reactants are consumed leading to the formation of final products. It appears to be more realistic than the previous approach (Mthombeni, 2009).

2.5.1.1 Approach 1: Modelling the CO conversion and Product Selectivity Models

This approach is based on the assumption that the products do not have a contribution in the formation of the monomer. The rate of CO consumption is generally correlated with the concentration of CO, H_2 and H_2O in the gas phase Most expressions are derived using the LHHW approach (Mthombeni, 2009).

Van Steen and Schulz, (1999) in their model assumed that the monomer formation step in the mechanism is the rate limiting step and all the other reaction step were in equilibrium. The following expression was proposed for the CO conversion based on a kinetically controlled production distribution approach:

$$r_{CO} = \frac{aP_{CO}(P_{H_2})^{3/2}/P_{H_2O}}{\left[1 + bP_{CO}P_{H_2}/P_{H_2O}\right]^2} \tag{2-3}$$

Ledakowlcz *et al.*, (1985) proposed the following expression taking into account the consideration of Water Gas Shift (WGS) reaction which leads to the formation of carbon dioxide and has a significant effect on the syngas consumption rate due to the chemisorption of water (Mthombeni, 2009):

$$-r_{CO+H_2} = 1.4 * 10^{10} * e^{-\frac{12407}{T}} * \frac{C_{H_2}}{1 + 0.115\frac{C_{CO_2}}{C_{CO}}} \tag{2-4}$$

The following expression, for the overall Fischer Tropsch reaction, was proposed by Van der Laan, Beenackers and Krishna, (1999) :

$$\mathrm{r_{FT}} = \frac{\mathrm{kP_{CO}P_{H_2}}^{1/2}}{\left(1 + \mathrm{aP_{CO}} + \mathrm{bP_{CO_2}}\right)^2} \tag{2-5}$$

Ahón *et al.*, (2005) proposed the following expression in terms of fugacities to account for the systems with high pressures:

$$\mathrm{r_{FT}} = \frac{\mathrm{k_{FT} f_{CO}}^{-1/2} \mathrm{f_{H_2}}^{-1/2}}{1 + \mathrm{cf_{CO}}^{-1/2} \mathrm{df_{H_2}}^{-1/2}} \qquad (2\text{-}6)$$

Ermolaev *et al.*, 2015 used the explicit rate equations based on the LHHW adsorption theory:

$$\mathrm{R_{CO}} = \frac{\mathrm{k_{CO}}.\mathrm{P_{CO}}^{2/3} \mathrm{P_{H_2}}^{2/3}}{\left(1 + \mathrm{K_{CO}}.\mathrm{P_{CO}}^{2/3}.\mathrm{P_{H_2}}^{1/3}\right)^{2}} \qquad (2\text{-}7)$$

The chain growth probabilities of Fischer-Tropsch products used were:

$$\mathrm{C_\alpha} = \frac{1}{1 + \frac{\mathrm{k_\alpha}}{\mathrm{P_{CO}}^{2/3} \mathrm{P_{H_2}}^{2/3}}.(1 + \mathrm{C_\beta})}, \qquad \mathrm{C_\beta} = \frac{1}{1 + k_\beta {P_{H_2}}^{0.5}} \qquad (2\text{-}8)$$

Where $\mathrm{k_\alpha}$ and k_β were given as functions of temperature:

$$\mathrm{k_\alpha} = 40.3 \exp\left(-9600 \, * \left(\frac{1}{\mathrm{T}} - \frac{1}{488.15}\right)\right) \qquad (2\text{-}9)$$

$$\mathrm{k_\beta} = 0.035 \exp\left(-4800 \, * \left(\frac{1}{\mathrm{T}} - \frac{1}{488.15}\right)\right) \qquad (2\text{-}10)$$

A product distribution model like Anderson-Schulz-Flory (ASF) is usually utilised to determine the distribution of the polymerisation products. It leads to a linear system of rate equations (Rofer-depoorter, 1981 & Visconti *et al.*, 2007).

2.5.1.1.1 ASF Distribution

The ASF product distribution model describes the whole product range using one parameter known as α. The α defines the probability of adding of a monomer to the polymer chain (Laan and Beenackers, 1999) and is given by:

$$x_i = \alpha_i \, * x_{i-1} \qquad (2\text{-}11)$$

Where x_i and x_{i-1} are the mole fractions of hydrocarbons having *i* and *i* – 1 number of carbon atoms respectively. It is assumed that during polymerisation, C_1 monomer units are added stepwise to a growing hydrocarbon chain on the catalyst surface (Mthombeni, 2009).

The α_i can be defined as:

$$\alpha_i = \frac{R_{p,i}}{R_{p,i} + R_{t,i}} \tag{2-12}$$

where $R_{p,i}$ and $R_{t,i}$ are the propagation and termination rates of the specie i respectively (Laan and Beenackers, 2011). The value of α_i may or may not be a function of the carbon number. If it is independent of carbon number, then it can be written as:

$$x_i = (1 - \alpha)\alpha^{i-1} \tag{2-13}$$

A plot of log of hydrocarbons' mole fractions and the carbon number should yield a straight line with the slope equal to α (Raje and Davis, 1996). Figure 2-3 shows the product distribution for ASF approach for an α value of 0.85. Some researchers have proposed models where α values have been presented as a function of carbon numbers (Schulz and Claeys, 1999; Lee and Chung, 2012).

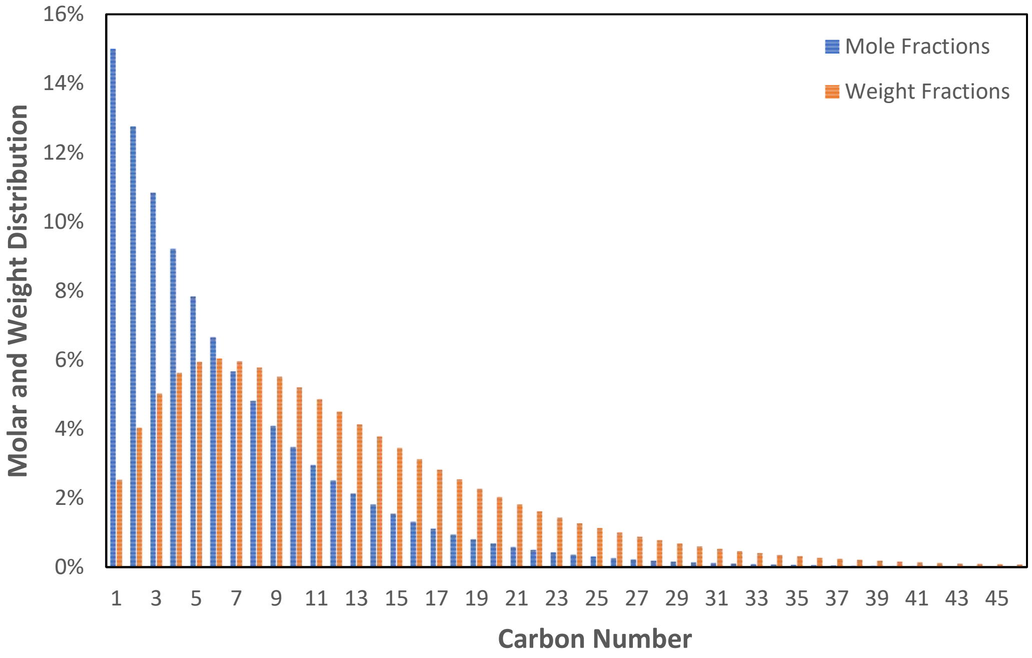

Figure 2-3: ASF product distribution for a constant α value of 0.85 (Vessia O., 2002)

ASF provides a simple way to predict the product distribution for FTS. However, it presents an idealistic view. The product selectivities obtained during experiments are observed to deviate from the ASF pattern. The major deviations observed from ASF behaviour include:

1. More than one α value in the product selectivity
2. Positive and negative deviations from the ideal ASF behaviour
3. Anomaly of C_1 and C_2 hydrocarbons

One of the possible reasons behind the deviation from the ideal behaviour is readsorption of olefins. Several researchers have proposed models where they have included the olefin readsorptions into their kinetic models by including it with the chain growth and termination on the same catalytic site (Van der Laan, Beenackers and Krishna, 1999; Ahón *et al.*, 2005 & Anfray *et al.*, 2007).

Lumped model approach is a convenient way of describing the kinetics for the Fischer Tropsch. There are, however, certain drawbacks with this approach. In this approach, all the reactions are parallel and independent, all the products originate directly from the reactants and do not follow any chain reaction steps and therefore, it cannot be used to study the effect of vapor-liquid equilibrium or the mass transfer on the product distribution. The mass transfer will, however, show its effect on the rate of reactant consumption, without having any impact on the product distribution.

The other drawback associated with the lumped model approach is that it is not suitable to predict the thermal behaviour of the FT system because it cannot be used to determine the exact amount of heat released by the exothermic reactions or the stoichiometric molar consumption ratio of hydrogen to carbon monoxide. For example, the kinetic model determines the amount of CO disappeared, but the amount of heat released will vary depending on the type of product generated. For example, 10 moles of CO consumed to produce 1 mol of n-decane or 10 moles of methane can produce 1560 kJ or 2060 kJ of heat, respectively (Lee and Chung, 2012).

Based on the above-mentioned reasons, it can be concluded that the product distribution models are unable to provide an accurate description of the product selectivities and hence an approach which proposes the rate laws by taking into the consideration, reaction mechanism and postulation of the rate determining step would be a better way to assess the product distribution and other aspects.

2.5.1.1.2 Approach 2

For most works in literature, Langmuir-Hinshelwood (LH) approach has been employed for modeling the kinetics. The LH approach uses the alkyl mechanism to develop the rate expressions for the n-paraffins and olefin formation (Laan, 1999). This approach proposes a rate determining step (RDS) and then complex rate expressions are developed which usually require many adjustable parameters.

This research project employs a different approach, whereby the thermodynamic and kinetic models are coupled and dependent on each other. This is done by following kinetic approach 2 from section 2.5.1, whereby elementary reaction rate equations are developed for every mechanistic step. The reaction rate equations are written in terms of species' activities, a concentration like measure of species' deviations from the standard state.

Activity is defined as the ratio of the fugacity of a species in a mixture to the fugacity of that species at the standard pressure. Section 3.1 explains the kinetic formulation for the current project (Davies and Möller, 2021b).

2.5.2 Heat Transfer

Since FTS is highly exothermic, the selectivity to middle distillates is predominantly guided by the temperature control and isothermal operation (Almeida *et al.*, 2011).

Fischer Tropsch reactions have a high heat of reaction (165 kJ/mol$_{CO}$). It can cause an adiabatic temperature rise of 1750 K (estimated by $\Delta H_r / C_{p,reactants}$). This problem is more serious for reactors with low tube-to particle diameter ratio. Therefore, temperature management is one of the key challenges for the intensification of the Fischer Tropsch process for the FBRs. This sharp temperature rise can lead to serious consequences, like an explosion of the reactor (Copelli *et al.*, 2016). Therefore, to prevent this, it is crucial to study the thermal behaviour of such tubes with the help of computer simulations before experimentation (Borkink and Westerterp, 1992). Following are the heat transfer mechanisms recognised by Yagi and Kunii, (1957) that are independent of fluid flow:

1) Thermal conduction through:
    1.1. The stagnant fluid
    1.2. The solids
    1.3. The contact surfaces of two catalyst particles
2) Radiant Heat transfer between:
    1.1. Surfaces of particles
    1.2. Neighbouring voids

The heat transport mechanisms that are dependent on fluid flow are:

1) Thermal conduction through the fluid film near the contact surface of two particles
2) Heat transfer by convection solid-fluid-solid
3) Heat transfer by lateral mixing of fluid due to the dividing and filaments passing round particles of packing

The FBRs experience poor heat conduction due to the limited contact points between the catalyst pellets and between the particles and the reactor walls. This leads to a non-isothermal operation of the reactor with presence of hot-spots and strong axial and radial temperature gradients inside the reactor. This, in turn, adversely affects the desired product selectivity, results in faster catalyst deactivation, and also leads to a possibility of thermal runaway of the reactor. Tubes in the commercial FBRs are generally limited in diameter to prevent the undesirable hot-spots (Zhu *et al.*, 2010).

Catalytic deactivation due to excess temperature leads to an autothermal temperature rise. The catalyst is deactivated in the region of the main reaction zone due to excess temperature. This leads to a migrating combustion zone in which the maximum temperature rises further and so on (Copelli *et al.*, 2016). This has been clearly depicted in the references Blaum, 1974 and Emig *et al.*, 1980.

The measures usually taken for the abovementioned challenges in the industries are limiting the CO conversion per pass, recycling the unconverted syngas along with a considerable fraction of the liquid phase. However, these measures have their own limitations. Modifications in the operating conditions to improve one parameter usually comes at the cost of other parameter. Innovations in reactor configurations is better than changing the operating conditions as it can be far more effective for temperature control at the same operating conditions, thus not compromising with reactor performance. A few such innovations are found in literature and are explained in the following section.

2.5.2.1 Innovations in Reactor Configurations

An efficient reactor design is necessary for making maximum use of catalyst. A reactor can never increase the activity or selectivity of a catalyst; however, a poorly designed reactor can decrease one or both the properties for a catalyst. Hence, there is a need to match the catalyst and reactor to achieve optimum productivity (Sparks *et al.*, 2017).

Given different concerns with conventional reactors, especially heat transfer inefficiencies, to intensify the FT process, different strategies have been proposed (Saeidi *et al.*, 2015a). Plate type reactor is one of the possible developments to achieve this aim.

In early FT studies, a few approaches have been reported, where efforts have been made to control the magnitude of the FT exotherm using innovative reactor designs. One such approach was to use the concentric tubes with cooling water passing through the inner tube and in the space outside the outer tube. The catalyst thickness, sandwiched between the cooling water sections, was about 10 mm (Sparks *et al.*, 2017). The configuration of this reactor arrangement is similar to the plate type reactors.

In another such study, Fratalocchi *et al.*, (2018) showed that open-cell foams made of thermally conductive material as reactor internals can be a viable alternative to the conventional FBRs by enabling us to control the mean temperature inside the reactor. Packing the foam also increases the amount of catalyst loading compared to the loading obtained by washcoating the same foam. However, such reactor systems are difficult to scale up and hence are not reliable for commercial use.

Gas phase microreactors is also an example of one such innovative reactor design and is being utilized for decades. The following section briefly denotes the geometric design and the advantages of a microreactor.

(b)

2.5.2.1.1 Micro-channel Reactors

A microreactor (μFBR) consists of several micro-channel reactors of sides of order 1 mm usually arranged in a crossflow configuration for the transport of syngas and cooling water. The reactor geometry comprises 3 main parts:

1. The reactor channel holding tube bundles which have a uniform layer of coating of active catalyst on the inner walls. The syngas is passed through these channels. The channels are generally of the order of a few millimetres.
2. The coolant channels which contain flowing fluid for absorbing the reaction heat from reactor channels, are generally of the order of a few millimetres.
3. The solid domain of the microreactor, generally made of metal, constituting the outer geometry of microreactor. The reactor and coolant channels are embedded in this solid region. A schematic diagram showing microreactor geometry is shown in Figure 2-4.

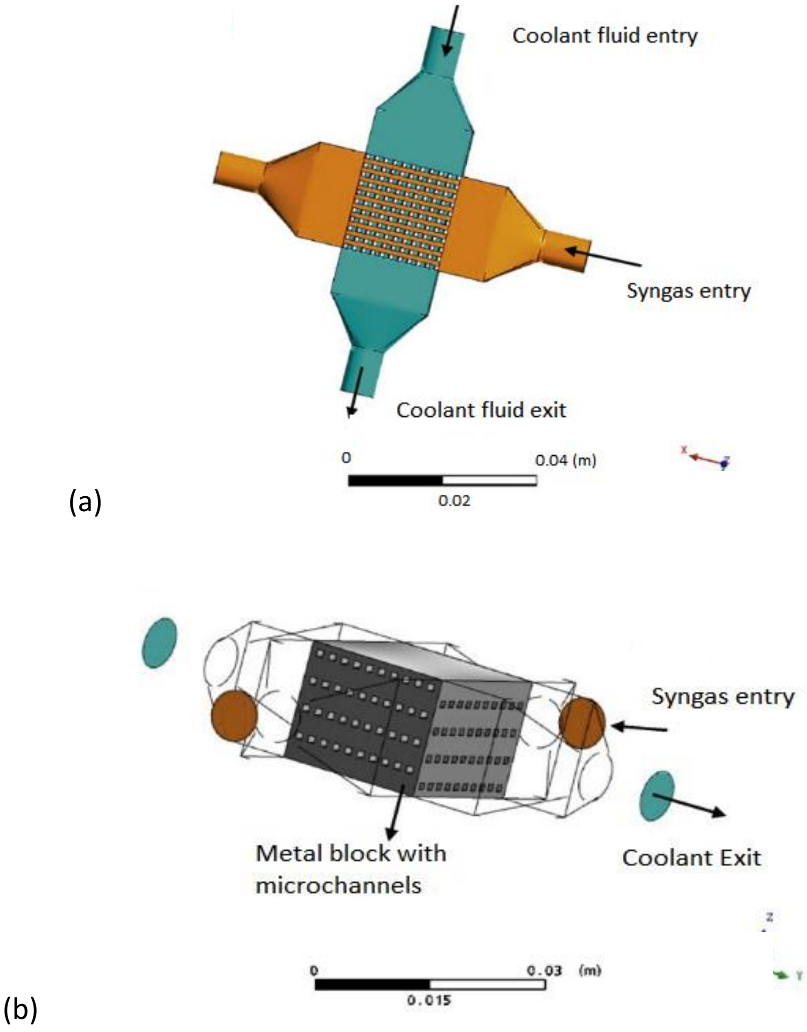

Figure 2-4(a) : Two fluidic domains of a micro-channel reactor, syngas FTS products – Orange and cooling fluid – Blue (b): The solid domain of a micro-channel reactor, adapted from (Arzamendi et al., 2010)

Micro-channel reactor technology provides us with heat transfer enhancement which is due to increased heat transfer surface area per unit volume decreasing the channel hydraulic diameter, which means it allows for higher reactant concentrations and catalyst loadings. Micro-channel reactors allow us to achieve virtual isothermal operation of FT which favours selectivity for middle distillates in the product distribution. Focus of models developed for micro-channel reactors has mostly been the study of heat transfer characteristics (Arzamendi *et al.*, 2010).

Progress in the work using micro-channel reactors has advanced to the point that commercialisation is being considered possible (Kibby *et al.*, 2013; H.J.Robota *et al.*, 2014 & Sparks *et al.*, 2017). Micro-channel reactors have proven to be more effective in heat removal relative to conventional reactors and have been explored in detail in literature (Saeidi *et al.*, 2015a).

Observing the excellent heat transfer properties of micro-channel tubes, it is worth exploring the effect of size, shape and configuration of the innovative FTS reactors compared to the tubular reactors on reactor performance.

The structure of a FBR reactor for FTS is very similar to a Shell & Tube heat exchanger. The following section compares the potential of shell and tube and plate and frame heat exchangers with respect to heat transfer power and other relevant properties.

2.5.2.2 Shell and Tube vs. Plate Type Heat Exchangers

With regards to heat transfer capabilities, Plate and frame heat exchangers have found to be more effective than the conventional shell and tube heat exchangers (Tumuluri, 2018). *Figure 2-5* shows an exploded view of a plate type heat exchanger. For two same fluids, the overall heat transfer coefficient is found to be higher in the plate type heat exchangers compared to the shell and tube heat exchangers (Bright Hub Engineering, 2010 & HFMPHE, 2018). The turbulent flow in the plates also helps to reduce deposits which interferes with heat transfer (Marine Engineering Study Materials, 2014). Additional advantages relevant to FT include lesser pressure drop, scalability, reduced maintenance, lesser capital expense, compact design.

Shell and tube heat exchangers used to dominate the market up until the latter part of the 20th century, as plate heat exchangers began replacing them in most industrial and most HVAC applications (Paul Mueller Company Engineering Staff, 2016).

Noting good heat transfer capabilities of plate type heat exchanger over shell and tube heat exchanger, a plate type reactor over conventional tubular reactors is worth exploring. There are numerous research studies available on a plate type heat exchanger, but as a reactor, it is yet to be researched on. Therefore, studies comparing tubular reactors and plate type reactors for FTS are scarce. Following section presents studies for plate type FTS reactors.

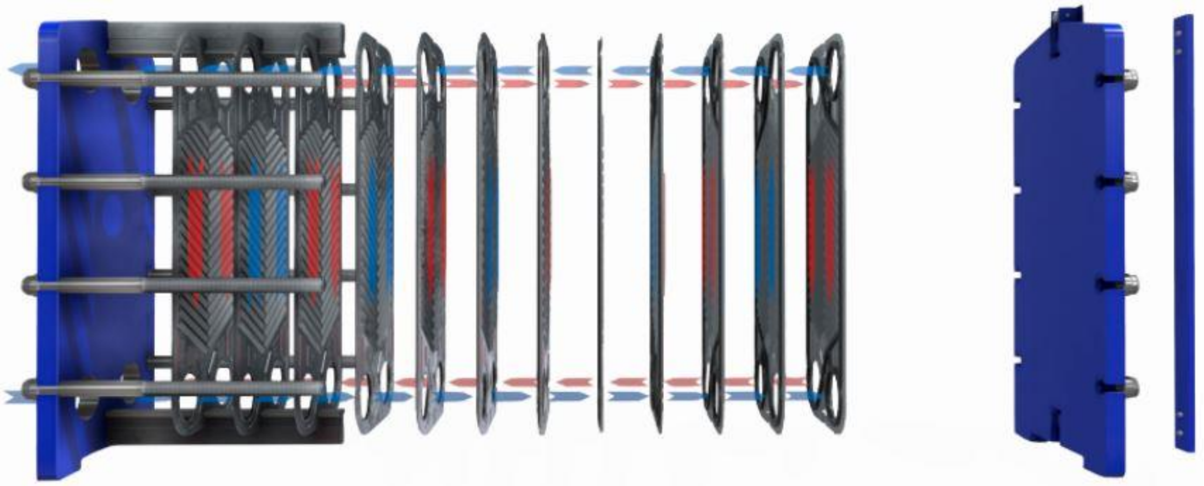

Figure 2-5 Exploded view of a Plate Type Heat Exchanger, reproduced from Savree (2020)

2.5.2.2.1 Plate Type Reactors for FT

Park *et al.*, 2014 carried out a FT simulation study in a channel type reactor with a plate heat exchanger (PHE). High heat transfer coefficient (HTC) between the reaction system and atmosphere was achieved. In addition, increased coolant flow rate was used to remove the heat generated by highly exothermic FTS reaction.

Sparks *et al.*, 2017 evaluated an aluminium small channel reactor, with a catalyst bed of the dimensions 2 X 4 mm. The data obtained using the channel reactor was found to be similar to an isothermal CSTR case, which means that the temperature within the reactor was maintained well and hence, almost isothermal behaviour was observed. It was also found that aluminium is a better choice for reactor material compared to the stainless steel, due to its superior heat conductivity and lower manufacturing cost, despite the usability of steel to be operated at higher temperature-pressure regions.

Taking an idea from abovementioned innovations and the efficiency of a plate type heat exchanger, a plate type reactor for FTS is studied in this project. Followed by which, a comparison is carried out between the conventional tubular reactor and the plate type reactor to observe the effect of reactor shape on heat transfer.

The performance of a plate type reactor strongly relies on the channel design and interplay between adjacent channels for exothermic as well endothermic reactions. The flow of hot and cold fluids happen in alternative spacings between the plates as shown in *Figure 2-6*. The red and blue arrows denote the flow directions of hot and cold fluids respectively.

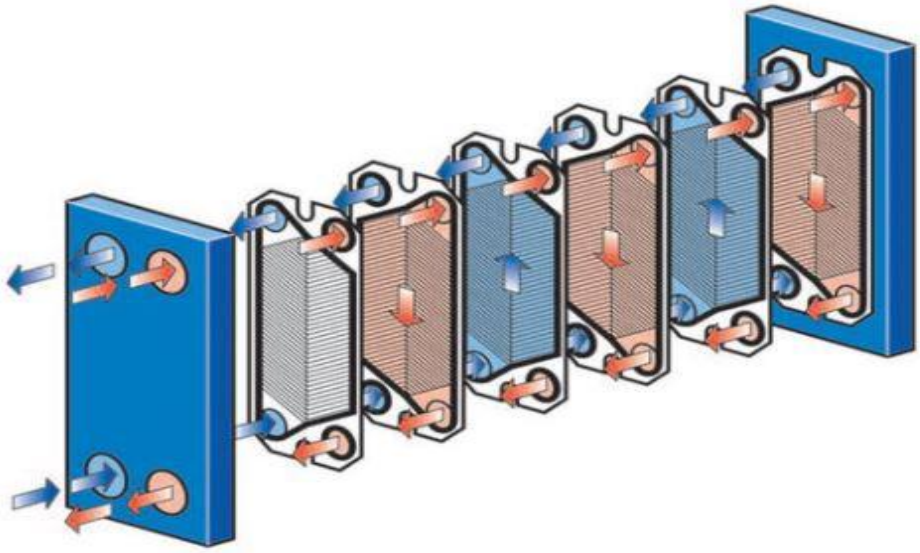

Figure 2-6 Heating cooling media flows in alternating channels between plates (Designs, 2021)

Hence, it is of immense importance to understand the dependence of a plate type reactor on the structure design parameters (Shin *et al.*, 2014).

Extensive research in the domain of plate type macro-reactors is not yet done. However, efficient heat transfer qualities of a plate type heat exchanger seem promising. The studies done on structural dependence of a plate type heat exchanger to find an optimum plate to plate spacing can be used as a reference to explore the optimum plate spacing for a plate type reactor for FT. Following section presents an analysis for the same using the studies reported in literature.

2.5.2.3 Plate Spacing

There have been several researchers who have studied the optimum plate spacing in a plate type heat exchanger for natural convection (Bodoia and Osterle, 1962; Levy, 1971; Bar-Cohen and Rohsenow, 1984; Kim, Anand and Fletcher, 1991). Studies to access the effect of plate spacing for forced convection are few.

Plate spacing has a direct influence on the channel velocity, equivalent diameter, pressure drop and Reynolds number in a PHE design (Rohmah *et al.*, 2015). Ambarita *et al.*, 2009 studied the optimum plate to plate spacing for maximum heat transfer rate from a flat plate type heat exchanger for parallel and counter flow directions of the working fluids using analytical and numerical solutions. The results showed that the optimum plate to plate spacing for a counter flow heat exchanger is smaller than parallel flow ones and the maximum heat transfer rate for a counter flow heat exchanger is bigger than parallel flow ones.

A 2-D CFD numerical simulation was carried out to study the effect of plate spacing on heat transfer characteristics within a parallel-plate heat exchanger by Huang and Jaworski, 2019. The study was carried out in a standing wave thermoacoustic system. It was found that the heat flux and the heat transfer coefficient increase with decreasing plate spacing. Less volume of the heat generating space available might be one of the possible reasons. It was also found that transition to turbulence regime due to increasing plate spacing has a strong effect on the heat transfer characteristics of the plate type heat exchanger.

All the above-mentioned works in literature are for non-reactive flows. Studies for optimum plate spacing for reactive flows could not be found in literature. In the current project, structural dependence of the plate type reactor on the plate spacing has been studied for a forced convection reactive flow. A parametric study on the plate spacing was carried out to understand its effect on reactor performance.

2.5.3 CFD Modeling

The primary mode of heat dissipation in the tubular FBRs is the radial heat transfer. To be able to control the temperature in the catalyst bed, it's important to match the radial heat transfer to the heat of reactions (Zhu *et al.*, 2010). Therefore, it is important to model the system as a 2D reactor in order to take account of the radial variations of temperature in the reactor. A few 2-D mathematical modeling studies on fixed bed FT reactors have been reported in literature based on various assumptions. A comparison between 1-D and 2-D models suggests that 2-D model leads to more accurate prediction in cases of thermal runaways as the runaway behaviour predicted by the 1-D model leads to a critical, too high cooling temperature (Jess and Kern, 2009).

A CFD simulation is a numerical method for calculation of nonlinear differential equations describing fluid flow, heat transfer, mass transfer, chemical reactions, and related phenomena for 2-D and 3-D computational domains. This is done by breaking the continuous fluid domain into a set of small discrete domains and solving conservation equations for those discrete domains to obtain a solution for the overall domain.

Very few studies have been carried out for analysing the reactor behaviour for Fischer Tropsch tubular FBRs using CFD. Most of these studies are based on a 2D pseudo-homogeneous model of FTS, where a lumped model has been employed for the kinetics and an ideal behaviour is assumed for the gases (Arzamendi *et al.*, 2010; Miroliaei *et al.*, 2012;

Aligolzadeh *et al.*, 2015 & Moganiwa and Oladiran, 2016). A few CFD studies published lately, however, have taken the real gas behaviour into account (Irani, 2014).

In the current project, a 2-D CFD model of a reactor of industrial scale has been developed, to take into account the radial variation of temperature and species concentrations. The 2-D model is then compared with a 1-D model to assess the effect of radial variations on CO conversion and product selectivity. Unlike the 1-D kinetic models, which neglect the radial variations in the reactor, the product distribution obtained by this CFD model was expected to be more realistic.

Part 2: Model Development

3 Chapter - Model Development

3.1 The Kinetics

A FT kinetics model should meet the following requirements:

1. It must preserve the polymerisation nature of the FT reactions so that the product distribution is accurately represented.
2. It must be thermodynamically consistent once the chemical equilibrium is established.
3. It must consider the partial chemical equilibrium aspect that exist in the n-Paraffin and the 1-Olefin homologous series that give rise to the thermodynamic basis of the ASF distribution (Norval and Phillips, 1990; Norval, 2008).

As given in section 2.5.1.1, most kinetics models in literature use the alkyl mechanism and develop rate expressions for hydrocarbon formation by deriving the Langmuir-Hinshelwood (LH) theory, which includes proposing a rate determining step (RDS) (Van der Laan, Beenackers and Krishna, 1999; Visconti *et al.*, 2007 & Davies and Möller, 2021). The allocation of the RDS and the form of these rate expressions means that the polymerisation nature of FT reactions is not retained and the contribution of every step of the process is not considered properly (Allie and Nyathi, 2019). Also, the kinetic parameters in these models are highly correlated, which complicates the process of parameter estimation (Schwan, 2001; Sharrock and Coetzert, 2007 & Ostadi, Rytter and Hillestad, 2016). In addition, the extrapolation of these kinetic models for high carbon number hydrocarbon products is questionable as they are valid only upto a few carbon numbers i.e. upto C_{15} or C_{20}. Which implies that these models do not account for a sizeable fraction of the product distribution. Noting these factors, an inference can be drawn that the complex FT reaction behaviour cannot be described by Kinetics alone and a thermodynamics perspective is required along with it (Glasser *et al.*, 2012 & Davies and Möller, 2021). Hence, a kinetic model with a partial equilibrium approach to the Kinetic Modeling was employed in this project. It is directly taken from the work of Davies and Möller, 2021.

The Paraffins and the Olefins are considered as separate subsystems working to achieve partial equilibrium. This implies that the yield of the products is controlled by the reaction kinetics while their distribution is controlled by the thermodynamics (Norval and Phillips, 1990; Davies and Möller, 2021a; Norval and Phillips, 1990 & Davies and Möller, 2021)

FT reaction should be viewed as methylene polymerisation reaction. Methylene is a monomer unit ($-CH_2-$) formed by the hydrogenation of CO. To satisfy the abovementioned criterion, a reaction pathway is proposed (Fernandes, 2006) and is shown in *Figure 3-1*.

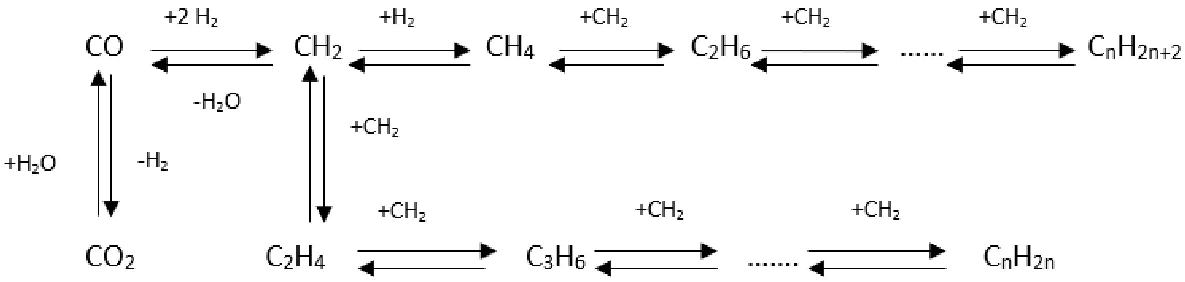

Figure 3-1 Proposed reaction pathway, adapted from (Fernandes, 2005 & Schulz, Steen and Claeys, 1994)

The chain initiation occurs in the first step in the and is shown in *Figure 3-1* where Carbon monoxide is hydrogenated to produce the monomer(CH_2) and water. The monomer (CH_2) is assumed to be a pseudo-specie which is at a pseudo-state and hence it has a zero net rate of formation. It means that the monomer is so reactive that it reacts almost immediately as it forms. It was introduced by Norval, 2008 to describe the FT using an equilibrium approach by highlighting a thermodynamic basis of the ASF distribution.

The addition of CH_2 facilitates carbon-carbon coupling which allows chain growth. N-Paraffins and 1-Olefins are shown to have separate chain growth reactions in a series-parallel reaction network (Mthombeni, 2009). CO may also react with the water being formed to produce CO_2 and H_2 in the Water Gas Shift Reaction. *Table 3-1* shows the reactions involved in the reaction pathway in and is shown in *Figure 3-1*:

Table 3-1 Chemical reactions in the proposed reaction pathway

S.no.	Reaction Step	Reaction	
1.	Monomer Formation	$CO + 2H_2 \rightleftharpoons CH_2 + H_2O$	(3-1)
2.	Methanation	$CH_2 + H_2 \rightleftharpoons CH_4$	(3-2)
3.	Initiation	$CH_2 + CH_4 \rightleftharpoons C_2H_6$	(3-3)
4.	n-Paraffin chain growth (n=2,3………N-1)	$CH_2 + C_nH_{2n+2} \rightleftharpoons C_{n+1}H_{2(n+1)+2}$	(3-4)
5.	1-Olefin chain growth (n=1,2,3……N-1)	$CH_2 + C_nH_{2n} \leftrightharpoons C_{n+1}H_{2(n+1)}$	(3-5)
6.	Water Gas Shift	$\mathrm{CO} + \mathrm{H_2O} \leftrightharpoons \mathrm{H_2} + \mathrm{CO_2}$	(3-6)

N represents the highest carbon number present in the system. It was taken as 20 for the current CFD project to reduce computational costs. However, the kinetic model has been verified and shown to give good results for a larger N(=80) in the reference Davies and Möller, 2021a. It is, therefore, safe to extrapolate the results for high carbon number compounds and therefore, it can be used to represent a sizeable fraction of the product distribution. *Table 3-2* shows the rate expressions proposed for each reaction step shown in *Table 3-1*.

Table 3-2 Rate expressions for the reaction steps in the proposed reaction pathway

S.no.	Reaction Step	Rate Expression	
1.	Monomer Formation	$r_1 = k_1\left(a_{CO}a_{H_2}^2 - \frac{a_{CH_2}a_{H_2O}}{K_{a,1}}\right)$	(3-7)
2.	Methanation	$r_2 = k_2\left(a_{CH_2}a_{H_2} - \frac{a_{CH_4}}{K_{a,2}}\right)$	(3-8)
3.	Initiation	$r_3 = k_3\left(a_{CH_2}a_{CH_4} - \frac{a_{C_2H_6}}{K_{a,3}}\right)$	(3-9)
4.	n-Paraffin chain growth (n=2,3,. . . . .N-1)	$r_{n+2} = k_4\left(a_{CH_2}a_{C_nH_{2n+2}} - \frac{a_{C_{n+1}}H_{2(n+1)+2}}{K_{a,n+2}}\right)$	(3-10)
5.	n-Olefin chain growth (n=2,3,. . . . .N-1)	$\mathrm{r_{N+n+1} = k_5\left(a_{CH_2}a_{C_nH_{2n}} - \frac{a_{C_{n+1}H_{2(n+1)}}}{K_{a,N+n+1}}\right)}$	(3-11)
6.	Water Gas Shift	$\mathrm{r_{2N+1} = k_6\left(a_{CO}a_{H_2O} - \frac{a_{H_2}a_{CO_2}}{K_{a,2N+1}}\right)}$	(3-12)

Every rate expression in Table *3-2* is expressed in terms of species activity which is given in equation (3-14). Activity is defined as the ratio of a species fugacity in a mixture relative to the fugacity of the specie in its pure form at a standard pressure as shown:

$$a_i = \frac{f_i}{f_i^{\circ}} \tag{3-13}$$

Since the calculation of the equilibrium constant uses the ideal gas as the reference state, the reference fugacity simplifies to the reference pressure which is commonly 1 bar(a) and the fugacity in a mixture can be written as a product of its partial pressure and its fugacity coefficient, activity is given as:

$$a_i = \frac{y_i \, \phi_i P_{total}}{P_{ref}} \tag{3-14}$$

here

y_i	Mole fraction of specie i in vapor phase
ϕ_i	Fugacity coefficient of specie i
P_{total}	Total pressure
P_{ref}	Reference pressure

The fugacity coefficient was found using the Peng-Robinson method in COCO. For ansys, in order to reduce complexity, ideal gas behaviour was assumed for the gases. The value of fugacity coefficient for all species in Ansys was assumed to be unity. Hence eqn (3-14) was changed to the following form:

$$a_i = \frac{y_i \, P_{total}}{P_{ref}} \tag{3-15}$$

for ansys. Hence, the kinetic driving force in each rate expression in eqn (3-7) – eqn (3-12) is the species partial pressure for Ansys. The values of fugacity coefficients in COCO were found to be close to 1. Hence, the ideal gas assumption could be safely applied in Ansys.

The thermodynamic aspect of the kinetic model and the calculation of the activity of the monomer CH_2 is shown in **Appendix A**.

To eliminate the a_{CH_2} term from the rate equations (3-8)-(3-11), first reaction of monomer formation was added to the reactions in (3-8)-(3-11) and the following reactions in *Table 3-3* were achieved and used for reaction set up in Ansys fluent with rate expressions from *Table 3-2*.

Table 3-3 Reaction steps after eliminating CH₂ from Table 3-1

S.no.	Reaction Step	Reaction	
1.	Methanation	$CO + 3H_2 \rightleftharpoons CH_4 + H_2O$	(3-16)
2.	Ethane Formation	$CO + 2H_2 + CH_4 \rightleftharpoons C_2H_6 + H_2O$	(3-17)
3.	Propane Formation	$CO + 2H_2 + C_2H_6 \rightleftharpoons C_3H_8 + H_2O$	(3-18)
4.	n-Paraffin chain growth (n=3,4,5………N-2)	$CO + 2H_2 + C_nH_{2n+2} \rightleftharpoons C_{n+1}H_{2(n+1)+2} + H_2O$	(3-19)
5.	1-Olefin Formation	$2\mathrm{CO} + 4\mathrm{H_2} \rightleftharpoons \mathrm{C_2H_4} + 2\mathrm{H_2O}$	(3-20)
6.	Olefin chain growth (n=2,3……N-2)	$CO + 2H_2 + C_nH_{2n} \rightleftharpoons C_{n+1}H_{2(n+1)} + H_2O$	(3-21)
7.	Water Gas Shift	$\mathrm{CO} + \mathrm{H_2O} \leftrightharpoons \mathrm{H_2} + \mathrm{CO_2}$	(3-22)

3.2 Reactor Assumptions

The assumptions taken for the kinetic model and the reactor model in this study are given as follows. Most of them were taken to reduce the complexity in the CFD model.

Kinetic Model Assumptions:

1. Water gas shift reaction was not considered in the kinetic model, due to it occurring in negligible amounts for Co Catalysts for low CO conversions (Jager and Espinoza, 1995).
2. The alcohols and other oxygenates are formed in negligible amounts for Co catalyst (Botao *et al.*, 2007).
3. The formation of liquid phase was assumed to be in negligible amounts compared to the amount of vapor phase products at low CO conversion (Visconti, 2014).
4. Ideal gas behaviour was assumed for gases in Ansys, while the COCO modelled real gas behaviour.

Reactor Model Assumptions:

1. The velocity across the reactor inlet is uniform.
2. The catalytic activity is constant and uniform across the catalyst zone.
3. The effectiveness factor for the catalyst is unity.
4. Porosity of the bed was taken as the porosity of the dry bed meaning it remains unaffected from the reactor conditions and was assumed to be constant and uniform across the reactor geometry.

The reactor is, therefore, assumed to operate in a single gas phase and produce no liquids or solids. It is also assumed to not produce any oxygenates as products. It is initialised with plug flow reactor conditions and is assumed to have constant and uniform catalyst activity and porosity across reactor bed.

3.3 Pressure Drop across the bed

Using Ergun equation is the most common way of calculating pressure drop inside a packed bed reactor. The pressure drop term is added to the momentum conservation equation as a momentum sink term S_m. It is given as:

$$S_m = (\Sigma\mu * v_j)/k + (\delta * \Sigma\rho * |v_j| * v_j)/2 \qquad (3\text{-}23)$$

Where μ is the dynamic viscosity of the gas; $|v_j|$ is the magnitude of gas velocity; k and δ are the permeability of the porous medium and the inertial resistance factor, respectively (Kshetrimayum *et al.*, 2016) . The definition of k and δ are provided in the Ansys Fluent Users Guide (Ansys, 2013b) as:

$$\kappa = {D_P}^2 * \varepsilon^3/(150.(1-\varepsilon)^2) \qquad (3\text{-}24)$$

$$\delta = 3.5 * (1-\varepsilon)/D_P * \varepsilon^3 \qquad (3\text{-}25)$$

The RHS in equation (3-23) consists of two terms:

1. Viscous Resistance (the first term in RHS)
2. Inertial Resistance (the second term in RHS)

The coefficients in these resistance were calculated using D_p and ε values taken from the work of Jess and Kern, 2009. These values are listed in *Table 3-4*.

Table 3-4 Values of coefficients in Viscous and Inertial Terms in Ergun Equation, bed Voidage and particle diameter

Catalyst Particle Diameter, D_p (m)	0.003m
Bed Voidage, ε	0.44
Viscous Resistance ($1/m^{-2}$)	61357376.09
Inertial Resistance ($1/m^{-1}$)	7669.67

3.4 Governing Equations for CFD

CFD codes are numerical algorithms structured to take input from the user to set up the problem and obtain the partial differential equations, solve the equations through an iterative approach and present the results graphically. These three processes are done by the three main elements of the CFD code (a) Pre-processor, (b) solver and (c) post-Processor, respectively.

These 3 elements along with conservation equations are explained in **Appendix B**.

4 Chapter - Research Methodology

4.1 Computational Set-up

The domain geometry and meshes were created using ANSYS Design Modeler and ANSYS Mesh Modeler and then imported in FLUENT for setting up the model.

4.1.1 Geometry

Two types of reactor geometries were considered for the current project, one for a tubular reactor and another for plate type reactors. The first one represents the reactor body of a single tube containing catalyst particles inside the tube. It might be a part of a multitubular reactor or could act as a standalone tube reactor for FTS. The second one represents a plate arrangement for a plate type reactor which, usually was a part of multiple plates arrangement for real reactors or heat exchangers.

Realistically, a catalytic reactor contains regular or irregular shaped catalysts which contain tortuous and irregular voids between them depending on the spatial arrangement of the bed. Catalytic reactions happen on the surface of catalysts, and therefore, an ideal reactor model geometry should include the catalyst surfaces in the geometric design to consider the actual surface area available for the reactions. However, for the sake of simplicity, surface reactions were approximated by volume reactions, and the reactions were assumed to be occurring in the entire catalyst bed volume rather than just on the catalyst surfaces. This means that the diffusion limitations in the catalyst particles were ignored by using volume averaged reaction rates.

Both the reactor geometries i.e. the plate and the tube were divided into 3 parts, a top part, a catalyst zone (porous zone), and a bottom part. The top and the bottom parts were modelled as empty spaces, which meant that pressure drop due to catalyst particles was zero in these zones. The reactions were also disabled in these zones. Their purpose was to provide some nodes in the computational domain before and after the catalyst zone, so that the boundary layer for the velocity was fully developed before entering and after leaving the catalyst zone. Difference between the top and bottom parts, and the catalyst zone was that, in the latter, the reactions occur and there was a pressure drop due to the packed bed. Their length was much less compared to the length of the catalyst zone in order to have negligible effect on the reactor parameters. *Figure 4-1* and *Figure 4-2* shows the three parts of the geometry.

Since the tube geometry was symmetrical about the cylindrical axis, the tubular reactor was treated as an axisymmetric geometry only one half of the reactor geometry on one side of the axis was modelled. The results obtained for half of the geometry could be extrapolated by rotating it 180° about the axis to obtain the results for the whole tube. So the wall on one side of the geometry represents the reactor wall while the other one represents the axis of the reactor. *Figure 4-1* shows the CFD domain geometry for a tube.

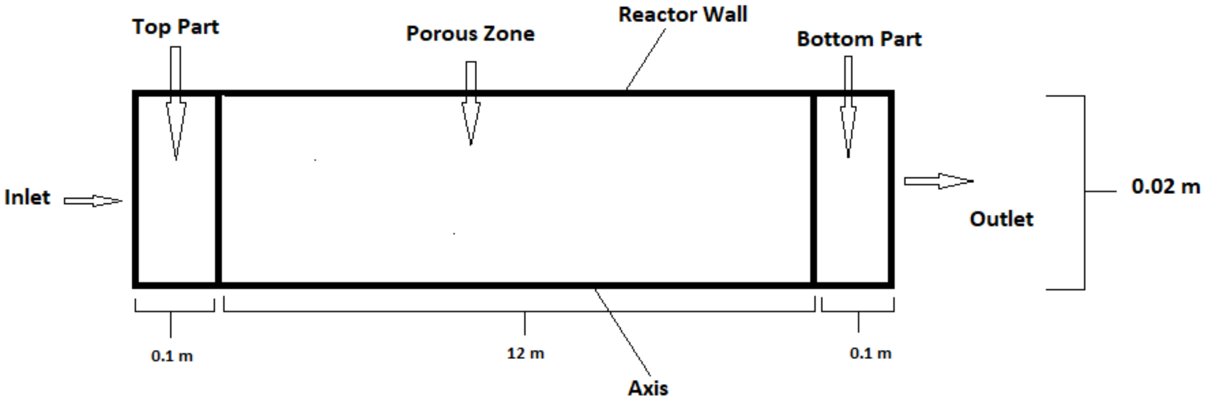

Figure 4-1 CFD domain geometry for a Tube

The plate reactor was modelled as a planar geometry, the walls of which represent the two plates between which the catalyst particles were sandwiched. The reactor walls were cooled on both sides using saturated steam and on one side for axisymmetric tubular geometry. *Figure 4-2* shows the CFD domain geometry for a plate type reactor.

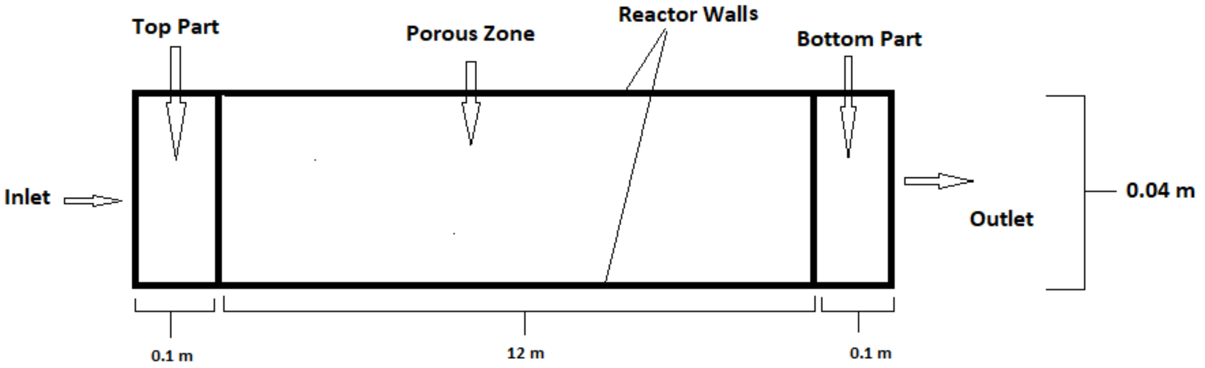

Figure 4-2 CFD domain geometry for a Plate type Reactor

The flow in the geometry was assumed to be unidirectional from the inlet to the outlet. Syngas which enters the reactor domain through inlet, passes through the top part without reacting and then it enters the catalyst zone and reacts. The products, along with the unused reactants, flow though the catalyst zone to the bottom part, which was where the reactions stop and then all species exit the reactor through the outlet. The dimensions of the base case reactor geometry i.e. length and the diameter, were taken from the work of Jess, 2012 and were given in *Table 4-1* along with the length of the top and the bottom parts.

Table 4-1 Dimensions of the Base Case Reactor geometry

S. no	Dimensions	Values
1.	Length of Catalyst zone	12.0 m
2.	Length of top part	0.1 m
3.	Length of bottom part	0.1 m
4.	Reactor Diameter	0.04 m

For 2-D geometries, ANSYS Fluent assumes a unit cell depth in the third dimension to calculate 3D quantities like volume, mass flow rate, volumetric flow rates etc. None of the flow equations were solved in third dimension for a 2D geometry. The unit depth for this computational domain was 1m into z-axis.

4.1.2 Mesh

A block-structured meshing approach was used to create mesh. The mesh consisted of only quadrilateral shaped cells. The mesh statistics for base case reactor geometry mentioned in *Table 4-1* were given in *Table 4-2*.

Table 4-2 Mesh Statistics for the base-case reactor geometry

S. no	Mesh Parameters	Values
1.	Number of nodes	8004
2.	Number of elements	6665
3.	Element Size	0.009m

Important mesh metrics that determine mesh quality were discussed below. To gain more insight into the quality of the mesh, histograms for various cell quality metrics were generated in ANSYS Mesh Modeler and were given below. These parameters were shown here for the base case mesh which was found to be independent of the grid size. The independence of the mesh was illustrated in section 4.1.3.

Aspect Ratio

The aspect ratio for a quad cell describes its deviation from a square (in terms of having all sides equal). It was given by the ratio of longer to shorter side of a rectangle approximated to the quadrilateral element. The rectangle was formed by joining the mid-points of the edges of the quadrilateral. *Figure 4-3* gives an example of the rectangle.

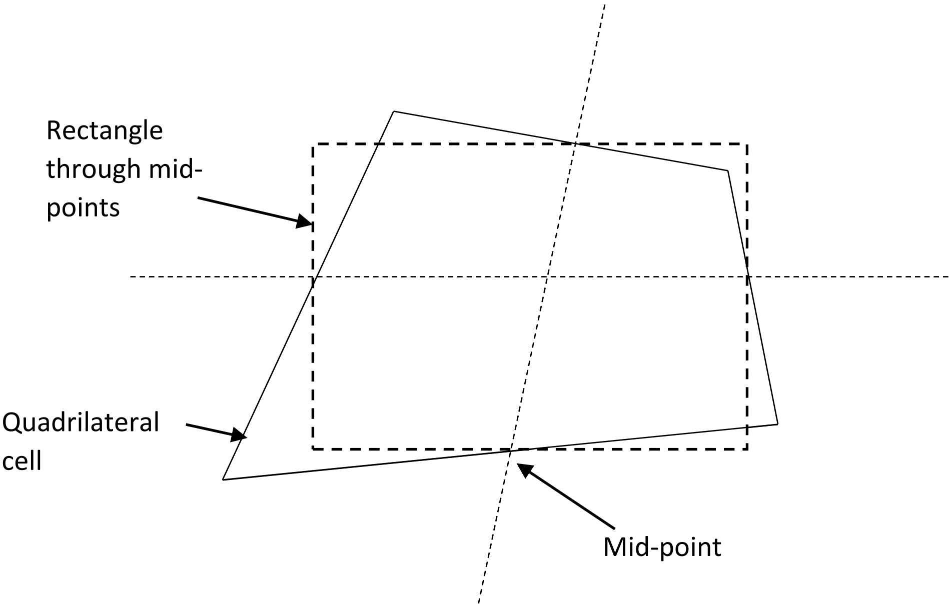

Figure 4-3 Quadrilateral Aspect Ratio Calculation

Figure 4-4 shows a distribution of the aspect ratio of the different elements in the mesh. It could be observed that all elements have an aspect ratio less than 5 which was considered good.

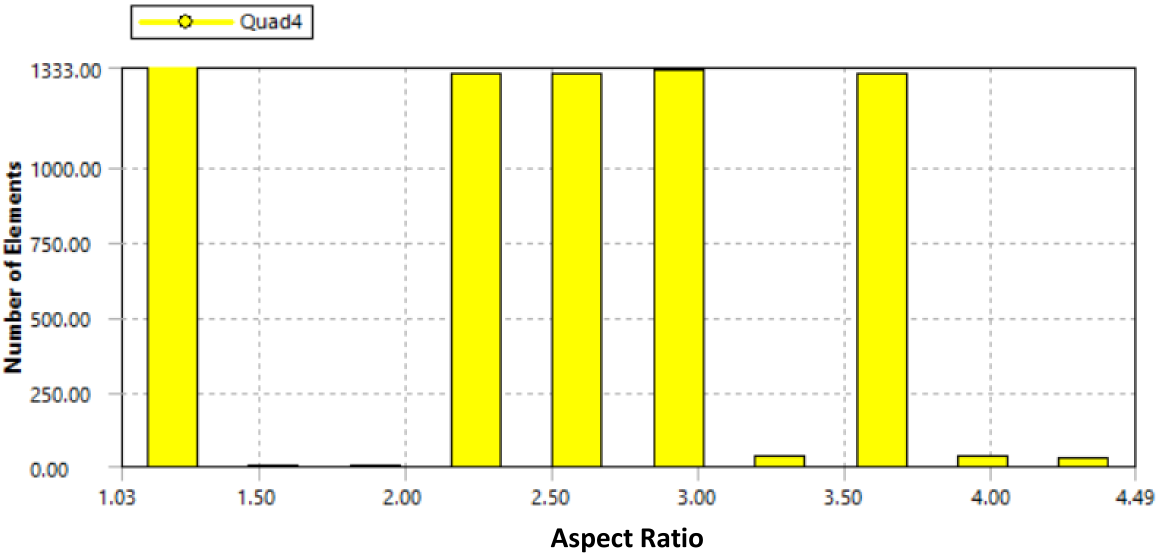

Figure 4-4 Aspect Ratio for different elements in the mesh

Skewness

Skewness of a mesh element determines how close to ideal a cell was in terms of its internal angles. *Figure 4-5* depicts ideal and skewed quadrilaterals. The skewness factor for an ideal quad was 0 and for a skewed quad was between 0 and 1. *Table 4-3* relates skewness factor to the quality of a cell which in turn represents overall mesh quality (Ansys, 2010).

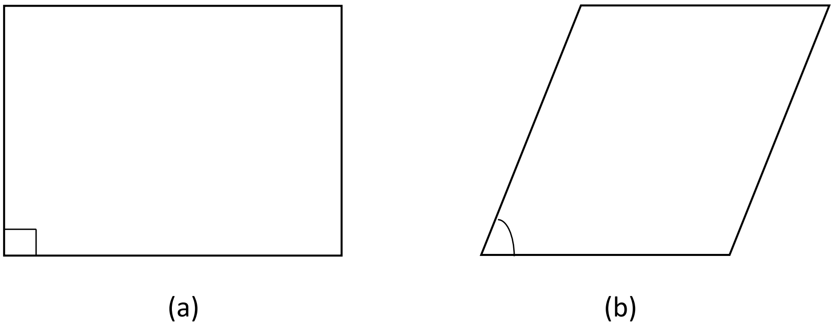

Figure 4-5 (a) Ideal Quad (b) skewed quad

Table 4-3 Relation between Skewness factor and Cell Quality

Value of Skewness	Cell Quality
1	Degenerate
0.9 - <1	Bad
0.75 - 0.9	Poor
0.5 – 0.75	Fair
0.25 – 0.5	Good
>0 – 0.25	Excellent
0	Equiangular

Figure 4-6 shows a distribution of skewness of the different elements in the mesh. It could be observed that almost all elements have a skewness of 0.01, which was close to the ideal value of 0.

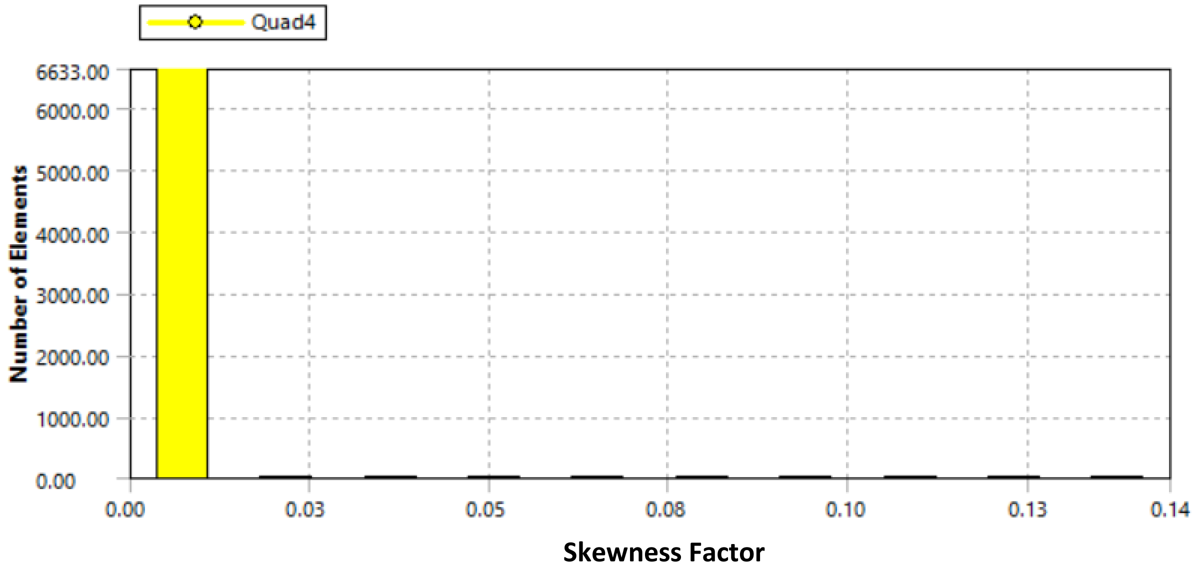

Figure 4-6 Skewness factor for different elements in the mesh

Orthogonal Quality

Orthogonal quality for cells was computed using the face normal vector $\overrightarrow{A_i}$, the vector from the cell centroid to the centroid of each of the adjacent cells $\vec{c_i}$, and the vector from the cell centroid to each of the faces $\vec{f_i}$. These vectors were depicted in *Figure 4-7* for a triangular cell.

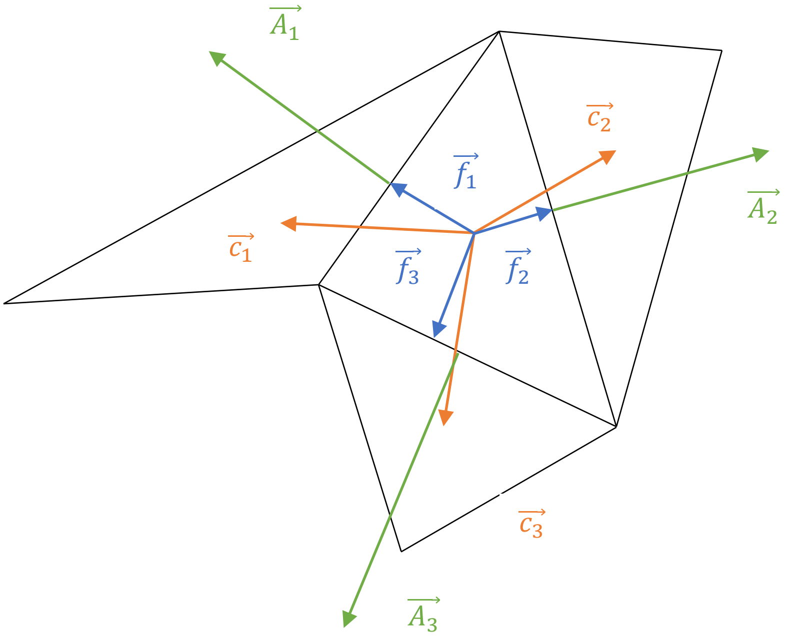

Figure 4-7 Vectors used for calculation of orthogonal quality for a triangular cell

The orthogonal quality for a cell was computed as the maximum of the following two quantities:

$$\frac{\overrightarrow{A_1}.\overrightarrow{f_1}}{|\overrightarrow{A_1}||\overrightarrow{f_1}|} \text{ and } \frac{\overrightarrow{A_1}.\overrightarrow{c_1}}{|\overrightarrow{A_1}||\overrightarrow{c_1}|}$$

Orthogonal quality for cell ranges from 0-1, 0 being the worst. Figure 4-8 shows a distribution of the orthogonal quality of the different elements in the mesh. It could be observed that most elements have an element ratio really close to 1, which was the ideal value.

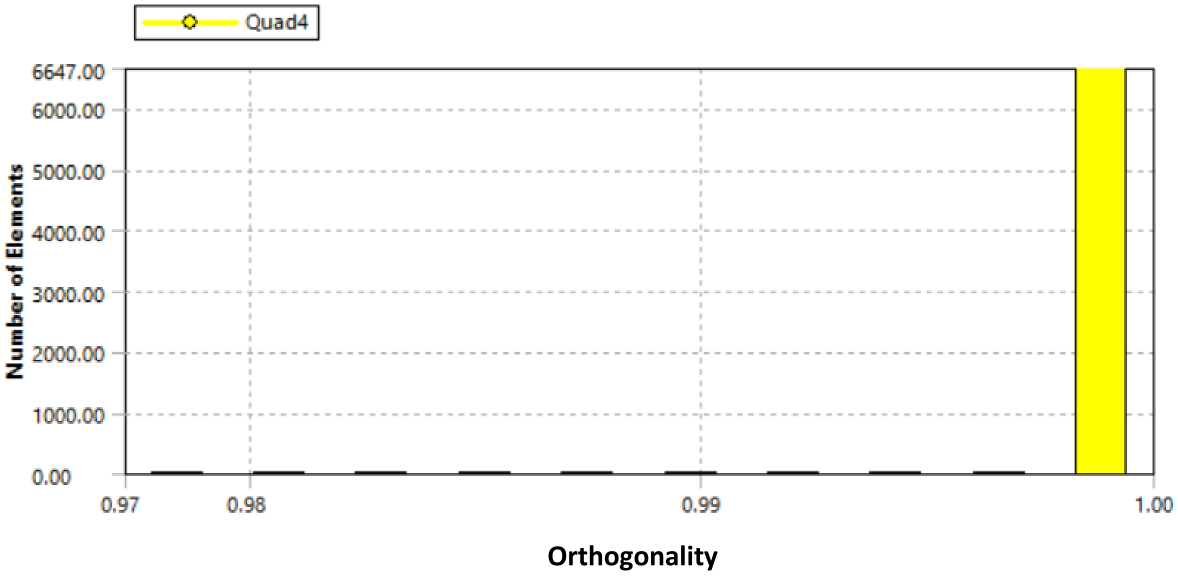

Figure 4-8 Orthogonal quality for different elements in the mesh

From *Figure 4-9*, it could be seen that the element quality of most cells was above 0.5. Hence, it could be concluded that the overall quality of the mesh was acceptable, also supported by the abovementioned parameters. The two aspects that characterise successful simulation result were convergence and grid independence. The only way to eliminate errors due to coarseness of a grid was to perform a grid dependence study, which was a procedure of successive refinement of an initially coarse grid until certain key results do not change. Then the simulation becomes independent of the grid. Systematic search for grid-independent results forms an essential part of all high-quality CFD studies. The following section briefly explains the grid independence study done on the mesh of the base case geometry.

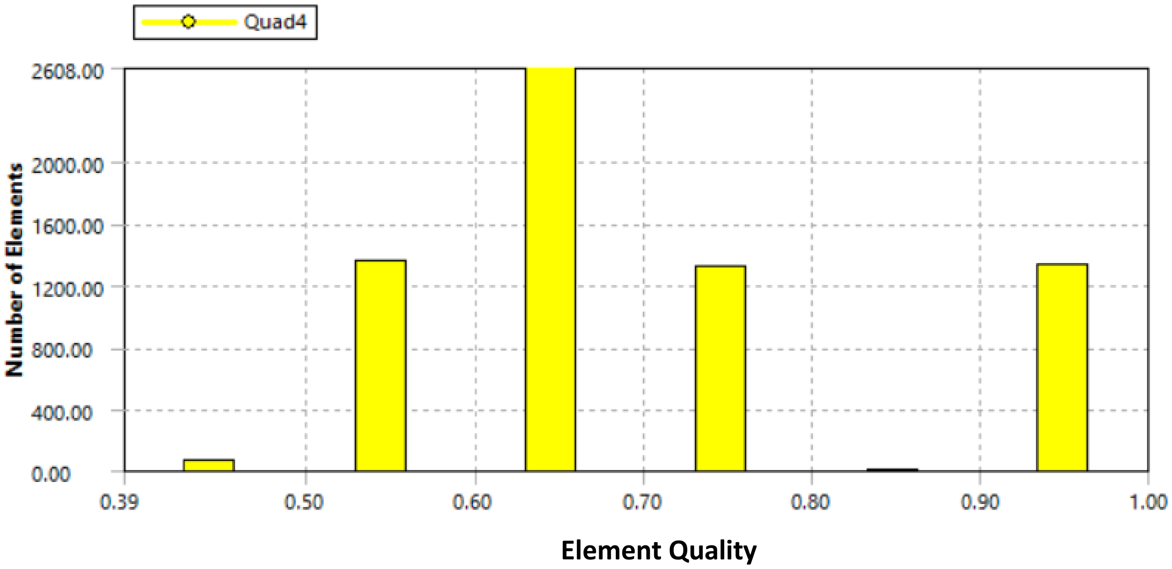

Figure 4-9 Element quality for different elements in the mesh

4.1.3 Mesh Independence Study

Prior to performing the parametric CFD simulations, a grid independence study was conducted over 8 grid resolutions. Since species concentration and temperature over the reactor length play key roles in this study, mesh dependence was checked for mass fraction of Carbon Monoxide(CO) at the reactor outlet and the hotspot temperature as parameters.

For mesh independence test, the element size was chosen as the independent variable. It was decreased from an initial value of 0.03m to 0.005m in 7 steps. *Table 4-4* shows a summary of successive refinement runs for the mesh independence study. *Figure 4-10* show response of CO concentration (at the reactor outlet) and hotspot temperature to the changing element size. A mesh having element size of 0.03m was too coarse and gave highly oscillating values for all the residuals. Hence, converged results could not be obtained for it. The results for this element size were thus, not included in the *Table 4-4*.

As it could be seen from *Figure 4-10* and *Table 4-4* that refining the grid for an element size more than 0.009m ceases to show any effective change on the temperature and CO concentration. Although fine meshes could be chosen but they increase the computation time excessively in exchange for negligible increase in accuracy. Hence, for all the further simulations, 0.009m was considered sufficient element size for convergence. Absolute and relative errors in concentration and temperature were calculated relative to the results of mesh having element size 0.009 m. All the relative errors were less than 0.01%. Thus, 0.009 could be safely employed as the element size.

Table 4-4 Mesh Independence Study

Element Size	No. of cells	No. of nodes	CO mole frac	Hotspot Temp.	Abs. Error	Relative Error(%)	Abs. Error	Relative Error(%)
0.03	1995	2400	~	~	Temperature		CO Mole fraction	
0.015	4005	4812	0.4976	494.943	0.0012	2.42E-4	-6E-4	-0.0012
0.01	6000	7206	0.4972	494.9442	0	0	-2E-4	-0.0004
0.009	6665	8004	0.496996	494.9442				
0.008	7509	9014	0.497025	494.9445	-0.0005	-1.01E-04	-2.9E-05	-5.8E-03
0.007	8570	10290	0.496993	494.9444	-0.0004	-8.08E-05	2.8E-06	5.63E-04
0.006	11980	13985	0.497	494.9445	-0.0005	-1.01E-04	2.8E-06	5.63E-04
0.005	14400	16807	0.49705	494.9445	-0.0005	-1.01E-04	-5.4E-05	-0.011

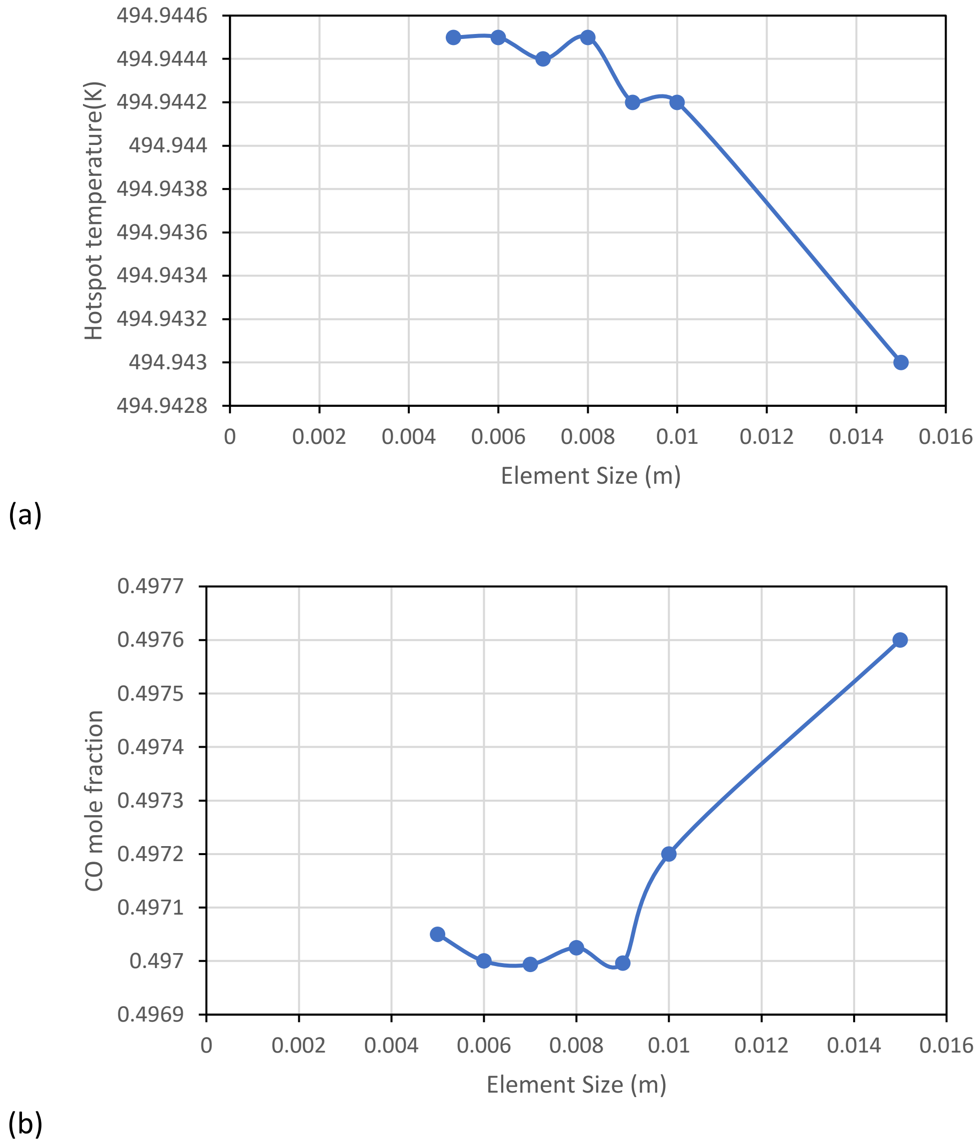

Figure 4-10 Response of (a) Hotspot Temperature (b)CO mole fraction at outlet for various mesh element sizes

4.1.4 Boundary Conditions and Cell Zone

Boundary conditions were various constraints applied to a boundary Value problem so that the differential equations could be solved within the domain. For the current geometry, the following boundary conditions were applied to various boundaries.

Inlet

The inlet was assigned a Velocity Inlet Boundary Condition (B.C.). This B.C. was used to define the flow velocity along with other relevant scalar properties of the flow at flow inlets. The stagnation pressure could rise to whatever value necessary to provide the prescribed velocity distribution.

Velocity magnitude, temperature and the species mole fractions were provided for the velocity boundary condition as shown in *Table 4-5 Input values for the Velocity Inlet Boundary Condition*. The superficial velocity and the H_2/CO molar ratio used in this project was taken from the work of Jess, 2012. The catalyst density and the porosity for the catalyst bed was taken as 700 kg/m^3 and 0.44 respectively. All the values in *Table 4-5 Input values for the Velocity Inlet Boundary Condition*, except the inlet temperature and steam temperature, were kept constant throughout the project. The inlet temperature and steam temperature shown in *Table 4-5 Input values for the Velocity Inlet Boundary Condition* were for the base case design.

Table 4-5 Input values for the Velocity Inlet Boundary Condition

S.no.	Input Parameter	Value
1.	Velocity Magnitude [m/s]	0.55 m/s
2.	Inlet Temperature [K]	493.15
3.	Steam Temperature [K]	493.15
Species Concentrations		
S.no.	Species	Mole Fractions
1.	CO	0.333
2.	H_2	0.667
3.	H_2O	0.0
4.	Paraffins: C_1…….C_{20}	0.0
5.	Olefins: C_2…….C_{20}	0.0

Ansys Fluent uses the above-mentioned inputs at the inlet to compute the mass flow into the domain through the inlet and to compute the fluxes of momentum, energy and chemical species entering the domain. The mass flow rate $\dot{m}$ entering a fluid cell adjacent to the inlet boundary was computed as:

$$\dot{m} = \int \rho\vec{v} \cdot d\vec{A} \tag{4-1}$$

Only the component of velocity normal to the control volume face contributes to the inlet mass flow rate. The velocity used in this project was normal to the flow area.

Outlet

The outlet was assigned the pressure outlet B.C. In this B.C., static pressure needs to be specified at the outlet boundary along with other required inputs. The Operating Pressure was set to 24 Bar.

Walls

No-slip condition was used for the velocity of the gas flowing on the walls. Wall thickness was not taken into account. The walls were assumed to be surrounded by saturated steam as the cooling medium. Temperature of the steam outside the walls was taken to be 493.15 K for the base case design.

4.2 Solver Type

Two types of numerical methods were available in Ansys Fluent:

1. Pressure-based Solver
2. Density-based Solver

Density based approach was historically employed for high-speed compressible flows while the pressure-based approach was developed for low-speed incompressible flows. However, both the methods have been expanded to solve both kinds of flows beyond their traditional intent (Ansys, 2013a).

Both the methods generate velocity from the momentum equations. In the density-based approach, density field was obtained from the continuity equation, but the pressure field was solved using the equation of state.

In the pressure-based approach, the pressure field was solved by using a pressure correction equation. This approach was used in this project as the velocity used here falls in the subsonic region. Pressure and Density based approaches have been explained in **Appendix C**.

4.3 Spatial Discretisation Schemes

Computational simulation involves solving of partial differential equations. The latter were converted to algebraic equations using discretisation methods. There were various methods available for discretisation. Some examples were Finite difference Method, Finite Element Method and Finite volume Method. Finite volume approach was utilised in this project. It was the first step, the control volume integration, which distinguishes the finite volume method from all other CFD discretisation techniques. It was given in **Appendix D** along with an example.

4.3.1 Pressure-Velocity Coupling

Pressure-velocity coupling method obtains the pressure field using the relationship between velocity and pressure corrections to enforce mass conservation. It was achieved by using the discretised continuity equation to derive an additional condition for pressure by reformatting the continuity equation (B-2). The SIMPLE method described and used here was based on a predictor-corrector approach. It was also shown in **Appendix D**.

4.4 Solution Controls

4.4.1 Relaxation

The under-relaxation factors were employed to suppress the oscillations in the flow solution which result from the numerical errors. They under-relax the change that was implemented in the scalars calculated from the governing equations per iteration. This slows down the convergence, but the steady state solution remains unaffected. High under-relaxation factors fasten the convergence, but they decrease the stability of the simulation, which means instability in the form of divergence or oscillations might increase. So, a balance was required between by tuning the under-relaxation factors to optimise the computational effort and stability. Steady state solution was achieved using the following under-relaxation values for the current project as shown in *Table 4-6*.

Table 4-6 Values of the Under-Relaxation Factors

S.no.	Under-relaxation Factors	Values
1.	Pressure	0.2
2.	Density	0.8
3.	Body Forces	1
4.	Momentum	0.6
6.	Species	0.8
7.	Energy	0.6

4.5 Initialisation

An initial guess value for the flow variables like velocity, pressure, temperature, volume fraction of different phases and concentrations of species was required for the solution flow field for all cells. However, a steady state solution was independent of the initialisation conditions provided the system was non-oscillatory. *Figure 4-11* shows all the residuals for the steady state, from 19000 iterations to 24000 iterations. It could be observed that the residuals do not oscillate and decrease monotonously near the end. Standard initialisation method was employed in the current project, and the initial values were set same as the values set for the inlet boundary condition for the entire reactor geometry. There were two main methods by which initial fields could be defined in Ansys Fluent: Standard Initialisation and Hybrid Initialisation were explained in **Appendix D**.

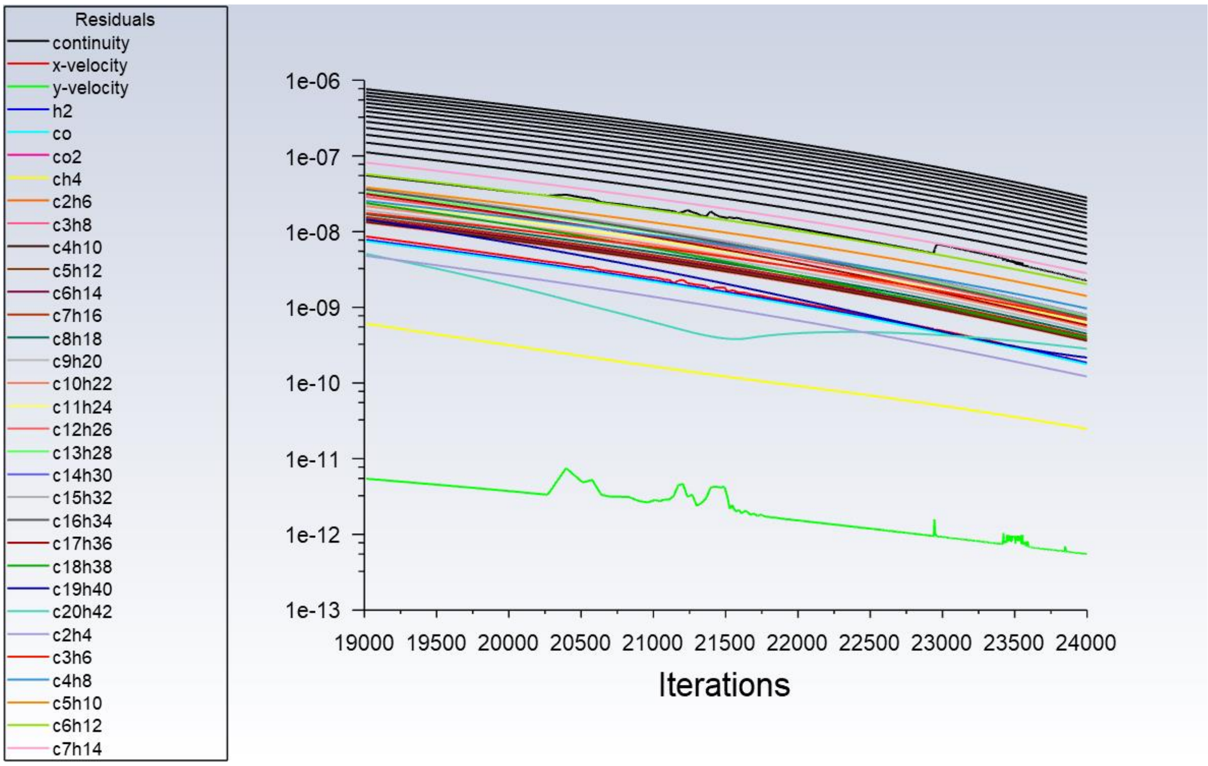

Figure 4-11 Non-Oscillatory nature of the residuals

4.6 Solution Convergence

The iterative process for finding a solution to the PDEs was repeated until the change in the values of a field variable between two consecutive iterations was so small that the system could be assumed to have reached a steady state. At convergence condition, the mass, momentum and all the scalar balances were achieved across all the boundary conditions and the solution no longer changes with additional iterations. Residuals measure the imbalances or errors in the conservation equations.

$$R_p = \left| a_P \phi_P - \sum_{nb} a_{nb} \phi_{nb} - b \right| \tag{4-2}$$

These residuals were calculated for the continuity, momentum, and specie conservation equations. At steady state conditions, these residuals were found to be extremely small. The steady state was achieved after approximately 8000 iterations for an isothermal case and 15000 iterations for a case with heat transfer.

4.6.1 Convergence Criterion

The convergence criterion for the residuals in a steady state solution were set as shown in Table 4-7. The convergence criterion values were absolute values. The choice of the criterion values was based on the relative error being 3 orders magnitude smaller than the species' concentration values.

Table 4-7 Convergence criteria for Residual values

S.No.	Quantities	Criteria for Residuals
1.	Continuity	$<10^{-8}$
2.	x-velocity	$<10^{-11}$
3.	y-velocity	$<10^{-12}$
4.	Energy	$<10^{-12}$
5.	Species	$<10^{-9}$

The residual for species was set to be less than the order of 10^{-9} as the lowest species concentration was found to be of the orders of 10^{-6}. The residuals being 10^{-3} times smaller than the species concentration makes the relative errors to be approximately 0.1% for the species with the lowest concentration.

$$\frac{\text{Residuals}}{\text{Species Concentration}} = \frac{10^{-9}}{10^{-6}} = 10^{-3}$$

This represents the worst-case scenario. Many cells had the relative error lesser than 10^{-3}. In addition, Species which have concentrations higher than 10^{-6} had the relative error much lesser than 0.001.

4.7 Tube Reactor vs Plate Type Reactor

A comparison was carried out between the plate type reactor and tube reactor on the basis of heat transfer capabilities. The length of the catalyst bed was kept same for both the geometries i.e. 12m. Other parameters like inlet velocity, temperatures etc. were all kept identical and constant for both the geometries.

There were two criteria applied to carry out the comparison between the two geometries. The first criterion was based on the physical similarity which included having equal surface-to-volume ratio for the two geometries. The second criterion was based on the catalyst loading in the reactor and included having equal tube-to-diameter ratio for the two geometries. Both the criteria were explained below.

4.7.1 Comparison on the basis of Surface Area to Volume Ratio

To obtain physical similarity, there were two criteria used for comparing a tube geometry to a plate geometry. The first criterion was based on having equal Reynolds number for both geometries. Since the factors on which the Reynolds number for a packed bed depends on, were all the same for both the geometries, by default, Reynolds Number is same for both the geometries. This criterion for comparison is explained in Appendix H.

Another criterion for comparison was related to having equal surface areas available for heat dissipation per unit volume of heat producing zone. Hence, surface area to volume ratio for both geometries were equated. With this constraint, for a tube of diameter D and a plate type reactor with a plate spacing t, equation (4-3) was obtained. The derivation for equation (4-3) is given in Appendix H.

$$D = 2t \tag{4-3}$$

Hence, a plate type reactor with a plate spacing t and a tube of diameter D = 2t (or radius, r = t) were compared for their heat transfer capacities.

4.7.2 Comparison on the basis of Tube-to-Particle Diameter Ratio

Most references in literature, that claim plate type heat exchangers to be better than shell and tube heat exchangers, were for non-reactive systems. For such systems, physical similarity of the two geometries is usually considered the major comparison criterion. However, for reactive systems, physical similarity along with reaction dynamics were important parameters to consider.

Tube-to-particle diameter ratio, n, is considered an important FBR design parameter in finding the optimum trade-off between the catalyst loading/packing and the product yield of the long chain hydrocarbons. Most exothermic catalytic reactions in industries were carried out using wall cooled tubular reactor with a low n (Chandra *et al.*, 2021).

A comparison on the basis of Tube-to-Particle diameter ratio was carried out. There is a limitation on the lowest possible diameter for a tube reactor or a plate reactor of accommodating a minimum of 10-15 catalyst particles along the tube diameter or the plate spacing. Since the catalyst particle diameter used in this project is 0.003m, that sets the lowest possible tube diameter or plate spacing to be 0.03m. Corresponding tube radius for a plate spacing of 0.03m is a tube of radius 0.03m (r = t) according to the comparison criterion given in section 4.7.1. However, according to the tube-to-diameter particle ratio criterion, the lower limit on the tube diameter is 0.03m. A comparison between the tube of diameter 0.04m and a plate of plate spacing 0.04m was carried out in section 5.4.2 to compare their heat transfer capabilities when compared on tube-to-particle basis. A tube of diameter 0.04m and a plate of plate spacing 0.04m could accommodate equal number of catalyst particles along the diameter or plate spacing respectively, hence resulting in equal catalyst packing.

Part 3: Results and Conclusion

5 Chapter - Results and Discussion

As mentioned previously in chapter 1, the objectives of this project included developing a steady state CFD model for FTS using a partial equilibrium approach kinetics for isothermal and non-Isothermal conditions for a tubular geometry. The next objective was to analyse the results obtained and compare the model with a 1-D mathematical model. As a next step, the developed model was adapted for a plate type reactor and the results compared with the results of a tubular geometry. Based on the results from the comparison, parametric studies were carried out to study the effect of diameter and plate spacing on the heat transfer properties of the tubular geometry and the plate geometry respectively.

The results in the following sections were given in the same order as the above-mentioned objectives. Each result was followed by its analysis and discussion. Before the results analysis, mass and energy balances were analysed to ensure that mass and energy imbalances were within the tolerances set by the solvers in the model at various conditions.

5.1 Model Justification

Model verification and validation is the primary means to assess the accuracy and reliability of a CFD simulation. At the end of the simulation, the user must make a judgement whether the results are ‘good enough’ (Oberkampf and Trucano, 2002).

The fundamental strategy of model verification is the identification and quantification of the errors in a CFD solution. The verification activities involve two types of measurements, one relative to analytical solutions and the other relative to highly accurate numerical solutions (Oberkampf and Trucano, 2002). Analytical solution for such a complicated problem involving more than 40 chemical species was extremely difficult to obtain. Hence, verification with a numerical solution obtained through another opensource software was carried out here.

The base case model described in the previous chapter, was run without any reactions occurring in the reactor as the first step in this chapter. This was done to check if the mass and energy balances hold true and check for any errors in the model before proceeding to the complex simulations with reactions.

5.1.1 Mass Balance

5.1.1.1 No reaction

Results for the mass flow rate through the model presented a net change of - 1.70195 x 10^{-10} and a relative change of a relative change of 0.000004% was observed for mass flow rate. Such small change can be attributed to the numerical errors and the computational errors and, therefore, can be neglected. Thus, it can be safely concluded that mass balance was established in the model.

Due to absence of reactions, the products were absent, and the reactants kept flowing throughout the reactor. The walls were kept at constant temperature. There was a pressure drop applied to the gas flow along the axis due to the catalyst zone formulations according to the Ergun equation as mentioned in Chapter 3. Therefore, pressure can be seen to be decreasing along the reactor length. The total drop in pressure was approximately 95 kPa which was 4% of the operating pressure. The effect of the pressure drop on the reactions was insignificant. Since, the top and bottom zones do not have the catalyst zone formulations, the drop in pressure was absent in these zones. A plot of pressure along the reactor axis was presented in Figure 5-1.

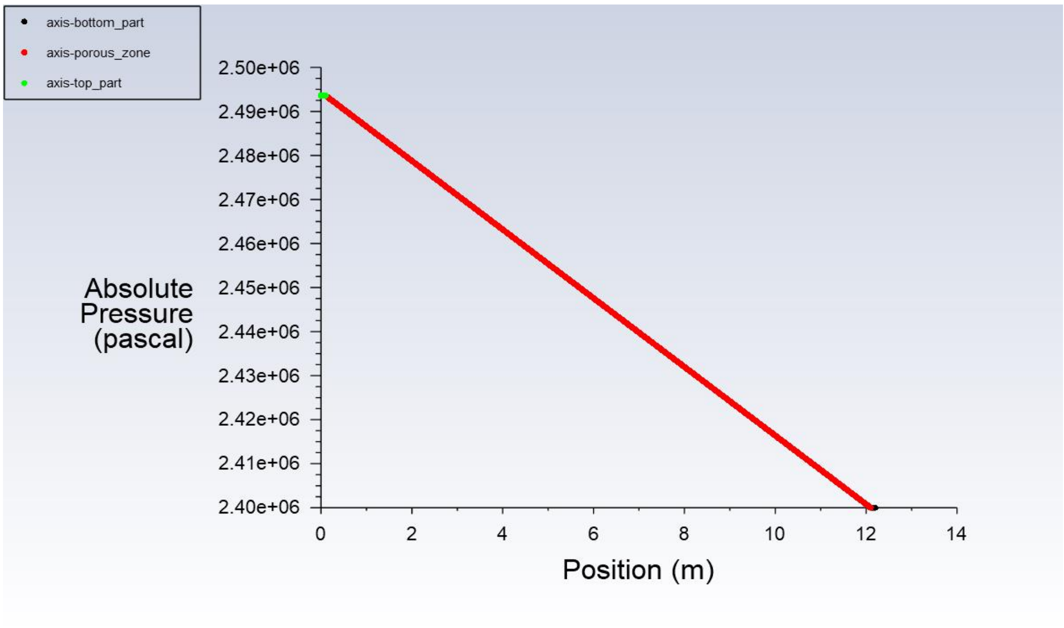

Figure 5-1 Pressure along the Reactor Length

As a next step, the model was run with all the reactions for isothermal conditions at various temperatures.

5.1.1.2 Isothermal Case with Reactions

The temperature range for low temperature FT reactions was usually considered from 200°C to 240°C. A temperature above this range falls in the HTFT reaction category. Simulation runs were, thus, carried out from 200°C to 240°C in intervals of 20°C.

Mass flow rates to the reactor inlet at 200°C, 220°C and 240°C were found to be 4.49 x 10^{-3} , 4.32 x 10^{-3} and 4.15 x 10^{-3} respectively. As the feed temperatures were changed for various isothermal runs (and non-isothermal runs in the following sections), it resulted in reduced mass flow rates to the reactor as the velocity was kept constant across all simulations in this project. This increased the W/F ratio i.e. Weight of the catalyst/Flow rate as the Flow rate was decreased. The W/F ratio was an important parameter that determines CO conversion in a packed bed as the design equation for a packed bed was given by equation (5-1).

$$\frac{dF_A}{dW} = -r_A \tag{5-1}$$

However, this effect on CO conversion was very small (linear) compared to the effect of increasing temperature which increases CO conversion exponentially. Therefore, velocity was kept constant across all the simulations.

The values of net change in mass flow rates at 200°C, 220°C and 240°C were found to be 2.16 x 10^{-12} kg/s, 3.06 x 10^{-12} kg/s and -7.26 x 10^{-12} kg/s respectively. Compared to the mass flow rates to the inlet, the net changes in the mass flow rates were negligible. Thus, it was concluded that the mass balance was satisfied for isothermal conditions within the limits of machine precision at all three temperatures.

5.1.1.3 Non-Isothermal Case with Reactions

After running the model with isothermal conditions, it was then simulated at non-isothermal conditions as the next step for the same feed temperatures as the isothermal setup i.e. 200°C, 220°C and 240°C.

Mass flow rates to the reactor inlet were kept same as the isothermal cases. The net changes in the mass flow rates at 200°C, 220°C and 240°C were found to be 7.52 x 10^{-12} kg/s, 2.28 x 10^{-11} kg/s and 1.09 x 10^{-11} kg/s respectively.

Compared to the mass flow rates to the inlet, the net changes in the mass flow rates were negligible. Thus it was concluded that the mass was conserved at all mentioned temperatures in isothermal as well as non-isothermal conditions.

5.1.2 Energy Balance

5.1.2.1 Non-Isothermal Case

The model was simulated with heat transfer enabled in the system, as the next step for the feed temperatures of i.e. 200°C (473.15K), 220°C (493.15K) and 240°C (513.15K). For these non-isothermal cases, the walls were kept at a constant temperature which was equal to the feed temperature. The walls were assumed to be surrounded by saturated steam as a cooling medium. The heat transfer coefficient from the reactor's outer surface to the bulk of steam was taken to be 10,000 w/m^{2}k as the nucleate boiling heat transfer coefficient for Ansys calculations (Welty *et al.*, 2000). The steam temperature was kept equal to the feed temperature for each simulation in the entire project. The overall heat transfer coefficient was a function of 3 heat transfer coefficients as given in equation (5-2).

$$\frac{1}{U_{overall}} = \frac{1}{h_1} + \frac{t}{\lambda} + \frac{1}{h_2} \qquad (5\text{-}2)$$

where

h_1	Heat transfer coefficient from reaction mixture to reactor's inner surface
h_2	Heat transfer coefficient from reactor's outer surface to the coolant steam
t	Wall thickness of the reactor
λ	Thermal conductivity of the wall

Since the reactor wall's thickness was assumed to be negligible, the heat transfer coefficient from reactor's inner to outer surface was considered negligible. h_1 was calculated in Ansys based on material properties. Results for the heat transfer rate through the various zones of the model was presented in *Table 5-1*.

Table 5-1 Energy Flows in the various zones of the CFD model for the non-isothermal condition

Total Heat Transfer rates (w) at different temperatures			
Boundaries	200°C	220°C	240°C
Inlet	2.15327×10^{3}	2.30404×10^{3}	2.44344×10^{3}
Outlet	-1.97606×10^{3}	-1.94838×10^{3}	-1.88973×10^{3}
Wall-Top Part	-1.58816×10^{-5}	-0.21558×10^{-5}	-8.74723×10^{-5}
Wall- Catalyst zone	-5.24234×10^{3}	-9.41773×10^{3}	-1.34639×10^{4}
Wall-Bottom Part	-1.74999×10^{-1}	-2.15588×10^{-1}	-1.61597×10^{-1}
Heat of Reaction Source	5.06230×10^{3}	9.06228×10^{3}	1.29104×10^{4}
Net Heat Transfer Rate	-1.98682×10^{-5}	1.46334×10^{-4}	2.34644×10^{-4}
Relative Change (%)	9.22699×10^{-7}	6.35119×10^{-6}	9.60302×10^{-6}

Since the steam temperature was same as the feed temperature, negligible heat transfer (~10^{-5}) takes place in the top part as there was no source of heat present. In the catalyst zone, the reaction heat was produced, and hence, significant amount of heat transfer takes place in the catalyst zone as well as the bottom part. A relative change less than 0.00001% was a small change that can be attributed to the numerical errors and the computational errors, and hence, can be neglected. The amount of heat generated from the reactions and the heat dissipation through the walls of catalyst zone were nearly equal at all temperatures. This simulation was carried out for very thin tube of diameter 0.04m and hence, 95% of the reaction heat was dissipated to the cooling medium effectively. But as the diameter increases, heat dissipation becomes challenging. This was shown in detail in the following sections.

From the above discussion, it can be safely concluded that mass and energy were conserved in the model. The model was thus physically meaningful and thermodynamically consistent. Thus, the model represents a good foundation to carry out further testing.

5.2 Isothermal Case

The result for isothermal runs for a tubular reactor of diameter 0.04m for steam temperatures of 200°C, 220°C and 240°C was presented in this section in the form of CO conversions and product distributions. CO conversions were calculated on the basis of consumption of the specie CO for all the simulations in this project.

5.2.1 CO conversion

CO conversions at different steam temperatures were calculated for isothermal conditions and were given in *Table 5-2*. CO conversion was seen to be increasing with the temperature in the reactor as the higher reaction rates were observed as the temperature rises.

Table 5-2 CO conversions at different temperatures for isothermal conditions

Temperature	CO conversion (%)
200°C	23.1
220°C	42.6
240°C	62.6

5.2.2 Product Distribution

Figure 5-2 shows the mole fractions of paraffins and olefins from C_1 to C_{20} and C_2 to C_{20} respectively at different temperatures. These quantities were reported for the outlet of the reactor. The concentrations were found to not change much across the outlet, therefore, the concentration at the centre of the outlet was taken as a representative value for the outlet concentration.

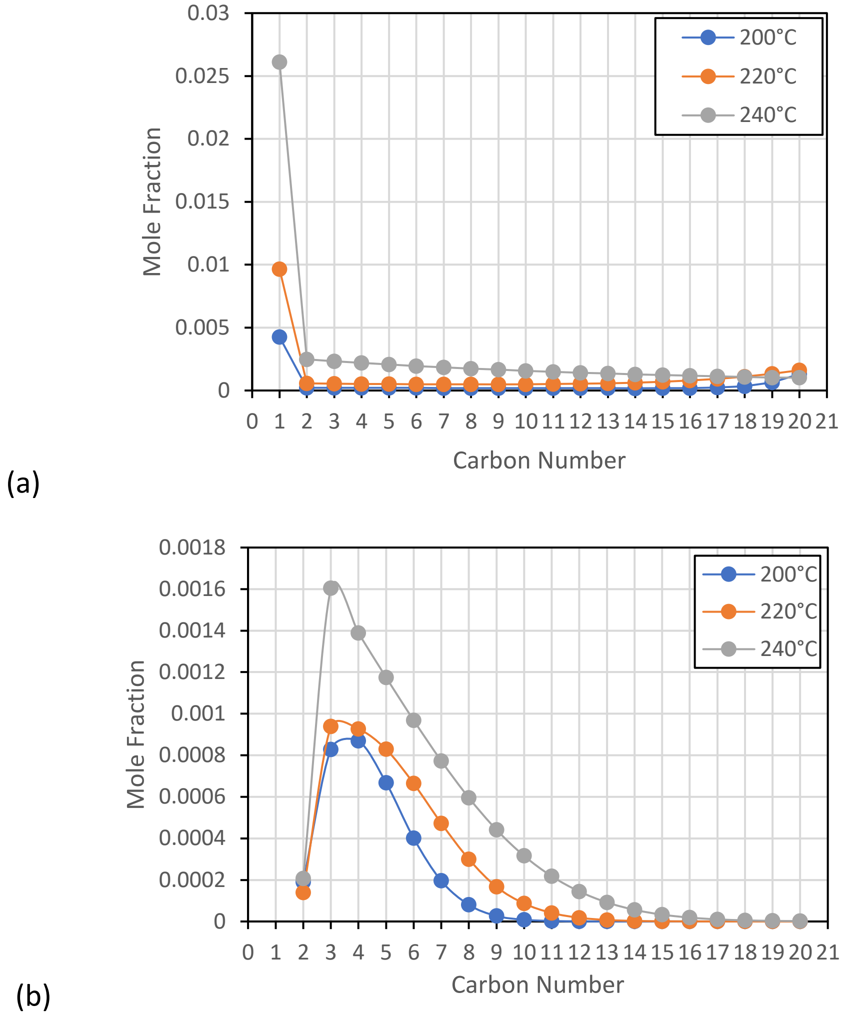

Figure 5-2 Mole fraction for (a) Paraffins (b) Olefins at different temperatures for isothermal condition. The CO conversions for 200°C, 220°C and 240°C were 23%, 42.5% and 62.64% respectively.

The product distribution obtained in Figure 5-2 deviates from the ideal ASF product distribution. The major reason behind this behaviour was the truncation of the homologous series of Paraffins and Olefins at n=20. To reduce complications, the model was truncated to solve for 20 species of paraffins and olefins while the original model had been developed and tested for n = 80. The truncation, however, serves as a limitation of the model and its effect can be observed in the form of increased mole fractions of the upper end of the paraffins series from Figure 5-2(a). This effect was more pronounced for the lower temperatures. This phenomenon has been explained in

Appendix **F**. However, since the truncation does not affect other aspects of the reactor, it can be used to demonstrate the effect of geometry on the reactor performance.

Comparing the mole fractions of paraffins and the olefins, it can be observed that the olefins have low yield than the paraffins. This can be attributed to the saturated products being the thermodynamically favoured one. Increasing temperature from 200°C to 240°C can be seen to have increased the CO conversion. Apart from increased CO conversion, selectivity seems to have changed with increased temperature. It has shifted towards the middle species from the higher carbon number species in the homologous series for paraffins as well as olefins.

5.2.3 Comparison between 1-D and 2-D for Isothermal Case

The kinetic formulations and the operating conditions used in Ansys were used to reproduce a 1D model in a chemical flow sheeting software COFE by Cape-Open to Cape-Open (COCO) Simulator (van Baten *et al.*, 2022). It was developed to obtain a numerical solution that could be used to compare and justify the CFD results from Ansys.

There were two major differences between the models developed in using the two softwares. Unlike Ansys, PFR model simulates a 1D model and hence represents a plug flow reactor. The other difference between the models was that, in COCO, real gas behaviour was considered, while for Ansys, ideal gas behaviour was used. The reason behind this assumption was the inaccessibility of fugacities in a UDF in Ansys. In order to consider the real behaviour for gases in Ansys, species' fugacities needed to be accessed in the UDF which was not allowed in Ansys Fluent. Even though Peng Robinson Equation of state model was present in fluent to be used to model real gas behaviour, it was not possible to couple it with the complex kinetics used here, inside a UDF. Hence, the gases were assumed to be ideal. The isothermal runs carried out in COCO were at same temperature values: 200°C (473.15K), 220°C (493.15K) and 240°C (513.15K) as in Ansys. The CO conversions for both the cases were shown in *Table 5-3*.

5.2.3.1 CO conversion for Isothermal Conditions

Table 5-3 CO conversions at different temperatures for COCO and Ansys

CO conversion (%)			
Inlet Temp. (°C)	Ansys	COCO	Relative Change (%)
200	23.09	21.98	4.82
220	42.56	41.39	2.74
240	62.64	62.28	0.57

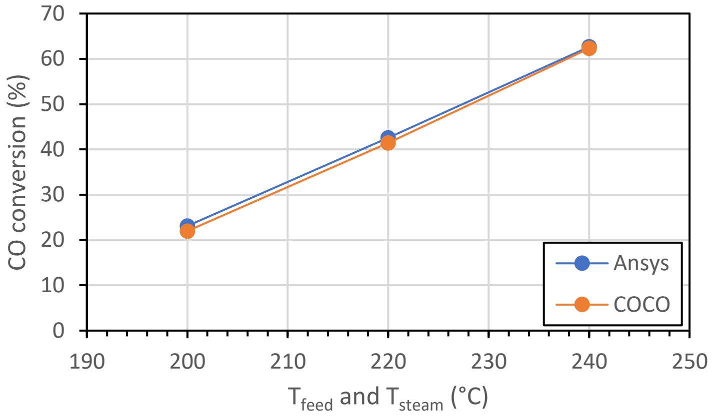

Figure 5-3 CO conversions vs Temperature for different softwares

Figure 5-3 shows that CO conversions in the 2 softwares were close. The relative variation in COCO and Ansys was less than 5%. Hence, it's safe to say that the kinetics was working properly for isothermal conditions.

5.2.3.2 Product Distribution at Isothermal Conditions

The plots in Figure 5-4 (a) – (c) compare the product distributions of paraffins and olefins obtained in Ansys and COCO for isothermal runs for a tubular reactor of diameter 0.04m at different temperatures 200°C (473.15K), 220°C (493.15K) and 240°C (513.15K). The plots on the left side of (a), (b) and (c) of Figure 5-4 represent the paraffins series whereas olefins were represented on the right side.

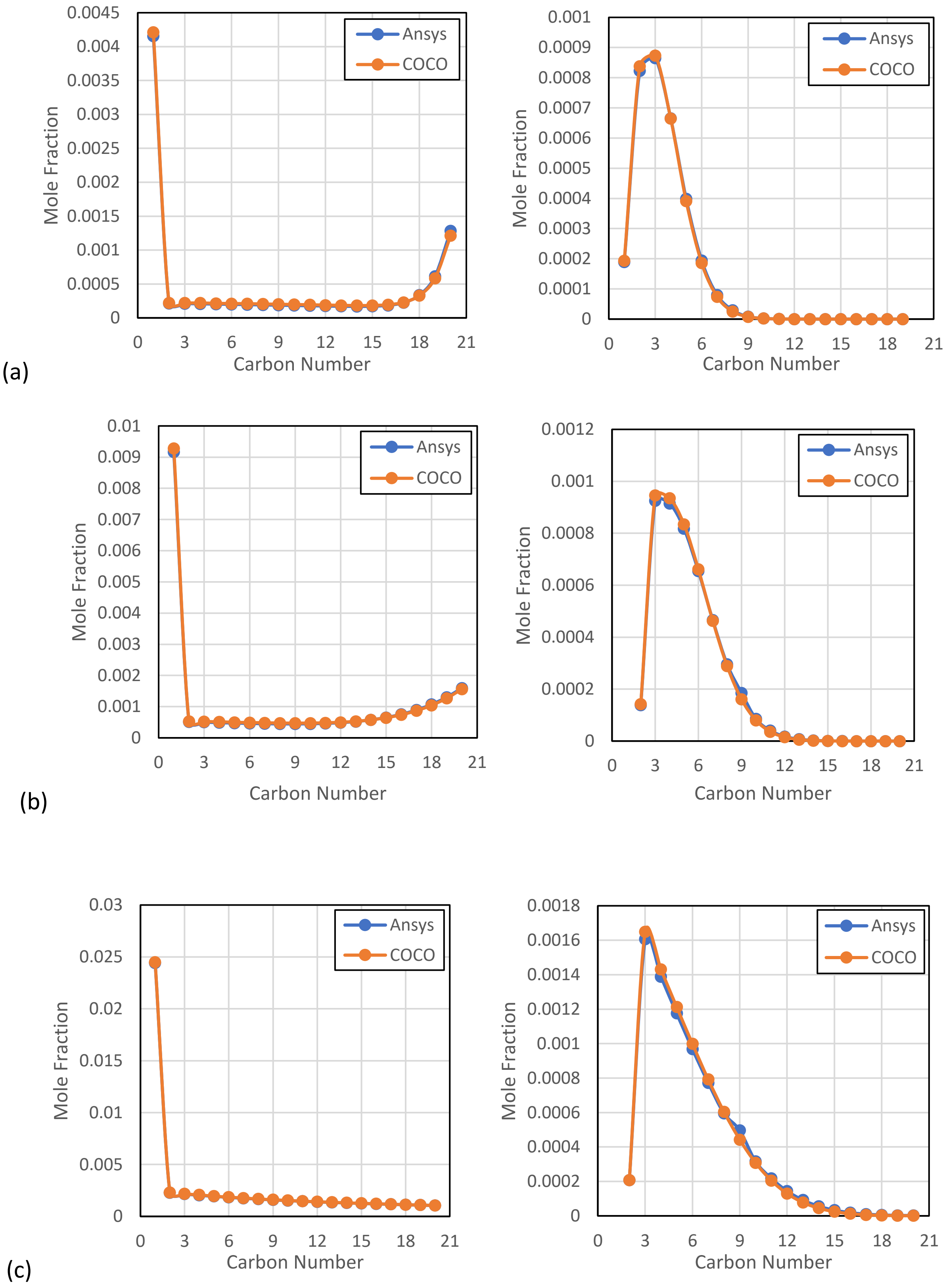

Figure 5-4 Product Distribution of a tubular reactor of diameter 0.04m at isothermal conditions at (a) 200°C (b) 220°C (c) 240°C. The pictures on left represent mole fractions of paraffins and olefins were represented on the right side

The product distribution plots in all figures from (a) to (c) in Figure 5-4 almost completely overlap for Ansys and COCO, except for some negligible deviations in the plots of Olefins. From the above results, it can be concluded that both the PFR and CFD models were in close agreement. This means that 2D CFD model can be used with confidence and the kinetic model and data were working correctly for the isothermal case. It can, thus, be used for further studies (Bar-Cohen and Rohsenow, 1984).

5.3 Non-Isothermal Case

Following sections describe the CO conversion, hotspot formation and the product distribution behaviour for non-isothermal case (described in section 5.1.2.1) with the help of temperature contours and plots. For the non-isothermal case, formation of hotspots was observed at all temperatures.

5.3.1 CO conversion

CO conversions at different temperatures for a tube of diameter 0.04m for the CFD model were given in Table 5-4 along with the isothermal CO conversions at corresponding temperatures. The CO conversions were seen to be slightly greater than the corresponding isothermal CO conversions at same steam temperature. This behaviour was observed due to slightly higher temperatures observed in the non-isothermal simulations which resulted in increased reaction rates. However, the difference between the CO conversions was small. This was because of the thin reactor tube exhibiting near isothermal operation in the reactor.

Table 5-4 CO conversions at different temperatures

CO conversion (%)			
Steam Temp. (°C)	Non-Isothermal Case	Isothermal	Net change
200°C	23.55	23.09	0.46
220°C	43.62	42.56	1.06
240°C	63.75	62.64	1.11

5.3.2 Temperature Contours

The temperature contours were obtained for various feed temperatures in Ansys and were presented in Figure 5-5, Figure 5-6 and Figure 5-7. The figures from (a) to (e) represent the successive sections of the catalyst bed in all three figures. The inert zones at both the ends of the catalyst bed were not included. Figures from (a) to (e) show a total reactor length of 12m. Thus, the Figure 5-5 (a) to Figure 5-5 (e) show the reactor length from 0.1m to 12.1m. Each figure from (a) to (e) show equal length of 2.4m.

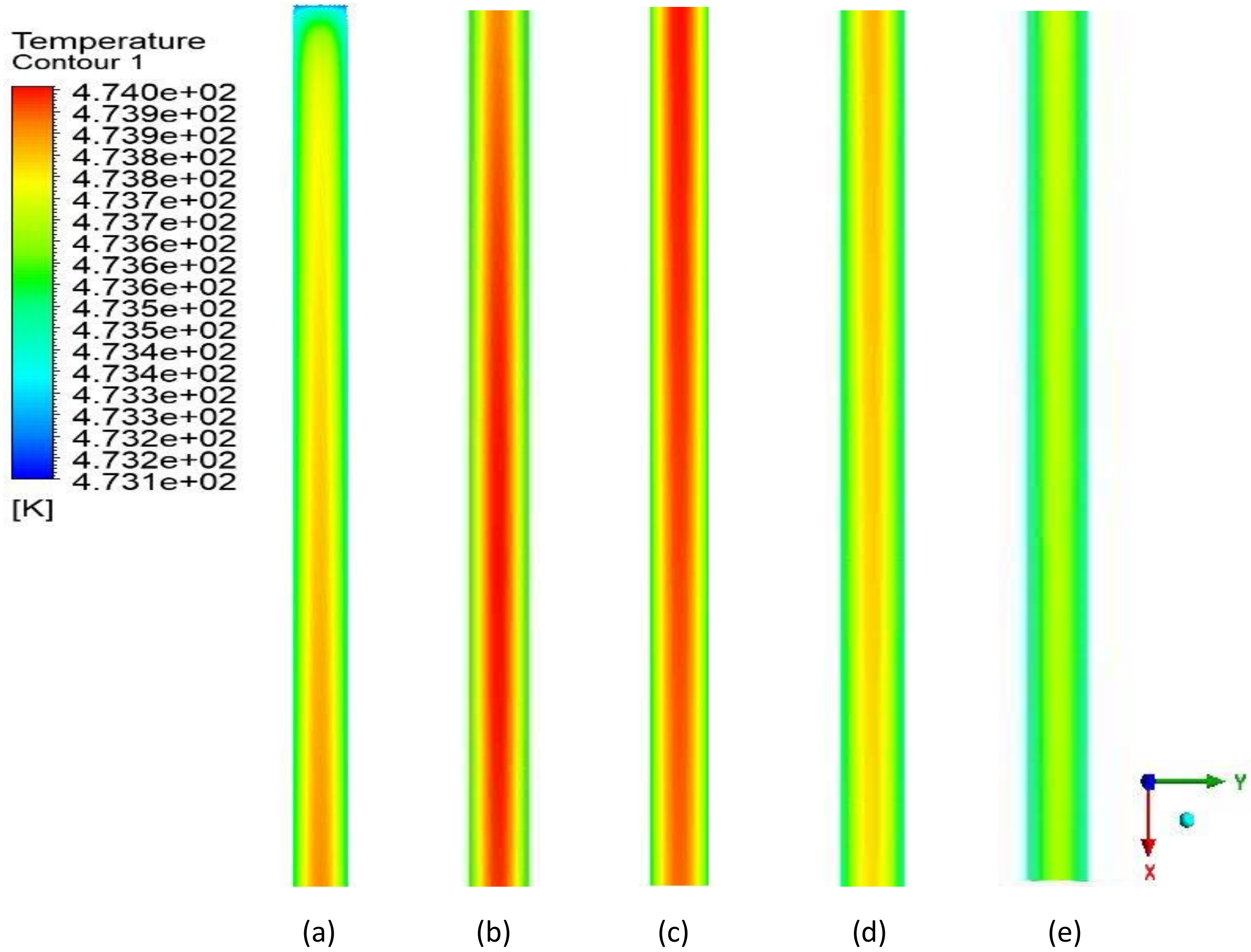

Figure 5-5 Sections of the catalyst bed showing the temperature contour successively in the order (a) to (e) for a steam temperature of 473.15 K (200°C) for a tubular reactor of diameter 0.04m

The steam temperature outside the reactor tube was 200°C. The wall temperature seems to be close to steam temperature throughout the reactor which indicates good heat removal from the tube. The temperature rise in the reactor (the highest temperature in the reactor – the inlet temperature) was 0.85 K which was small and hence, near isothermal behaviour was observed.

As a next step, contours were obtained for a case with steam temperature and inlet temperature of 220°C. The size of the hotspot here can be seen to be smaller compared to Figure 5-5, which means that the hotspot was less diffused than the contour in Figure 5-5.

The centre of the hotspot shows a shift towards the inlet and was comparatively closer to the inlet. The rise in temperature at the hotspot was comparatively larger than the previous case. This value was 1.75 K.

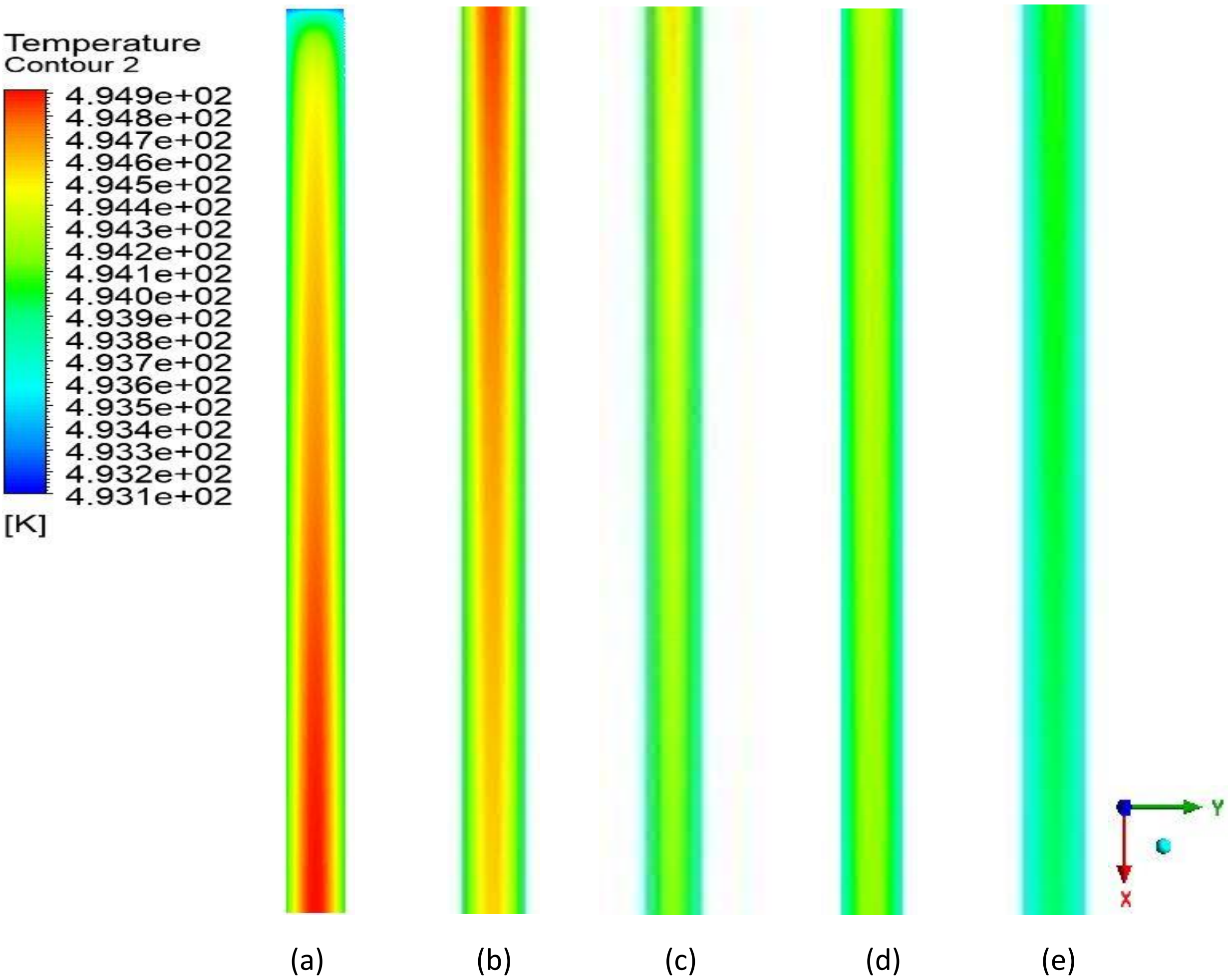

Figure 5-6 Sections of the catalyst bed showing the temperature contour successively in the order (a) to (e) for a steam temperature of 493.15 K (220°C) for a tubular reactor of diameter 0.04m

Lastly, simulation case with a steam and inlet temperature of 240°C was run and the results were shown in *Figure 5-7* (a) – (e). The hotspot size was the smallest in this case and was nearest to the inlet compared to the previous two cases. The difference in temperature between the hotspot temperature and the inlet temperature was comparatively highest in this case (3.75 K).

The hotspot temperature can be seen to be shifting towards the inlet with increasing steam temperature. The hotspot was more diffused in terms of its location and size for lower temperatures. As the temperature rises, the hotspot size gets smaller. Higher temperature leads to faster reactions and higher CO conversions, thus, the heat release was relatively faster and larger, while the driver for heat removal remains the same. Thus, the heat removal cannot keep up with the heat generation and there was a temperature rise with increasing reaction temperature. The larger temperature difference thus promotes faster heat removal, which, in this instance was high enough to bring the reaction temperature down, without the risk of temperature run-away. As the temperature rises, the hotspot has a quicker increase and decrease in temperature leading to a higher and narrower hot spot.

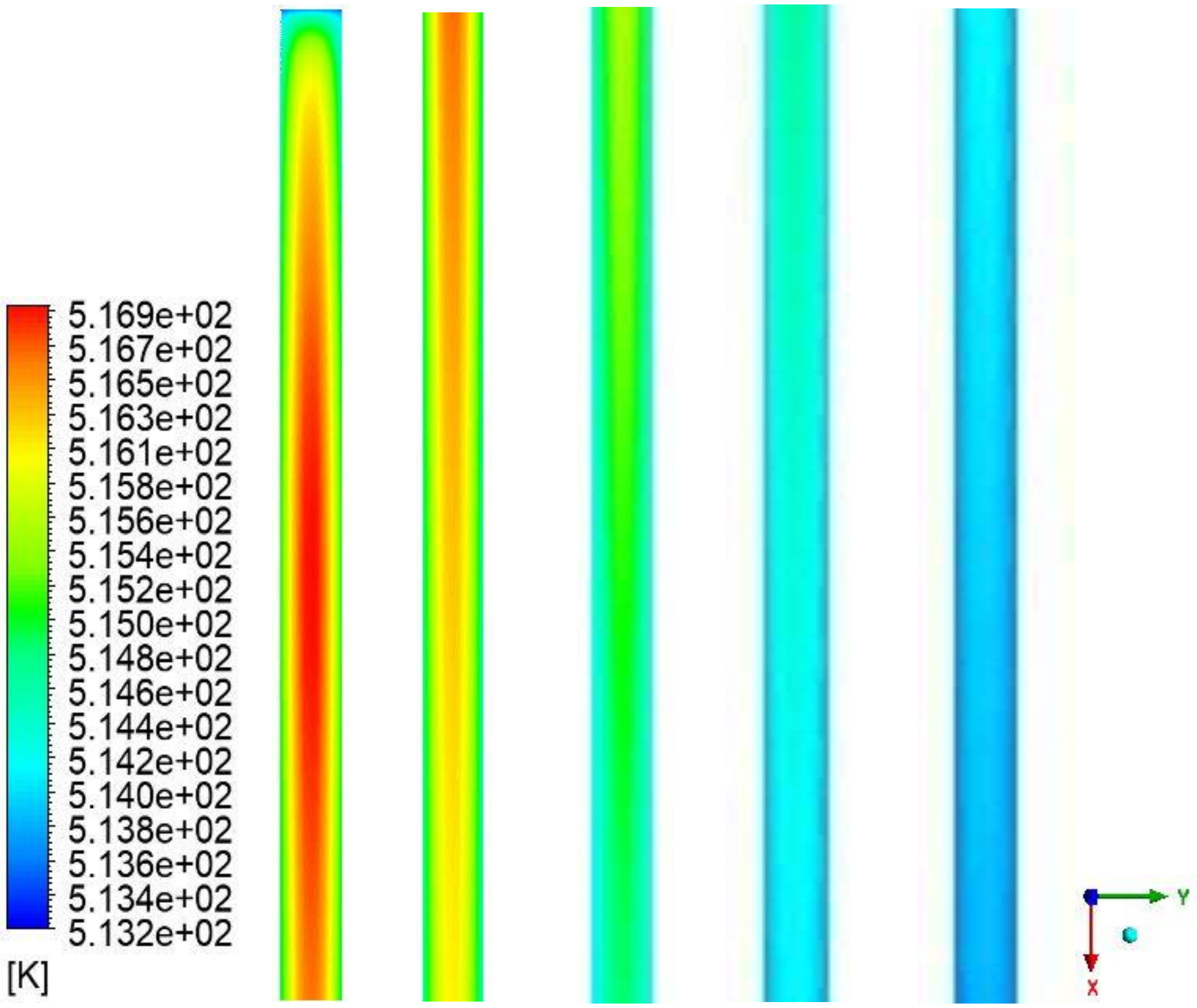

(a) (b) (c) (d) (e)

Figure 5-7 Sections of the catalyst bed showing the temperature contour successively in the order (a) to (e) for a steam temperature of 513.15 K (240°C) for a tubular reactor of diameter 0.04m

5.3.3 Product distribution

Product distribution for the non-Isothermal case was given in *Figure 5-8* for paraffins and olefins. As mentioned above, the non-isothermal case have a slightly higher temperature and increased CO conversion in the reactor. For the non-isothermal cases, product distribution was similar to that of the isothermal case shown in Figure 5-2. A comparison between isothermal and non-isothermal conditions has been shown in Figure 5-9 for paraffins and olefins respectively. Even though increased CO conversion was observed for non-isothermal cases, there was very little difference observed in the product distributions as it almost overlaps with the product distribution observed for isothermal case.

The results presented in this section were for a very thin tube which has a good heat transfer. As the tube diameter was increased the heat transfer reduces and the differences between the isothermal and the non-isothermal conditions increase. This was explained in section 5.3.4.3.

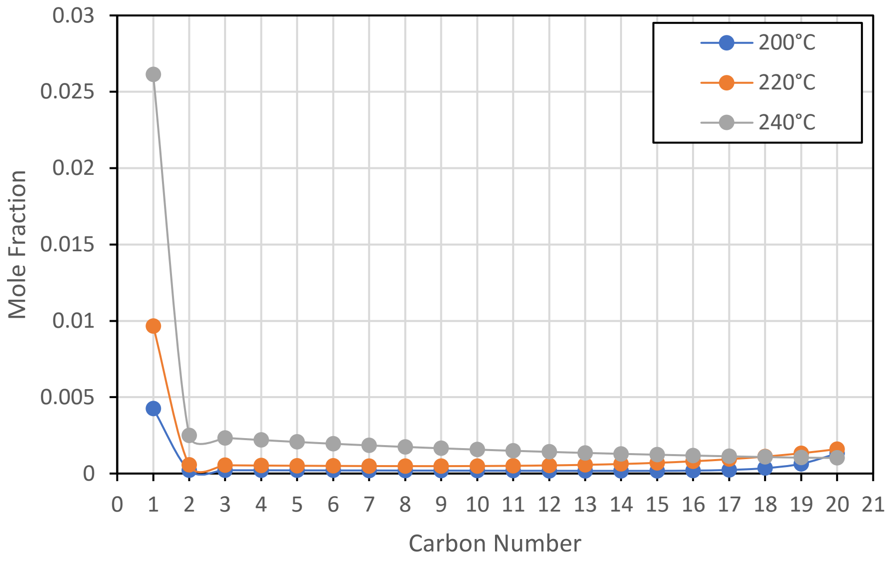

(a)

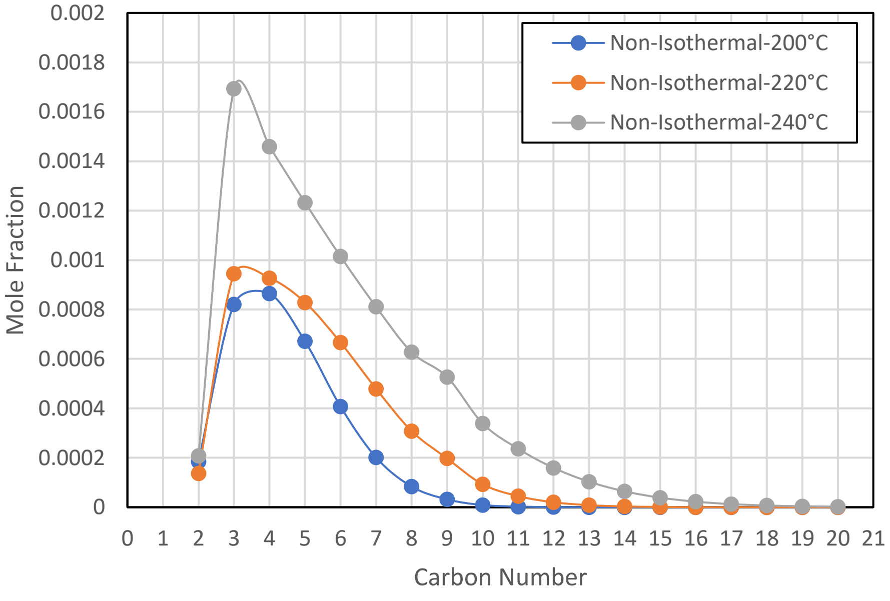

(b)

(b)

Figure 5-8 Mole fraction for (a) Paraffins (b) Olefins at different temperatures for non-isothermal conditions

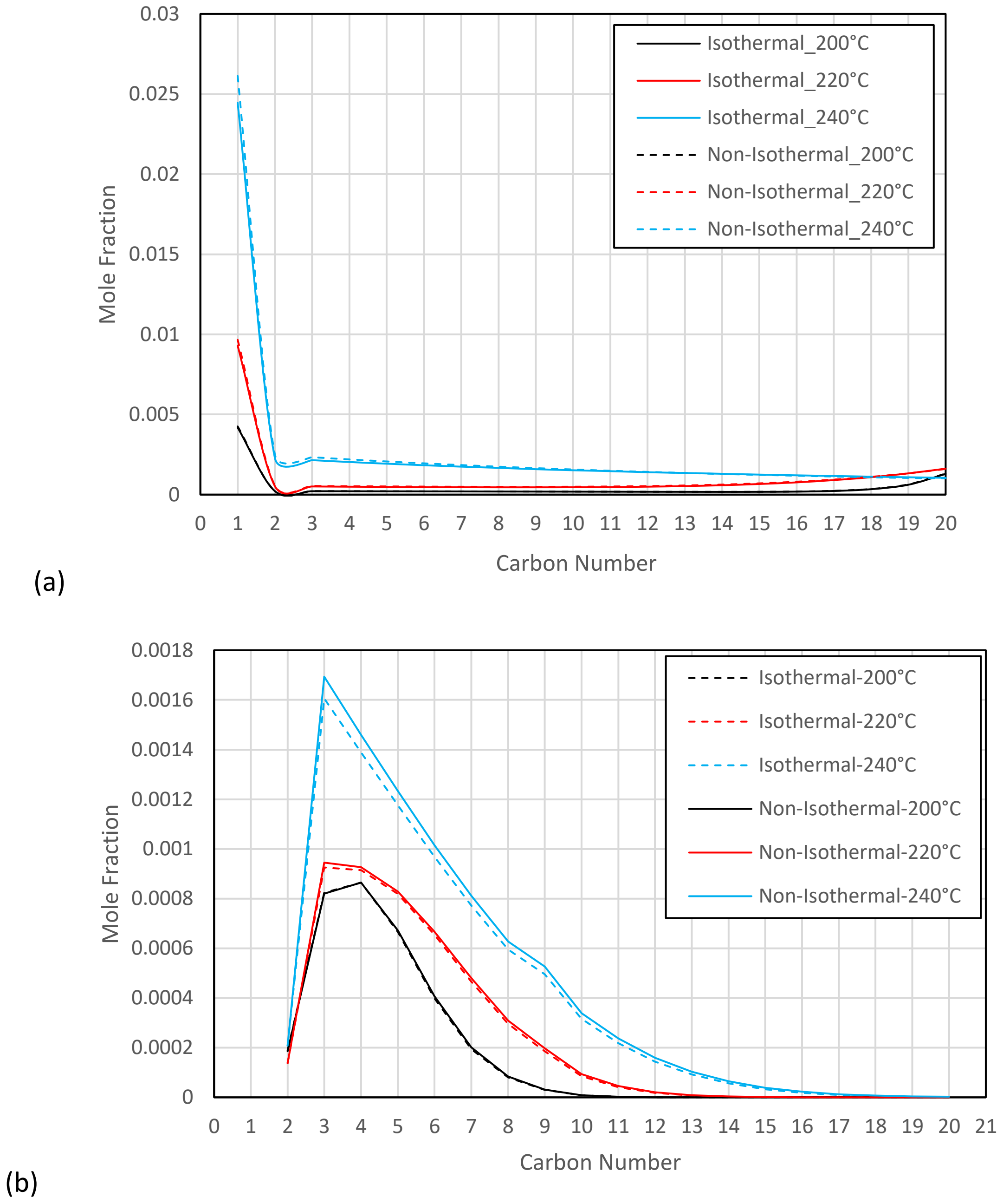

(b)

Figure 5-9 Comparison of product distributions for the isothermal and the non-isothermal cases for (a) paraffins (b) olefins

5.3.4 Comparison between 1-D and 2-D for non-isothermal case

5.3.4.1 CO conversion

After having compared the 2D isothermal results with the 1D isothermal results in COCO, the 2D non-isothermal case was also compared with a 1D non-isothermal case in COCO for a tube of diameter 0.04m. Overall heat transfer coefficient ($U_{overall}$) at different steam temperatures were calculated from Ansys and used in the 1D PFR (COCO) model to simulate heat transfer. The method used to calculate $U_{overall}$ from the CFD model was shown in Appendix G. The CO conversions and the hotspot temperatures obtained from Ansys and COCO were tabulated in Table 5-5.

Table 5-5 CO conversions and hotspot temperatures at different steam temperatures

	Ansys			COCO	
Steam Temp.	CO conversion (%)	Maximum Temp (°C)	$U_{overall}$ (w/m2.k)	CO conversion (%)	Maximum Temp (°C)
200°C	23.55	200.81	6804.26	22.35	200.60
220°C	43.62	221.80	6936.08	42.32	221.32
240°C	63.75	243.77	7336.27	63.29	242.63

The hotspot temperature in the 2D Ansys results were taken as the maximum temperatures observed in the geometry. For all cases the hotspot temperatures lie on a line through the centre of the reactor (central axis for the tube reactor) as shown in *Figure 5-10*, due to symmetry in geometry. For COCO, the hotspot temperatures were taken to be the maximum temperatures along the reactor length.

However, the calculation of the heat transfer coefficient, $U_{overall}$, was done on the basis of the basis of volume averaged temperature and not the hotspot temperatures.

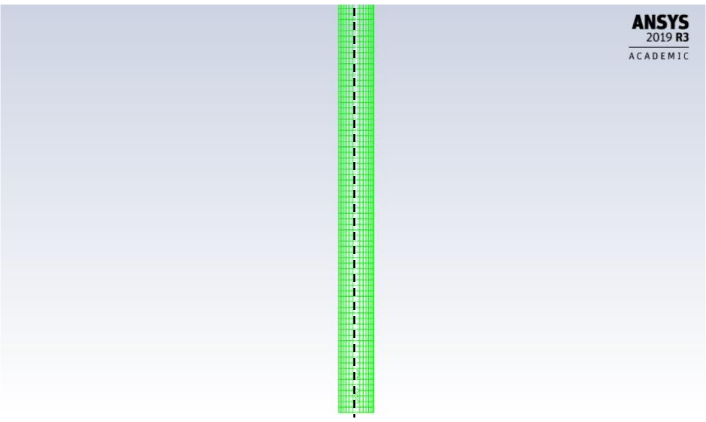

Figure 5-10 Line of interest for the hotspot temperatures for the planar geometry

CO conversions at different reactor feed and steam temperatures were shown in Figure 5-11. A comparison of temperature rise was shown in Figure 5-12. Temperature rise has been defined in equation (5-3) for Figure 5-12 and Figure 5-13.

$$\triangle T = T_{Hotspot} - T_{Feed} \qquad (5\text{-}3)$$

In Ansys the temperature varies in the radial direction along with the axial direction. The $U_{overall}$ values employed in COCO, were calculated using volume averaged temperatures in Ansys and thus it was expected that the temperature calculated by COCO would yield temperature deviations closer to the radial average, which was supposed to be lower than the centre line temperature reported by Ansys. This was explored in the following sections.

Even though there was a difference in the rise in hotspot temperatures, the differences were small and can be attributed to the little difference in CO conversions as the CO conversions in COCO were a little lower than Ansys. Hence, it can be concluded that the data generated by Ansys was reliable and can be used with confidence.

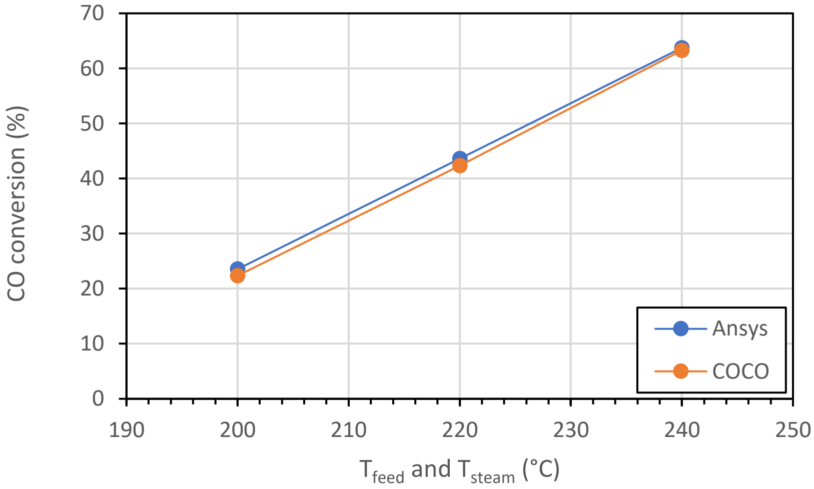

Figure 5-11 CO conversions at different steam temperatures for Ansys and COCO

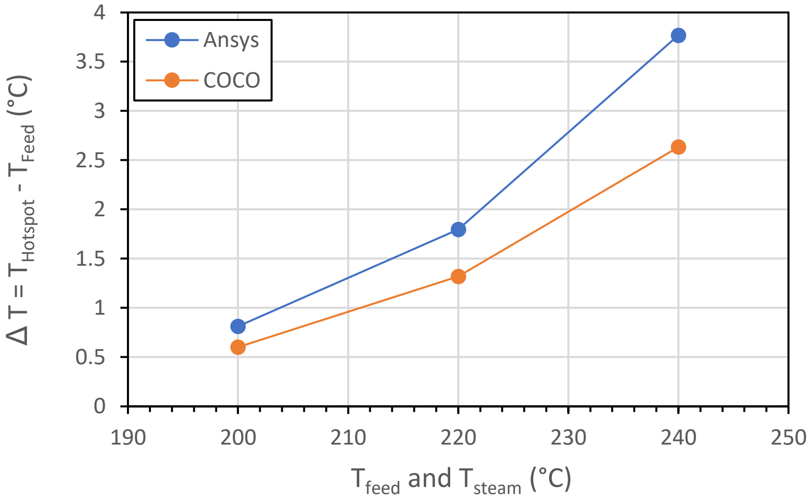

Figure 5-12 Comparison of the temperature rise between for Ansys and COCO at different steam temperatures

5.3.4.2 Temperature Profiles

Figure 5-13 compares the temperature rise relative to the feed temperature as shown in equation (5-4), across the length of the reactor between COCO and Ansys.

$$\triangle T = T_{Reactor} - T_{Feed} \tag{5-4}$$

For Ansys, the temperature rise profiles were plotted along the centreline i.e. the reactor axis (shown by the dotted black line in *Figure 5-10*) as well as along the reactor wall. The profiles were shown only for the catalyst zone and the top and bottom portions of the reactor were not included. 0 on the x-axis denotes the beginning of the catalyst zone and the ending of the zone was represented by 12m mark.

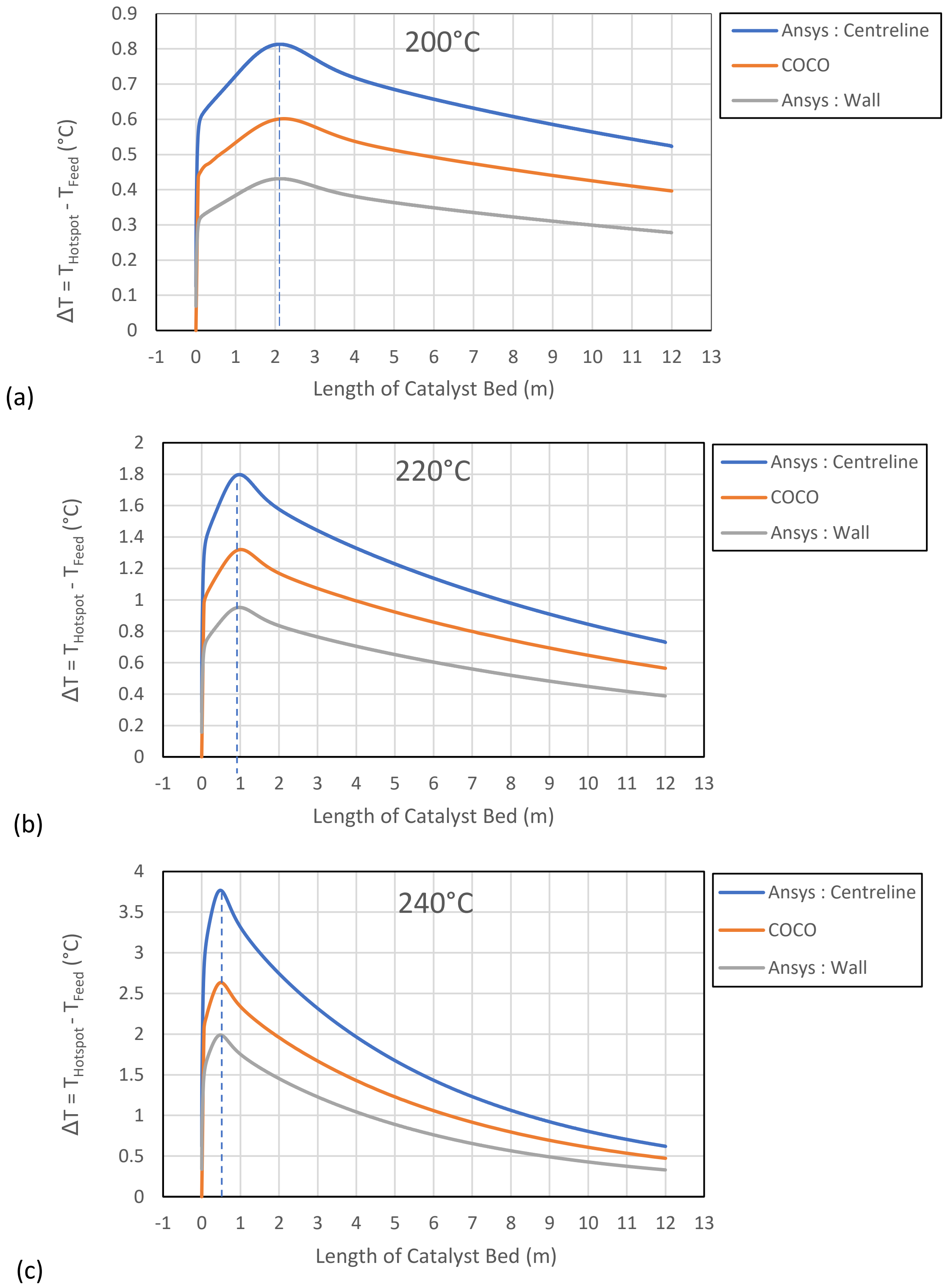

Figure 5-13 Temperature rise profiles at the axis and the wall of a reactor at different steam temperatures (a) 200°C (b) 220°C (c) 240°C

There was a sharp increase in temperature at 0m which was the beginning of the catalyst bed for all three temperatures 200°C, 220°C and 240°C in Ansys as well as COCO. It was the point where the reactions start. The sharp rise in temperature was a result of the heat produced from the reactions. Figure 5-14 shows plots of the heat of the reaction and rise in temperature at the very beginning (0m – 0.03m) of the catalyst zone for a steam temperature of 220°C for the same tubular reactor employed in Figure 5-13. A sharp rise in the heat of reaction can be observed from 0m to 0.005m, which results in a sharp rise in temperature, shown in Figure 5-14 (b), for the same region 0m to 0.005m. This explains the sharp increase in temperature rise profiles of Figure 5-13 at 0m. The temperature rise is not zero at the beginning (0m) on the x-axis in Figure 5-14 (b). This shows that there is some temperature thermal dispersion and/or conduction into the inert zone.

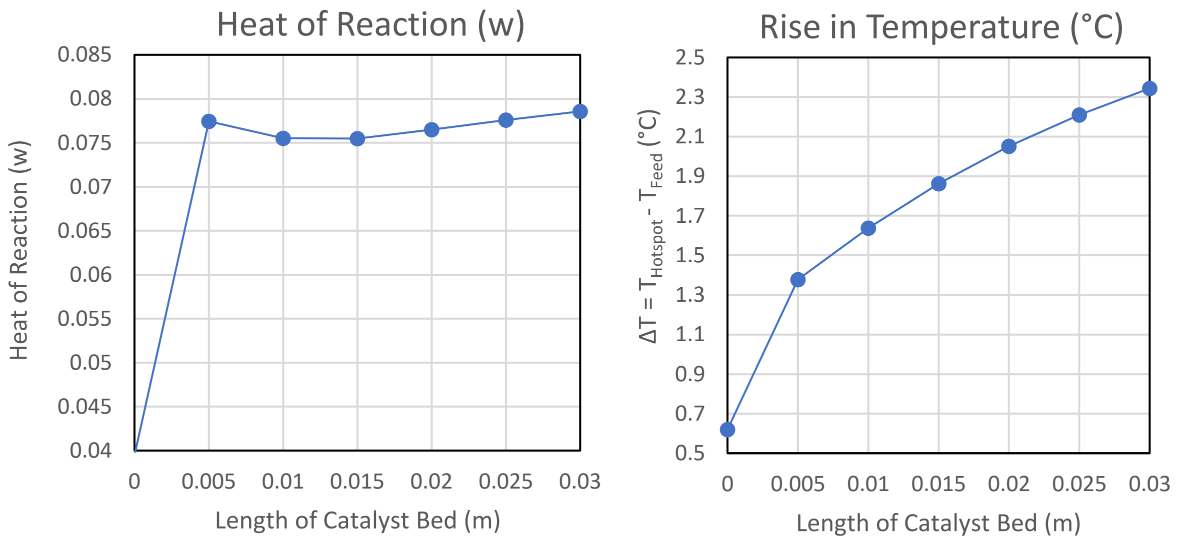

(a) (b)

Figure 5-14 (a) Heat of Reaction (b) Rise in temperature, at the reactor centreline at the beginning of the catalyst bed for the tubular reactor of diameter 0.04m

Ansys takes into account the radial transfer of heat along with the axial heat transfer and therefore it shows different temperature profiles along the axis and the wall. However, radial variations were not taken into account in COCO as it reports a single temperature profile providing a 1D representation of the reactor temperature.

Figure 5-13 shows that the COCO profiles always lie roughly midway between the two extremes of the Ansys temperature profile, i.e., the centreline temperature profile and the wall temperature profile. As discussed previously in section 5.3.4.1, considering that the calculation of $U_{overall}$ uses volume average temperature values, thus yielding a temperature averaged $U_{overall}$. This leads to a COCO profile that lies between these two extremes.

Figure 5-15 shows temperature profile along the radius of the tubular reactor at an axial position located at the maximum temperature rise for a steam temperature of 220°C. The temperature reported by COCO at the same location was also plotted to present a comparison between the 1D and 2D models. The temperature values along the radius in Ansys were used to find volume averaged temperature using Scilab to compare with the temperature reported by COCO. The value obtained using this calculation was 221.3°C. The value reported by COCO was close to 221.3°C as can be seen from *Figure 5-15*. This proves that COCO represents a volume averaged profile of temperature represented by Ansys.

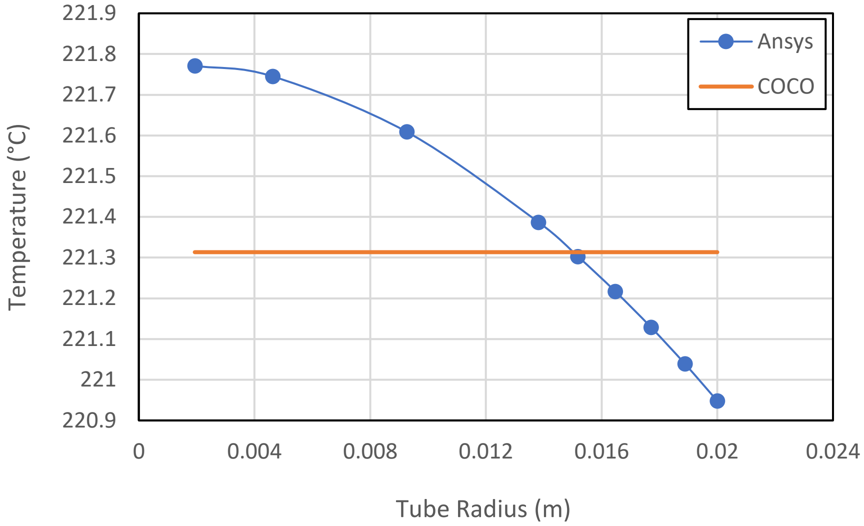

Figure 5-15 Radial temperature profile obtained at the hotspot location from Ansys at 220°C

The hotspot temperatures reported by COCO differ from the ones reported by Ansys. This happens because there were a few limitations with using the $U_{overall}$ in COCO. Some of them were listed here:

1. $U_{overall\ was}$ estimated as an average value over the whole domain.
2. In Ansys, the heat transfer coefficient value used for simulating was calculated as a function of the axial and the radial position, while in COCO, uniform value was used for the entire reactor domain. There was no provision for a position dependent $U_{overall}$ to be used in COCO.
3. The error between the temperature profiles will increase as the peak maximum temperature rises because the volume average estimation of $U_{overall}$ gets poorer as ΔT increases.

Due to these reasons, the hotspot temperatures predicted by COCO differ from the ones reported by Ansys. The hotspot temperatures in COCO were lower than that of Ansys by a few degrees at all steam temperatures 200°C, 220°C and 240°C.

If the 1D and 2D models were to be compared for the same tube diameter at which the thermal runaway would occur according to the 2D model, relatively lower hotspot temperatures in 1D model indicate that the 1D model can go up to larger diameters than the one reported by the 2D model, without having a thermal runaway. This result was in agreement with the work of Jess and Kern, 2009. This means that a 1D model overestimates the thermal runaway diameter. Therefore, a 2D model gives a better representation of the heat transfer compared to the 1D model and should be preferred over the 1D model (Jess and Kern, 2009).

For a better representation of the hotspot temperatures in COCO, the $U_{overall}$ values can be tuned to allow COCO to predict temperature runaway more closely to the 2D hotspot temperatures. However, this would lead to alteration of CO conversion and entire reactor's temperatures at all positions, along with other parameters. This kind of tuning can be helpful if the 1D PFR (COCO) model was to be used only for obtaining the hotspot temperatures.

The following section shows a comparison between the product distributions obtained from Ansys and COCO for non-isothermal conditions to study if the negligence of the radial effects in COCO affects its product distribution.

5.3.4.3 Product distribution

Unlike the previous sections, a tube of radius 0.08m was used to obtain the product distributions in both the softwares Ansys as well as COCO for a steam temperature of 220°C in this section. This radius was chosen so that maximum deviations between 1D and 2D models could be obtained, as a bigger radius would lead to larger radial variations. Increasing the radius to 0.09m resulted in a thermal runaway as shown in the following section. Therefore, a tube of radius 0.08m served as an extreme case to show the maximum effect of neglecting the radial variations in a 1D model. Figure 5-16 show the product distributions for the paraffins and olefins respectively for 1D and 2D models for non-isothermal conditions. Product distribution for the isothermal conditions was also plotted to present a comparison. Figure 5-16 shows the paraffin distribution spectrum from C_2 – C_{20} whereas the olefin distribution ranged from C_2 – C_{20}. C_1 (Methane) was excluded from the spectrum as its concentration was much higher than other species and hence, plotting it on the same graph with other species made it difficult to show the difference between Ansys and COCO plots.

Table 5-6 Conversions for a tubular reactor of radius 0.08m for a steam temperature at different conditions

Conversion (%)			
Isothermal		Non-Isothermal	
Ansys	COCO	Ansys	COCO
42.56	41.40	57.15	50.36

From Figure 5-16 significant differences can be observed in the product distribution profiles between Ansys and COCO at non-isothermal conditions for both paraffins as well as olefins unlike the isothermal case. At isothermal conditions, Ansys and COCO seem to have similar product distribution. This similarity was also shown in Figure 5-4 for a narrow tube reactor. At non-isothermal conditions, a wider tube has larger radial variations of temperature compared to the narrow tube and hence negligence of the radial variations by the 1D model has shown larger differences for the wide tube in Figure 5-16.

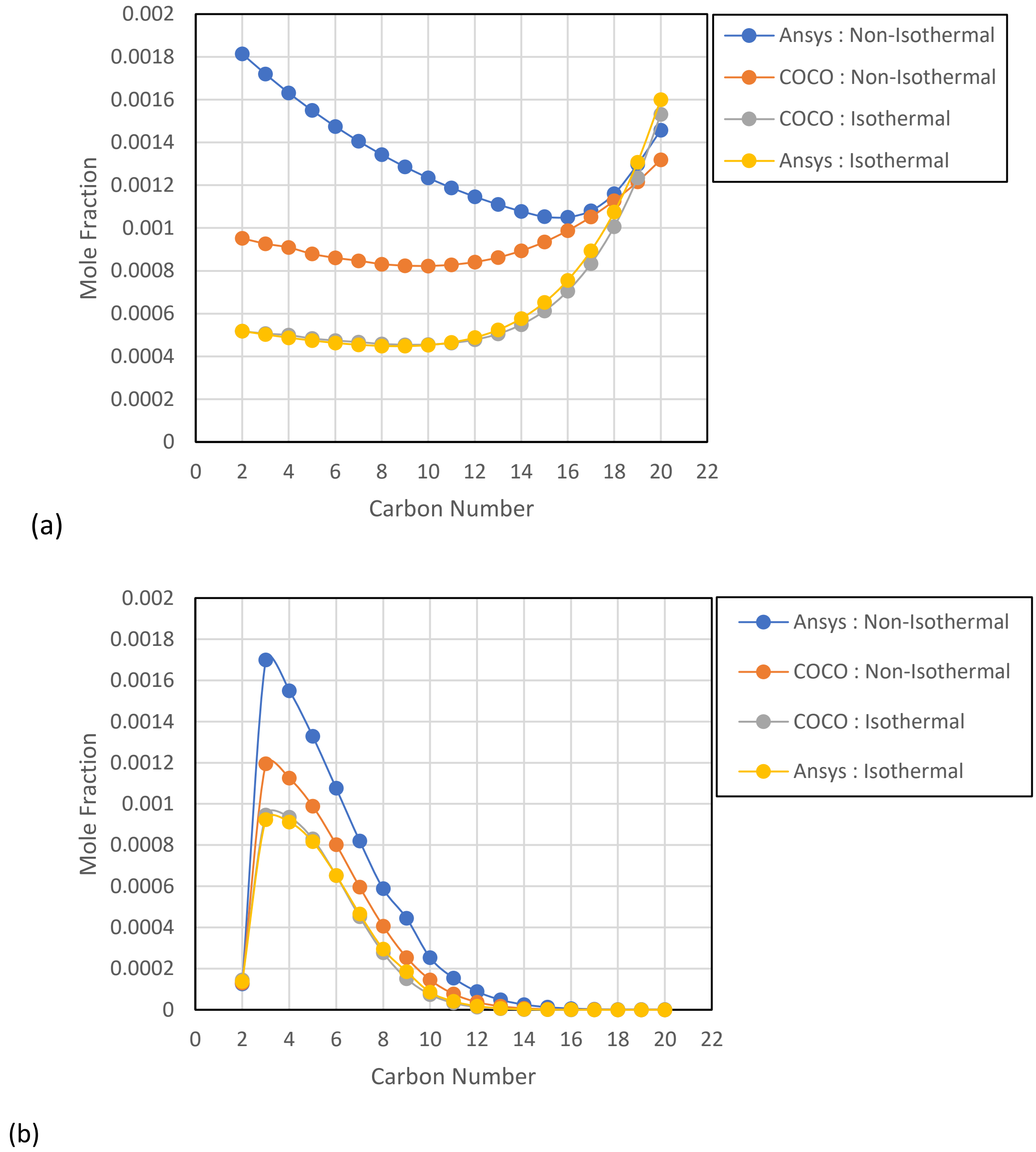

Figure 5-16 Mole Fraction of (a)Paraffins (b) Olefins at the outlet of a tube of radius 0.08m in Ansys and COCO at a steam temperature of 220°C for Isothermal and non-isothermal conditions

Unlike Figure 5-9, significant differences can be seen between the product distributions at isothermal and non-isothermal conditions. This was so because the current section employed a wide tube of radius 0.08m unlike section 5.3.3 which employed a tube of radius 0.02m. A wider tube has a poorer heat transfer behaviour compared to the narrow tube and hence differences between the isothermal and non-isothermal conditions was more evident in wide tubes.

However, the differences in the product distribution in plots of Ansys and COCO in Figure 5-16 cannot be attributed to the differences in CO conversion only, because there were differences in the shapes of the distributions especially for the paraffins at the non-isothermal conditions. Such differences were not observed for the isothermal plots. Difference in the shape of the distribution were also observed when a non-isothermal distribution was compared to an isothermal one. This highlights the importance of the radial variations of mass and heat transfer in the 2D model.

To further understand the difference between 1D and 2D model for a wide tube, temperature profiles were obtained at the centreline and wall in Ansys and COCO and were shown in Figure 5-17.

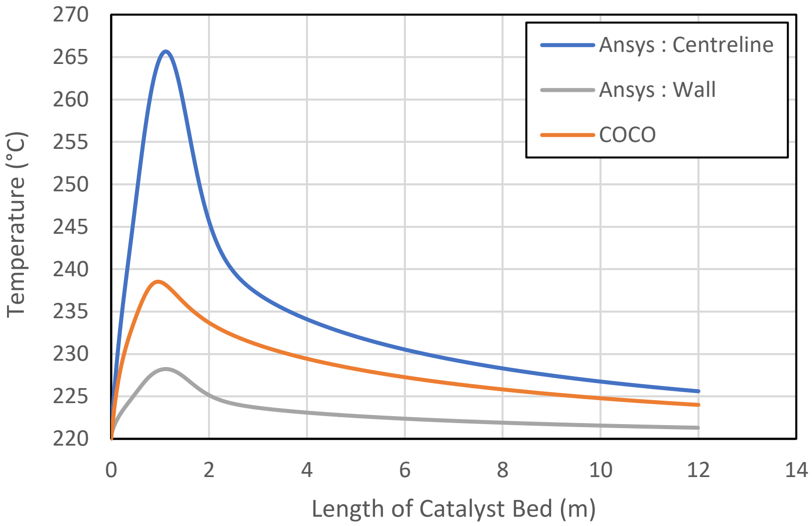

Figure 5-17 Temperature Profile for a tube of radius 0.08m using Ansys and COCO

The $U_{overall}$ used to model the heat transfer in COCO was calculated using Ansys. The calculation of $U_{overall}$ was explained in Appendix G. The difference in hotspot temperatures reported by Ansys and COCO have a huge difference of 28°C. The difference in the hotspot temperatures reinforces the argument that taking into account the radial variations of temperature in a reactor was important, especially for large diameter tubes. The 1D model underestimates the hotspot temperatures and thus overestimates the tube diameter at which thermal runaway occurs. Therefore, a 2D model should be preferred over the 1D model to study the heat transfer characteristics (Jess, 2012).

To explore the effect of conversion and temperature individually on the product distribution, plots of product distribution at different conversions at 220°C were obtained for isothermal and non-isothermal conditions and were given in Figure 5-18 and Figure 5-19 respectively. The profiles were obtained at various lengths of the reactor to get the concentrations at various conversions. Figure 5-18 and Figure 5-19 show that increasing conversion, increases the mole fraction of the species but the change in shape of the distribution was very small.

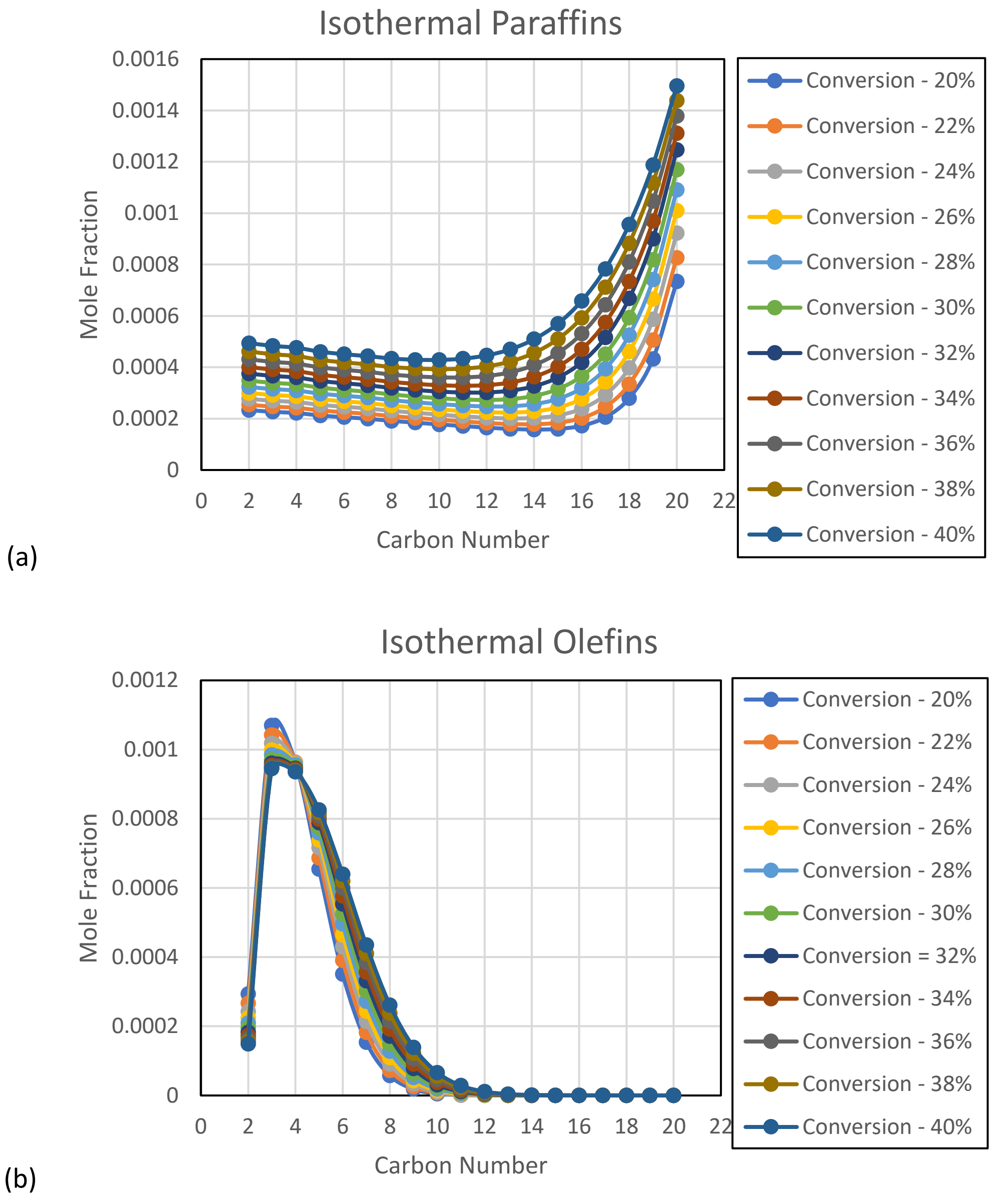

Figure 5-18 Product distribution for (a) Paraffins (b) Olefins at different conversions at isothermal conditions for tube reactor of radius 0.08m

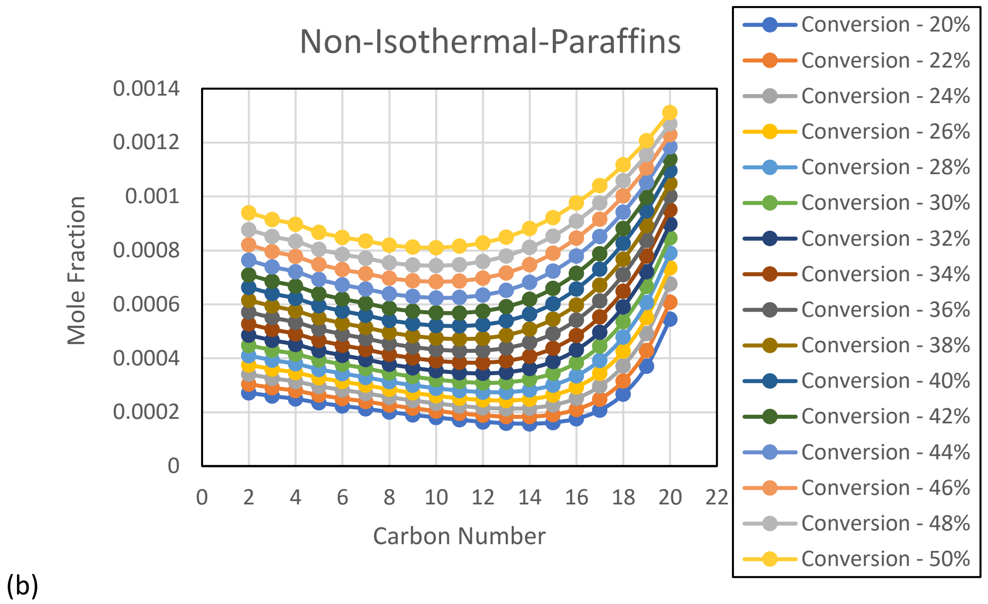

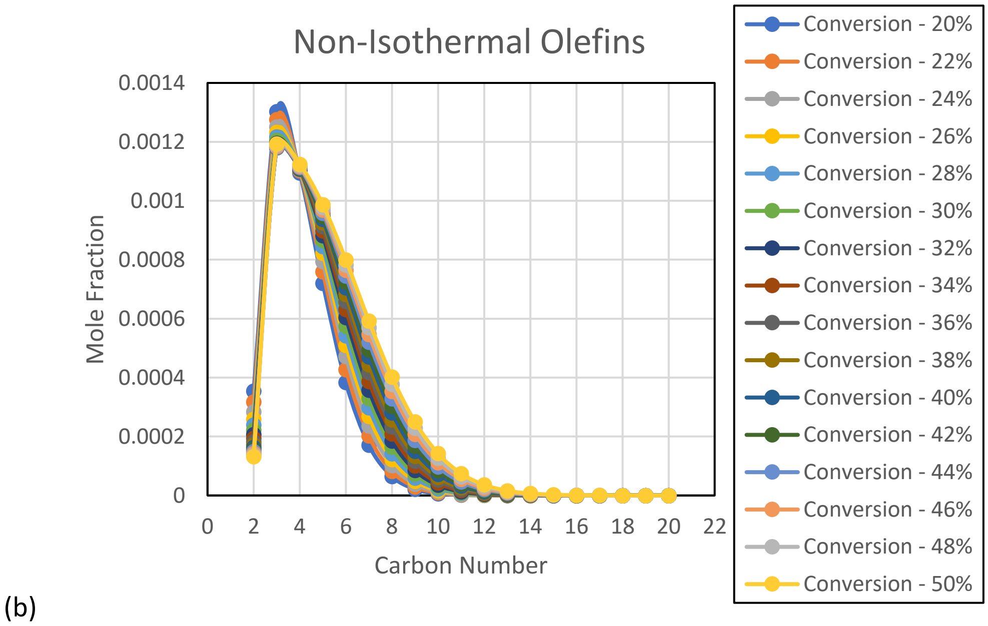

Figure 5-19 Product distribution for (a) Paraffins (b) Olefins at different conversions at non-isothermal conditions for tube reactor of radius 0.08m

Figure 5-20 shows product distribution at various temperatures for a conversion of 20% for isothermal conditions. Change in the shape of distribution at various temperatures was clearly evident from Figure 5-20. Increase in temperature promotes formation of shorter chains. Formation of higher chains decrease as the temperature goes up.

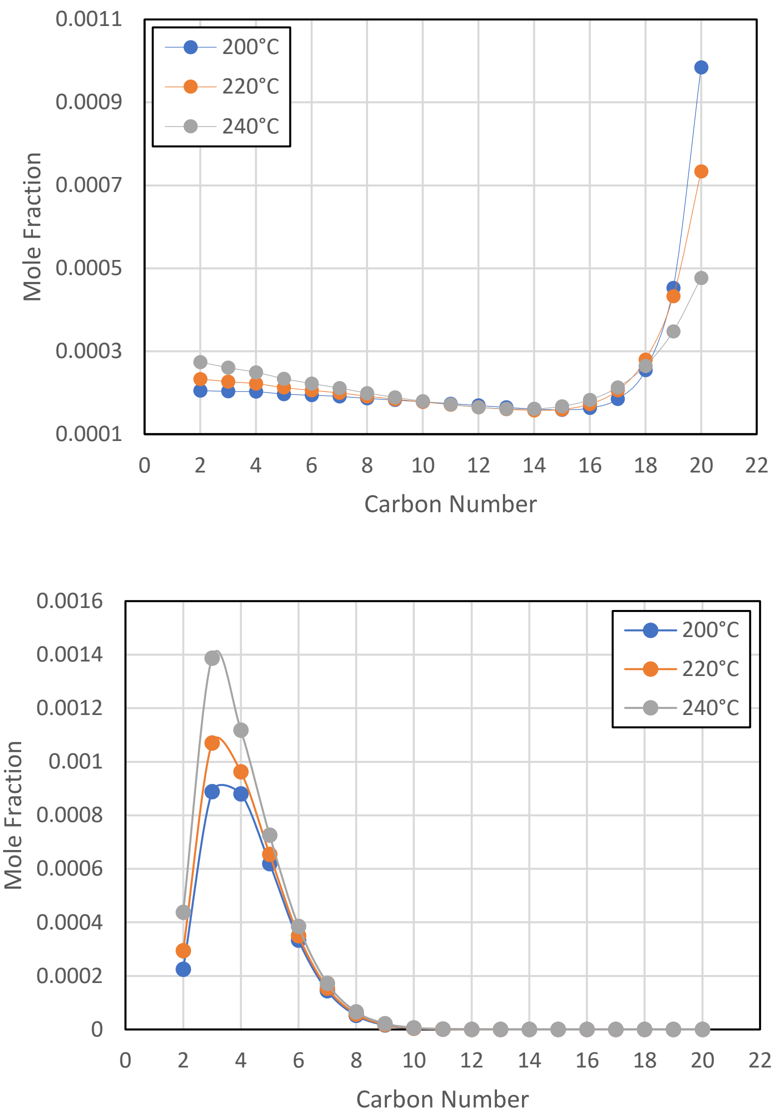

Figure 5-20 Product distribution for (a) Paraffins (b) Olefins at different temperatures at isothermal conditions for a conversion of 20% for a tube reactor of radius 0.08m

5.4 Tube Reactor vs Plate type Reactor

5.4.1 Comparison on the basis of Surface Area to Volume Ratio

As described in 4.7.1, a plate and a tube reactor were compared on the basis of physical similarity. The plate spacing for the plate reactor was kept equal to the tube radius of the tubular reactors for comparison.

The plate spacing values and corresponding radii were increased from 0.03m to 0.11m to carry out a parametric study taking the tube diameter and plate spacing as parameters. The upper limit was taken to be 0.11m as a thermal runaway was observed for the plate spacing of 0.11m.

A steam temperature and inlet temperature of 220°C was used and kept constant throughout all the simulations in the current section 0. All parameters except the tube diameter or the plate spacing were kept the same as simulations in previous sections. These parameters were kept equal for both the geometries. Hotspot temperatures and CO conversions were observed in both the cases and were explained in the following sections.

5.4.1.1 Hotspot Temperature & CO conversion

Figure 5-21 shows the CO conversions obtained for a tube and a plate for increasing plate spacing and the corresponding radius. Increase in conversion with increase in plate spacing/ radius occurs due to less heat removal from the reactor as discussed in the previous sections. The CO conversion in case of the tubular reactor was found to be higher than the corresponding plate type reactor at all plate spacings/radii. The difference was observed to be relatively small at smaller plate spacings/radii and increase at a rapid rate with increase of plate spacing or the radius.

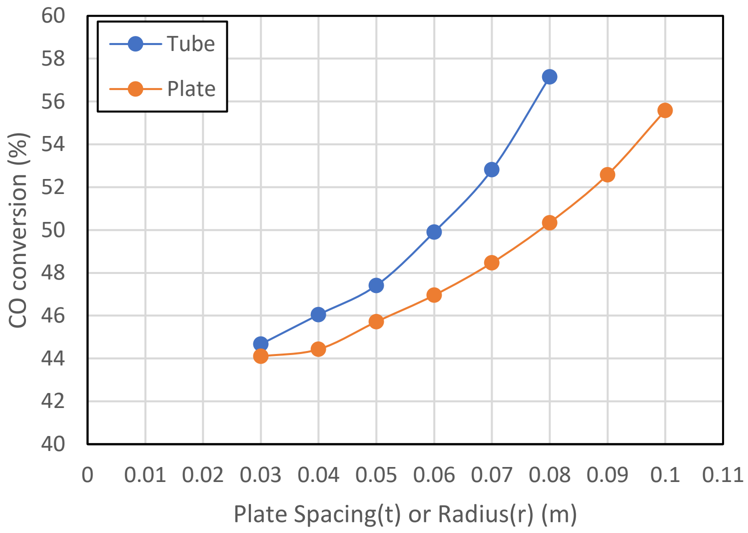

Figure 5-21 Plot of CO conversion at different plate spacing for plate type reactors and for corresponding radii for tubes

The results for the rise in temperature, Δ T, as given in equation (5-3) for both the cases were shown in *Figure 5-22*. From *Figure 5-22*, the hotspot temperature for the tubular reactor was found to be higher than the corresponding plate type reactor at all plate spacings/radii. The difference was observed to increase with increase of plate spacing or the radius. *Figure 5-23* shows the difference by which the tubular hotspot temperature was larger than the plate hotspot temperature for different plate spacing/radii. A temperature difference as large as 30°C was observed for a plate spacing/radius of 0.08m.

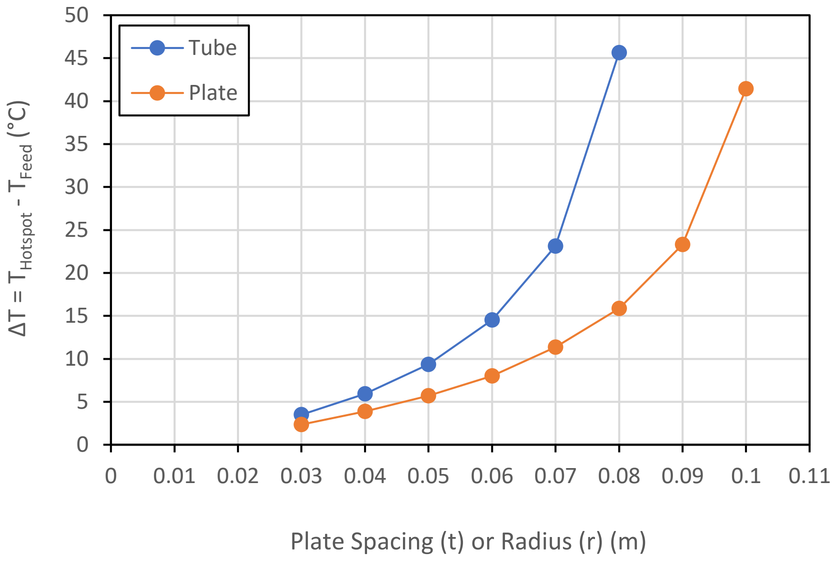

Figure 5-22 Comparison of Temperature rise at different plate spacing for plate type reactors and for corresponding radii for tubes

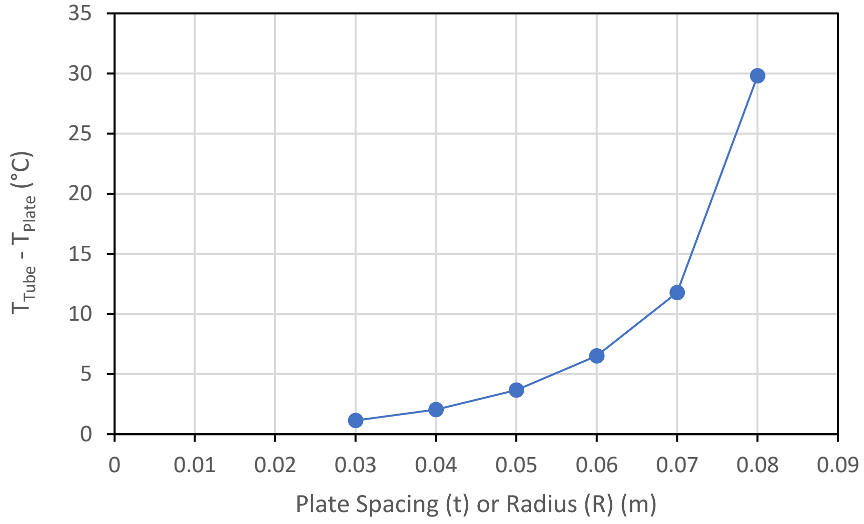

Figure 5-23 Difference in hotspot temperatures at different plate spacing for plate type reactors and corresponding radii for tubes

The rate of heat generation was proportional to the volume of the reactor while the heat removal was proportional to the surface area available for dissipation. The ratio of surface area to volume for a tube and a plate were given by 1/r and 1/t respectively. As plate spacing t was kept equal to tube radius r, this ratio was equal for both the geometries. This calculation was shown in Appendix H. As the tube and plate reactor get wider, this ratio decreases for both the geometries which results in poor heat removal from the reactors.

Figure 5-22 indicates that a thermal runaway occurred at smaller radius for the tube reactor than corresponding plate type reactor. This behaviour indicates a better heat dissipation in case of plate type reactors compared to the tubular reactors, which leads to a better temperature control. This observation leads to the acceptance of the hypothesis, of a plate type reactor being better than a shell and tube reactor in terms of better heat removal, which was derived from the works of Ambarita *et al.*, 2009, Tumuluri, 2018, Bright Hub Engineering, 2010, HFMPHE, 2018, Marine Engineering Study Materials, 2014 and Paul Mueller Company Engineering Staff, 2016.

A thermal runaway occurred for a radius of 0.09m for a tube while the plate type reactor could go up a spacing of 0.1m without facing a thermal runaway. A rough estimate for the radius or plate spacing that results in a thermal runaway was determined by plotting 1/ ΔT versus tube radius or plate spacing and extrapolating the curve to intersect x-axis. The extrapolation was carried out with the help of TREND function using a spreadsheet software Microsoft Excel. The TREND function computes the liner trendline based on given linear set of data using least square method. Two data points closest to the x-axis were used for extrapolation.

The extrapolation resulted in 0.09m to be the tube radius and 0.0113m. However, 0.09m as tube radius and 0.11m as plate spacing resulted in thermal runaway. Since linear interpolation does not precisely predict the correct trendline, these values only give a rough estimate of the actual tube radius and plate spacing.

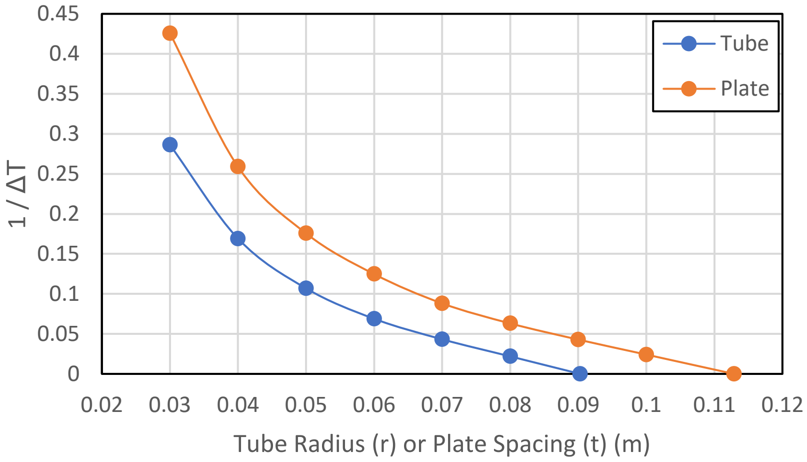

Figure 5-24 Plot of 1/ΔT extrapolated to find runaway tube radius and plate spacing

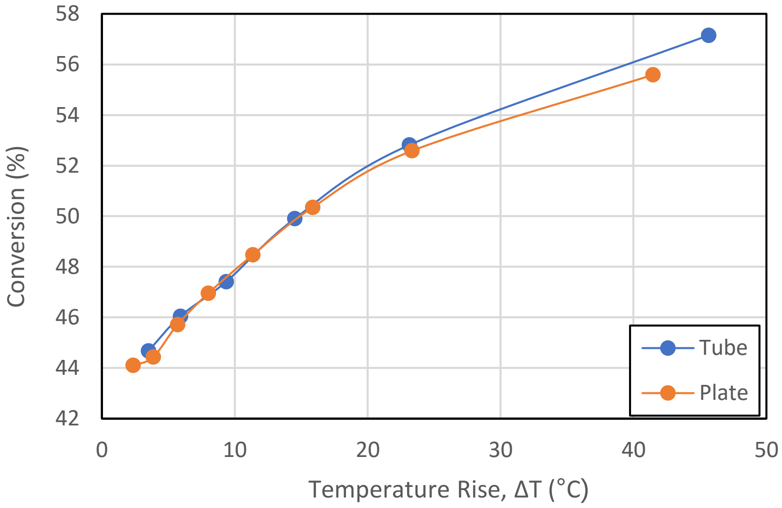

Figure 5-25 Conversion at different temperatures for tube and plate reactor

Figure 5-25 shows a plot of conversion versus temperature rise for both the reactors. As discussed previously, conversion increases with increase in temperature rise. The plots for both the geometries can be seen to be overlapping upto a temperature rise of around 20°C. This means that both the reactors provide similar conversion for a given temperature rise, provided the temperature rise was less than 20°C. However, a particle temperature rise does not occur to both the reactors at same value of plate spacing and radius. For a particle temperature rise, the plate reactor has a plate spacing less than the radius of corresponding tube reactor as can be seen from *Figure 5-22*. This means that for same temperature rise behaviour and conversion, a plate type reactor was more compact than a tube reactor.

After having confirmed of the differences in the results for a tube and a plate type reactor, it was important to understand the factors responsible for these differences. The two major differences in a tube reactor and a plate reactor were of the flow patterns and the heat transfer characteristics. To find out which factor was the major driving force behind the observed differences, the product distributions were obtained at isothermal conditions and non-isothermal conditions. At isothermal conditions, heat transfer characteristics cannot affect the reaction system and hence effect of flow patterns can be observed.

5.4.1.2 Product Distribution

5.4.1.2.1 Isothermal Case

Figure 5-26 gives the product distribution for paraffins and olefins at 220°C for a tube of radius 0.04m and a plate reactor of plate spacing 0.04m at isothermal conditions.

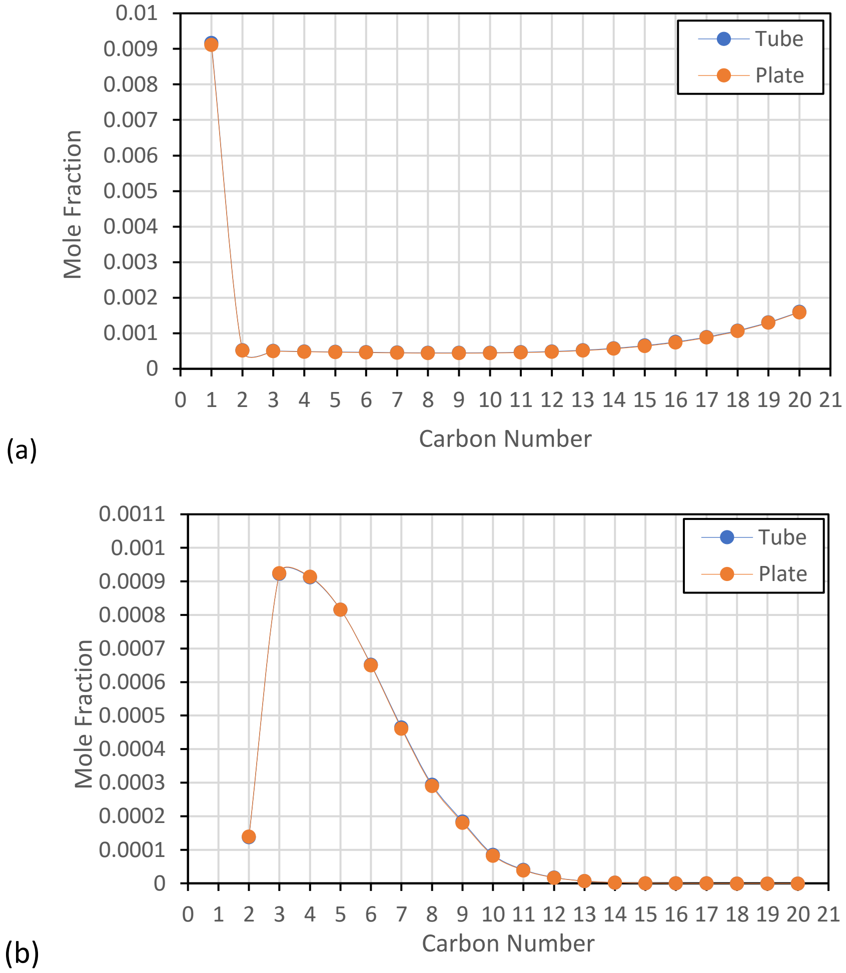

Figure 5-26 Product Distribution for (a) Paraffins (b) Olefins for a plate and tube reactor for isothermal conditions for a tube radius and plate spacing of 0.04m

At isothermal conditions, it was only the effect of flow patterns that could bring a difference in the product distributions as heat transfer characteristics were same for the geometries. As can be observed from Figure 5-26, the product distributions for the tube and plate geometries almost completely overlap with each other. The model indicates that the major driving force behind the differences in the performance of a tube and plate geometry was the heat transfer characteristics.

However, it should be noted that flow pattern depends on factors like catalyst packing and interaction between different phases along with reactor geometry. Catalyst packing structure has not been included in the model and, therefore, catalyst surface interactions are not taken into account. The latter will have effects on the flow pattern which will affect the mass transfer and hence, product distribution is expected to be different for the two geometries in the real reactor system. Therefore it is not possible to reach any conclusion on the effect of the flow pattern on the product distribution based on this model alone for isothermal conditions.

Non-Isothermal cases for tube and plate reactor were simulated and temperature profiles, contours and product distributions were presented in the following sections.

5.4.1.2.2 Non-Isothermal Case

A parametric study was carried out to analyse heat transfer behaviour along the reactor geometries with tube radius and plate spacing as the parameters for tube and plate type reactors respectively.

Figure 5-27 shows the temperature contours and the formation of a hotspot in a tubular reactor as the radius increases from 0.03m to 0.08m. These pictures do not show the full length of the reactor. They only show the top portion where significant temperature rise was seen. The length of the section of the reactor from (a) to (f) remains the same.

Increasing tube radius to 0.09m leads to a temperature runaway. In Figure 5-27 (a), (b) and (c), very small temperature rise (<10°C) was observed. This indicates a very good heat dissipation of the reaction heat generated and hence excellent temperature control resulting in almost isothermal operation in the thin tubes. However, significant temperature rise (upto 45°C) and formation of a hotspot can be seen in tubes with larger diameters.

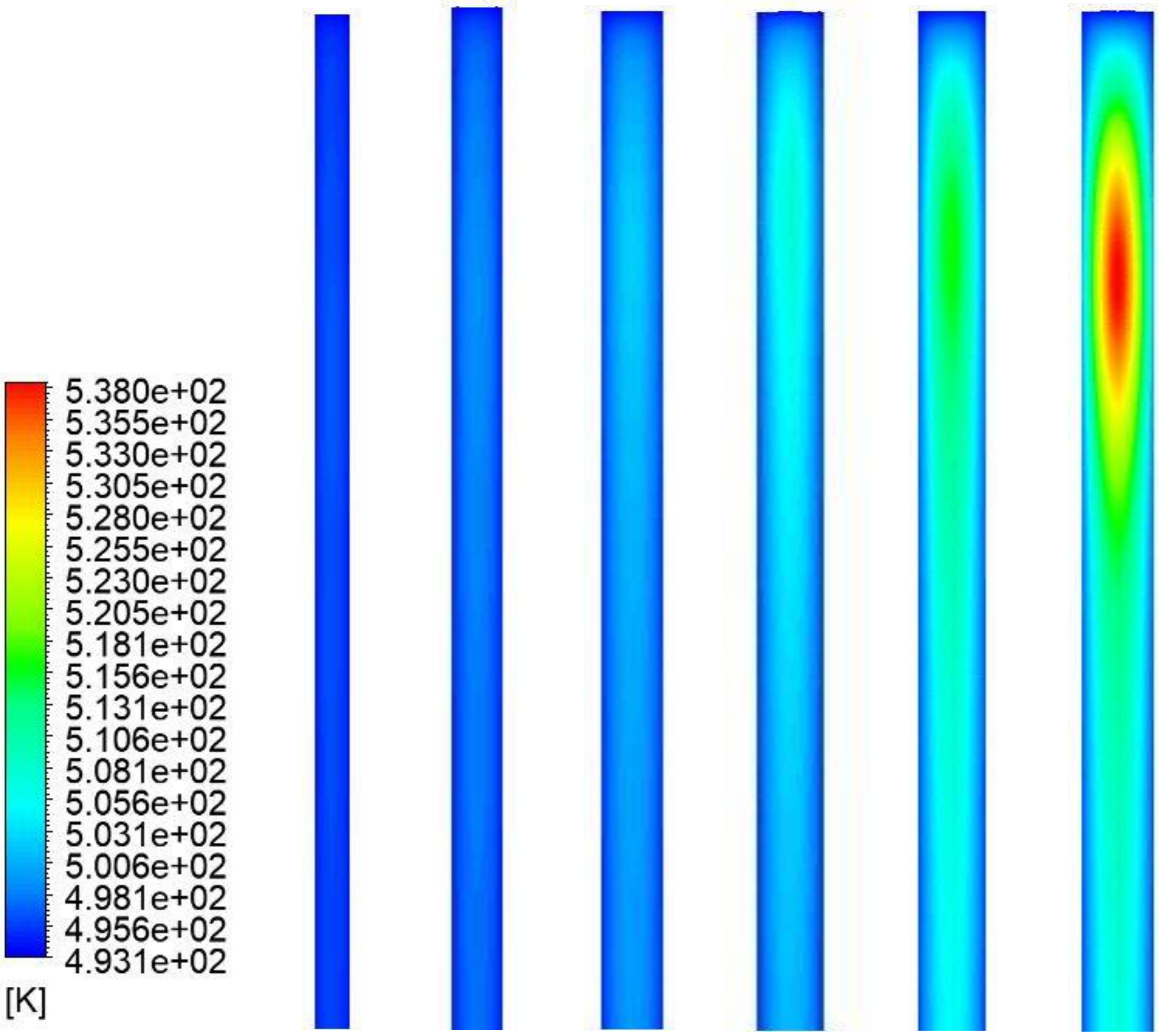

(a) (b) (c) (d) (e) (f)

Figure 5-27 Temperature contours of tubular reactors of different radii (a) 0.03m (b) 0.04m (c) 0.05m (d) 0.06m (e) 0.07m (f) 0.08m. These figures were not to geometric scale. Their purpose was to give a thermal comparison between (a) to (f)

Figure 5-28 shows the formation of a hotspot in a plate type reactor as the plate spacing increases from 0.03m to 0.1m. Like the previous figure for tubular reactors, this figure also does not show the full length of the reactor. They only show the top portion where significant temperature rise was seen. Figure 5-28 employs a different legend than Figure 5-27. The legends were given on the left side of the contours for both figures.

Increasing plate spacing to 0.11m leads to a temperature runaway. In Figure 5-28 (a), (b), (c) and (d), very small temperature rise (<9°C) was observed. This indicates a very good heat dissipation and hence excellent temperature control resulting in almost isothermal operation in the plate type reactors with small plate spacings. However, significant temperature rise (upto 40°C), and formation of a hotspot can be seen in plates with larger spacings.

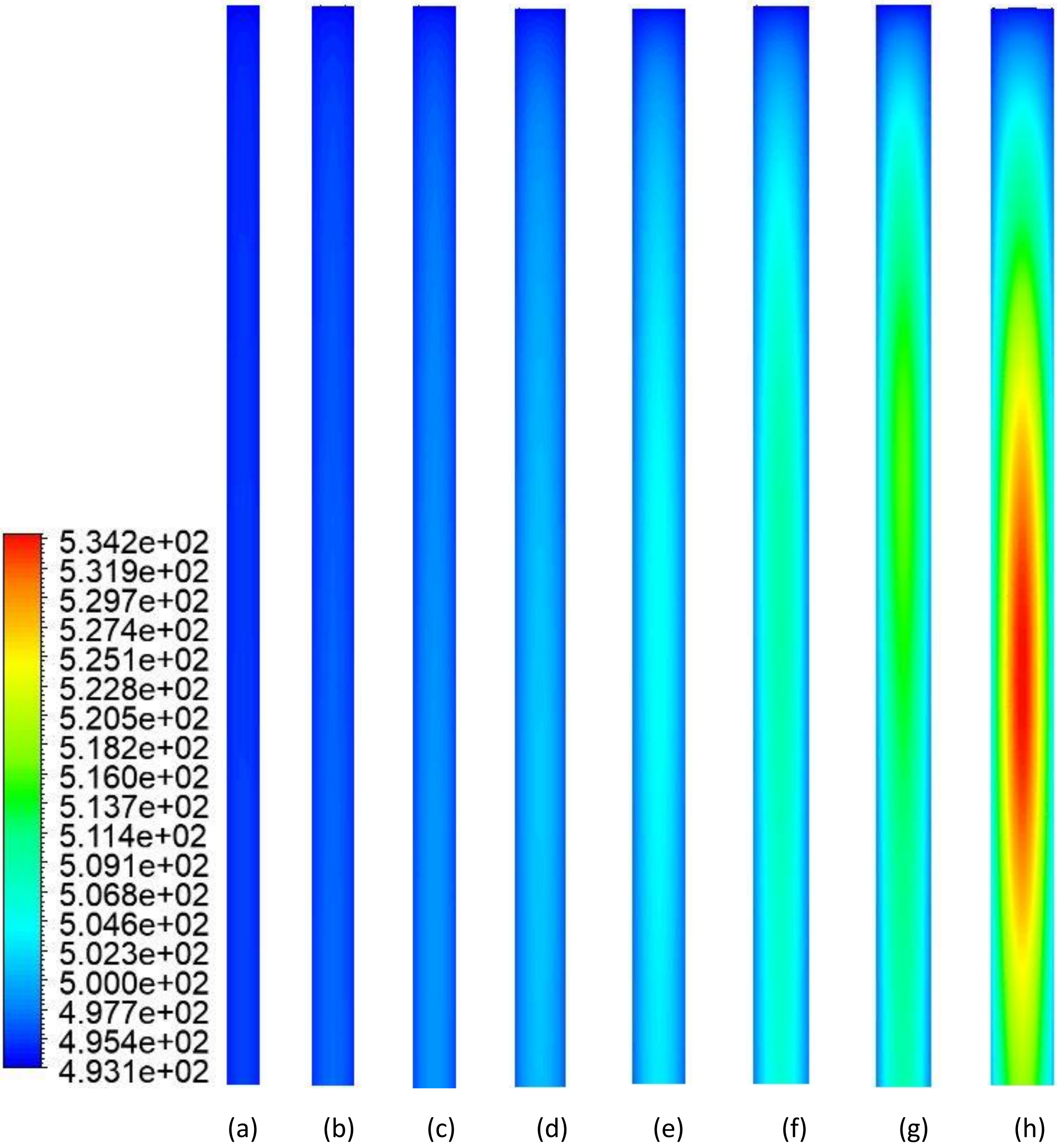

Figure 5-28 Temperature contours of plate type reactors of different plate spacing (a) 0.03m (b) 0.04m (c) 0.05m (d) 0.06m (e) 0.07m (f) 0.08m (g) 0.09m (h) 0.1m. These figures were not to geometric scale. Their purpose was to give a thermal comparison between (a) to (h)

Figure 5-29 shows temperature contours of a tube of tube radius 0.08m and a plate of plate spacing 0.1m for the same temperature legend. Just like Figure 5-27 and Figure 5-28, this figure does not show the full length of the reactor. They only show the top portion where significant temperature rise was seen. Both the contours show equal lengths of the reactor.

These contours represent the tube and plate with maximum temperature rise in their respective categories. They were created using same legend to present a comparison of the hotspot location and size. Figure 5-27 and Figure 5-28 cannot be used for this purpose of comparison because they employ different legends. Even though the hotspot temperature in the tube was larger than the hotspot temperature in the plate, the difference was not much, and hence a comparison can be made.

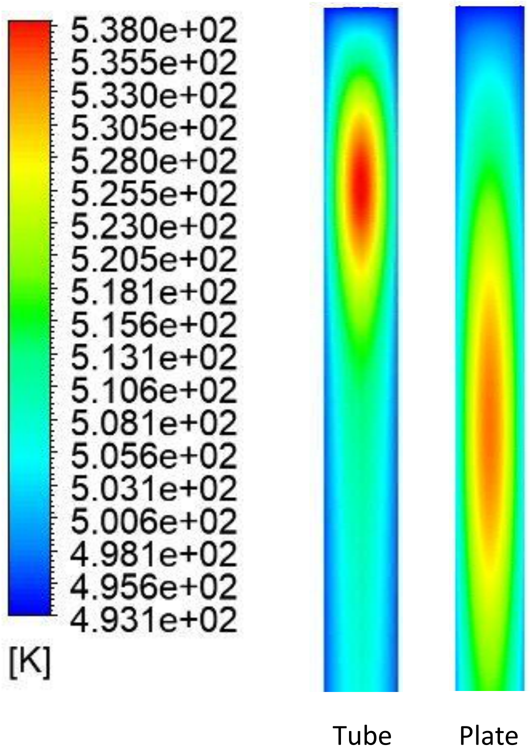

Figure 5-29 Temperature Contours of a tube of tube radius 0.08m and a plate of plate spacing 0.1m. These figures were not to geometric scale. Their purpose was to give a thermal comparison between tube and plate reactor

As it can be clearly seen that the hotspot was closer to the inlet for a tube compared to the hotspot in the plate type reactor. This behaviour of shifting of the hotspot location towards inlet as the hotspot temperature rises was also be observed in Figure 5-5, Figure 5-6 and Figure 5-7. Temperature rise with increasing plate spacing/ tube radius was the reason behind the shift. Rise in temperature leads to faster reactions and release of large reaction heat. Since the contours do not show the entire reactor length, the difference in the closeness to the inlet for both cases seems magnified compared to when looked at from the entire reactor length.

From Figure 5-29 it can also be noted that the hotspot was more diffused in case of a plate reactor compared to a sharp hotspot for the tube. A sharp hotspot was more likely to lead to a thermal runaway compared to a diffused one. This behaviour can also be observed from Figure 5-30. It might also be one of the reasons why a tube attains a thermal runaway at smaller radius compared to a plate with corresponding plate spacing.

Figure 5-30 compares a plate type reactor and a tubular reactor for plate spacings and corresponding radii respectively, keeping all other conditions same. The plate spacing/radii range from 0.03m-0.08m as thermal runaway was achieved for tube reactor for 0.09m.

All the contours in Figure 5-30 (a) – (f) do not follow a single legend. The legend for the contours in (a), (b) and (c) was given on their left, while the contours in (d), (e) and (f) follow the legend given on their left below the legend for (a), (b) and (c). The choice of legends was based on accommodating the lowest temperature in both reactors (493.15 K) and the highest temperature observed in the tubular reactors. Out of the two reactors in each picture in (a) – (f), tubular reactors were on the left, while plate type reactors were on the right.

The temperature inside the plate reactors can be seen to be always smaller than the tubular reactors at all plate spacings and corresponding radii.

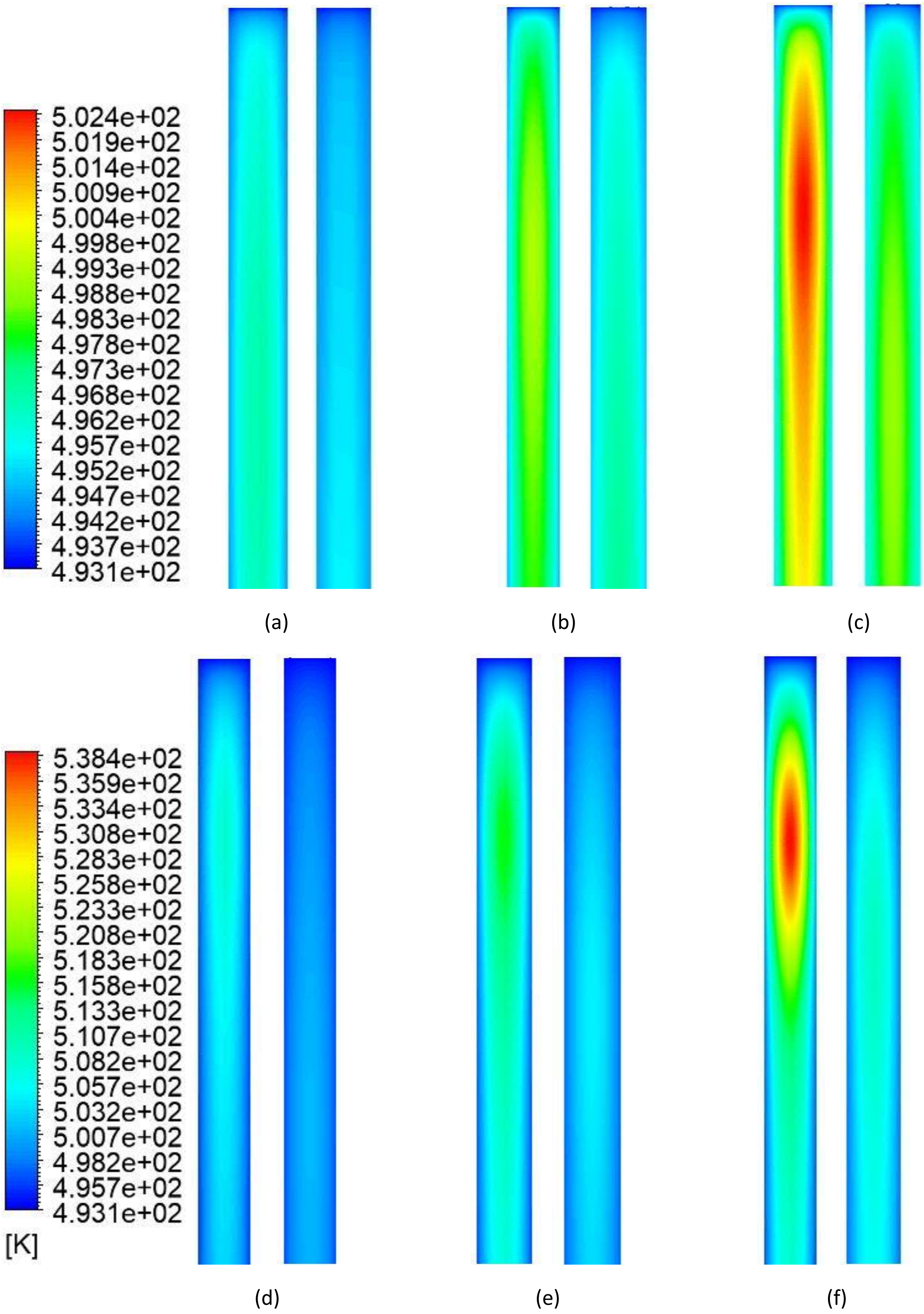

Figure 5-30 Temperature contours comparing a tube and a plate type reactor for various plate spacings/radii (a) 0.03m (b) 0.04m (c) 0.05m (d) 0.06m (e) 0.07m (f) 0.08m. These figures were not to geometric scale. Their purpose was to give a thermal comparison between the plate and tube reactors from (a) to (f)

Figure 5-31 shows a comparison of plots of temperature profiles along the reactor lengths for tube and plate type reactors of different plate spacings/radii. The profile was shown along a line in the centre of the reactor in order to capture the maximum temperature in the reactor. The temperature in the tube was found to be higher than corresponding plate type reactors throughout the entire reactor length. The difference in temperature rose with increasing plate spacing/radii.

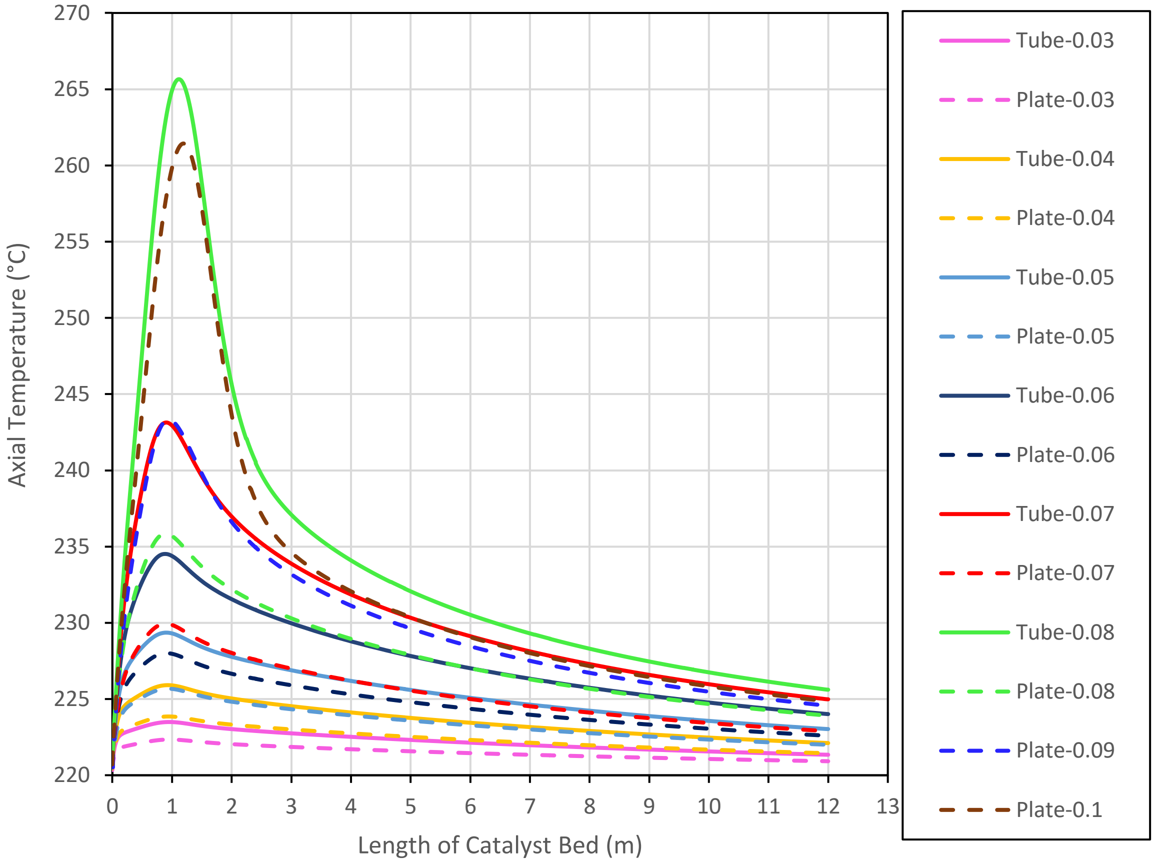

Figure 5-31 Plot of temperature along reactor length for different plate spacings for plate type reactors and for corresponding radii for tubes

The dotted lines represent the temperature profiles for the plate type reactors and solid lines were for the tubular reactors. The temperature profiles of a tube and a plate of a particular radii and corresponding plate spacing respectively were represented by one colour.

The hotspot temperature went upto 538.8 K for a radius of 0.08m in case of a tubular reactor while it reached a maximum temperature of 534.6 K for a plate spacing of 0.1m in case of a plate type reactor. This meant that the maximum hotspot temperature achievable in a tube was higher than the maximum hotspot temperature achievable for a plate type reactor despite having a smaller corresponding tube radius.

Radial temperature profiles were obtained at the location of hotspots for the tubes and plates at different plate spacings and radii and were shown in Figure 5-32. The colour coding for the plots was kept same as the axial profiles in Figure 5-31. The dotted lines show the profiles for plate reactors while the solid lines represent tubular reactors. The centre of a hotspot on the vertical axis in the centre of the tube reactor and the plate reactor was taken to be the origin on the x-axis. An additional plot for a tube of radius 0.02m was included in Figure 5-32. Data points were shown with solid dots and were joined using straight lines to obtain the plots. Non-symmetrical plots around the axis (for example, plate spacing 0.09m and 0.08m) were a result of unavailability of the nodes in the model mesh near the walls.

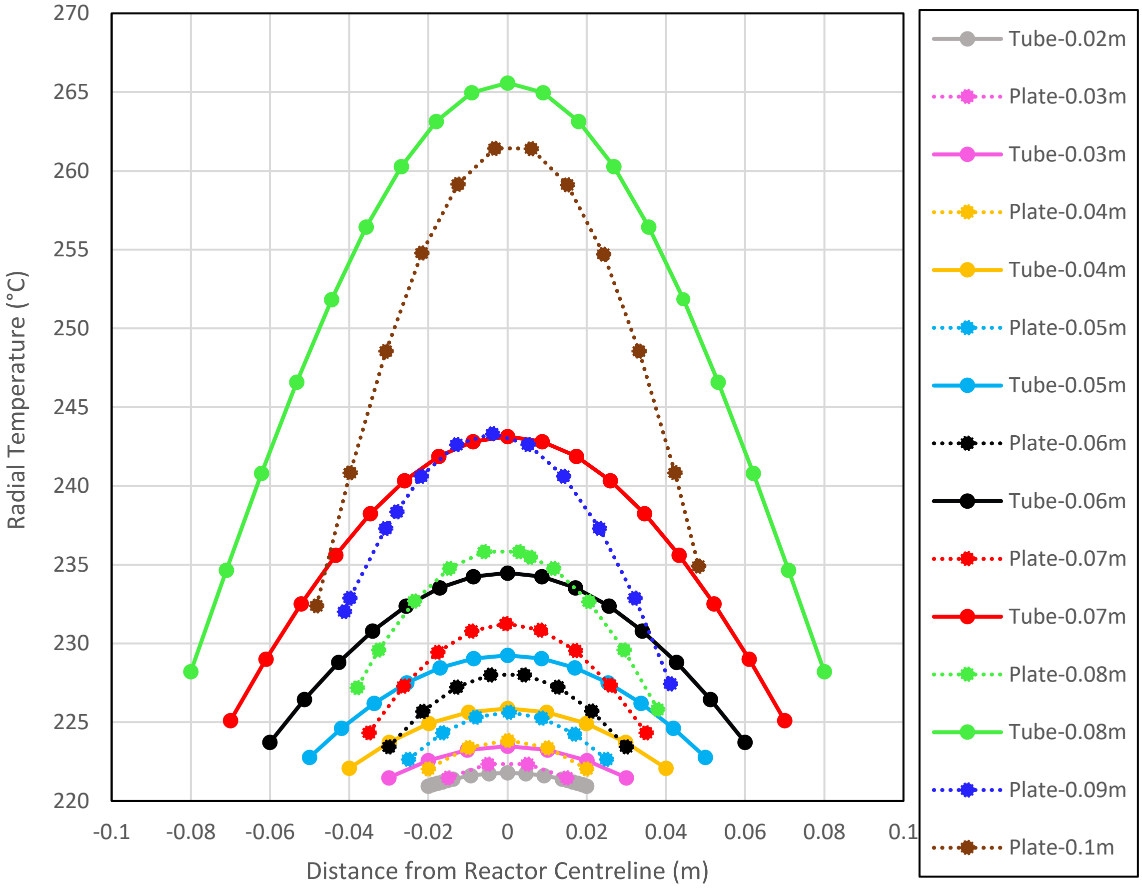

Figure 5-32 Radial Temperature profiles of tube and plate reactors at the location of a hotspot

A difference in the shape of the profiles for the tubular reactors and the plate reactors can be observed in Figure 5-32. If the plots having similar hotspot temperatures were to be compared (for example, tube radius 0.07m and plate spacing 0.09m; tube radius 0.06m and plate spacing 0.08m; tube radius 0.04m and plate spacing 0.05m), the plots for the tube reactors appear to be wide while the plots for the plate type reactors seem to bulge out more than the tubular reactors. In other words, plots for the plate type reactors were more concave with respect to x-axis compared to the plots of tube reactors.

A very convenient diagram for visualising the problem of a steady state non-isothermal problem was the conversion vs. temperature plot (Froment and Bischoff, 2004). CO conversion measured along the length of catalyst bed was thus plotted for temperatures along the centreline and was shown in Figure 5-33. Similar to Figure 5-31 and Figure 5-32, the conversion profiles of a tube and a plate of a particular radii and corresponding plate spacing respectively were represented by one colour.

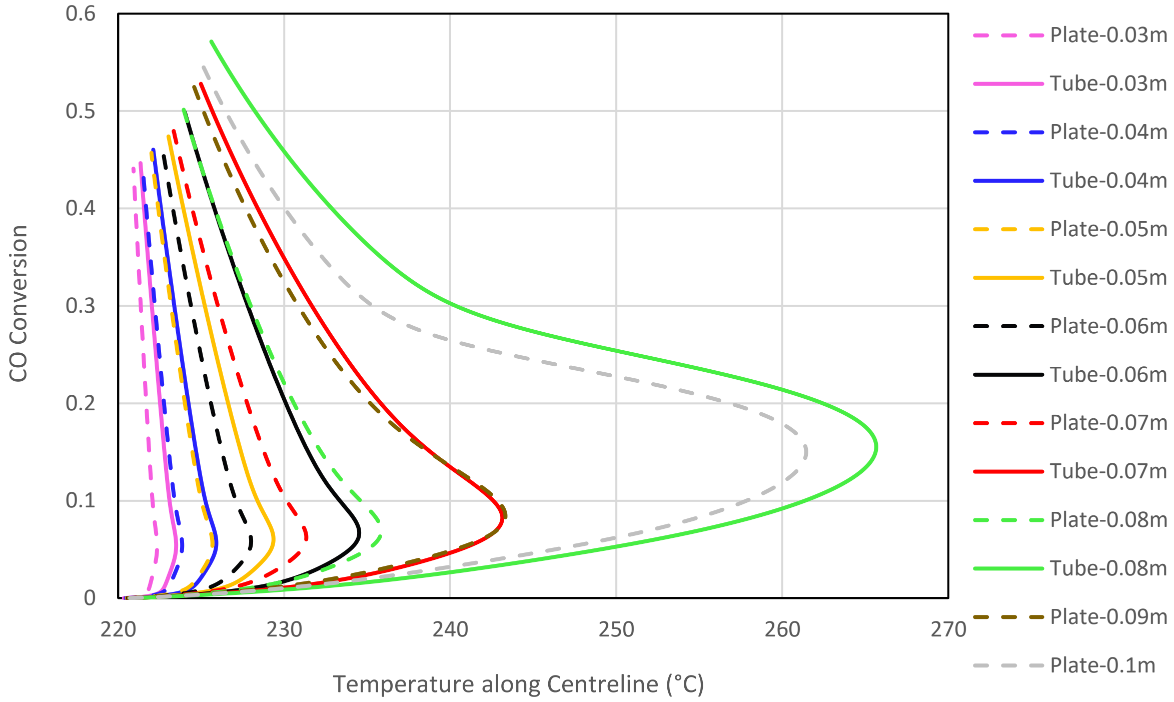

Figure 5-33 Conversion vs. centreline temperature for tube and plate reactor at different radii and plate spacings respectively

Figure 5-33 allows a comparison of the different reactors under conditions of similar catalyst performance, which was not shown by other figures. It shows for conditions of r=t (comparing the same colours), Tmax was always higher in the tube reactor but there was a big difference in the conversion and thus the reactors were not performing at the same production rate. When comparing at the same production rate (same conversion, as best as possible) the plate reactor will always meet the conditions t>r but t<<d, but the temperature profiles were in this case quite similar. For example, if tube reactor with radius 0.07m was compared to the plate reactor of plate spacing t=0.09 and tube reactor of radius 0.06m was compared to plate reactor of plate spacing 0.08m, it shows that based on the temperature profile, neither reactor performs better than the other. It shows that the plate reactor provides a more compact design, for example, a plate reactor of plate spacing of 90mm was as good as a tube reactor of diameter of 140mm in terms of heat transfer behaviour. The primary reason behind this phenomenon was the area/volume equivalence (r=t) for the two reactors. Thus, the plate reactor has more efficient heat removal per unit volume.

Having studied the relationship between conversion and temperature, effect of conversion was studied on one of the product species. Methane mole fraction was plotted as a function of CO conversion and was shown in Figure 5-34. It shows that the plots which have similar CO conversion profiles in Figure 5-33, for example, tube radius 0.07m and plate 0.09m, and tube radius 0.06m and plate 0.08m, produce similar concentration of species at all the conversions.

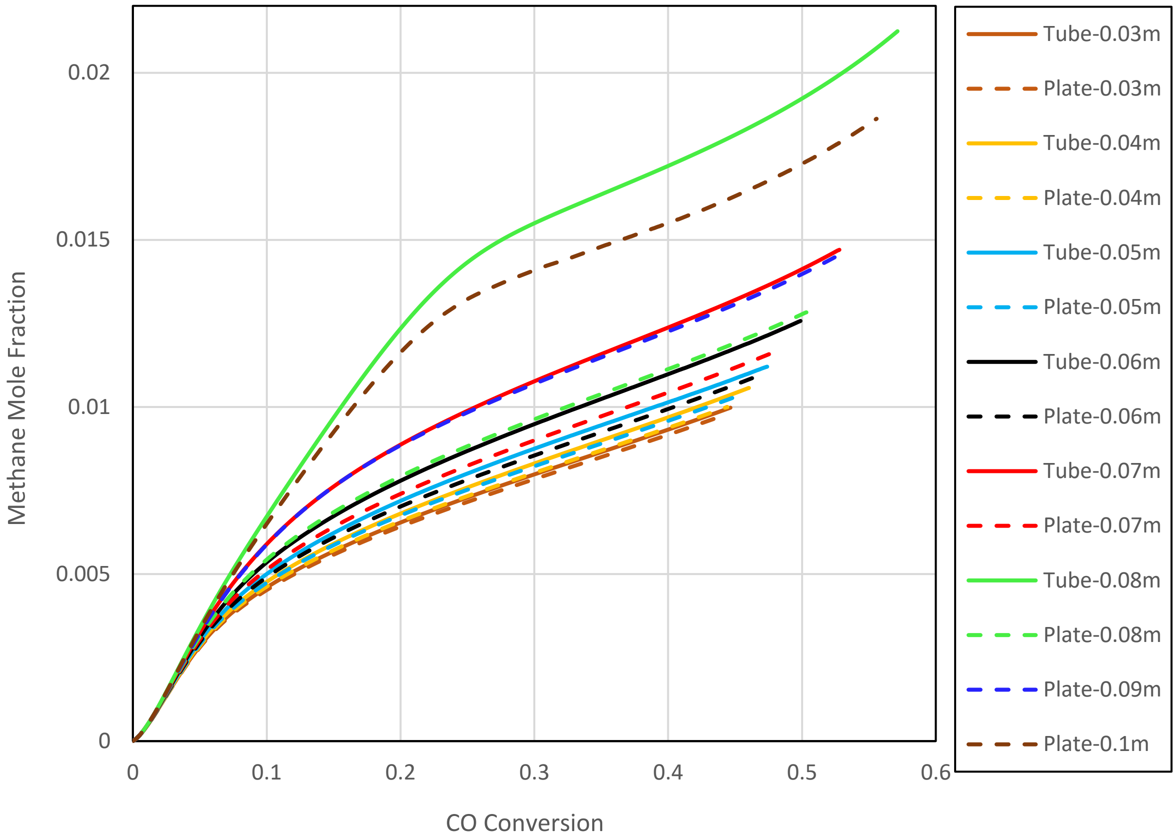

Figure 5-34 Plot of Methane mole fraction along centreline versus CO conversion along the centreline

To further analyse heat transfer capabilities of both geometries, heat transfer coefficients were plotted for increasing radii/plate spacing in Figure 5-35. Heat Transfer Coefficients were indicative of the heat transfer capabilities of any system.

A plate reactor has two plates providing surface area for heat dissipation while a tube has one continuous surface for heat dissipation. The integral heat flux reported by Ansys was reported for a single reactor wall. This value was, thus, doubled for the plate reactors. Area was calculated for two plates for the plate type reactors and for single continuous surface for tube reactors. A sample calculation to calculate the heat transfer characteristics of both the geometries was shown in Table 5-7. The calculation of heat transfer coefficients for the rest of plate spacings and radii were shown in Appendix G.

Table 5-7 Sample Calculation to show the calculation of heat transfer coefficient for a plate spacing and radius of 0.03m and 0.04m

Tube Radius /Plate Spacing (m)	Integral of Heat Flux (w)	2 x Integral of Heat Flux (w)	Volume-weighted average Temperature	Steam Temperature (K)	ΔT = Volume Avg. Temp - Steam Temp (K)	Area (m2)	Integral of Heat Flux /Area (w/m2)	Heat Transfer Coefficient (w/m2.k)
Plate								
0.03	113928.6	227857.2	494.61	493.15	1.46	24	9494.05	6494.77
0.04	152614.1	305228.2	495.30	493.15	2.15	24	12717.84	5911.43
Tube								
0.03	21564.75	NA	494.81	493.15	1.65	2.26	9538.55	5758.25
0.04	39110.09	NA	495.67	493.15	2.52	3.01	12974.42	5142.66

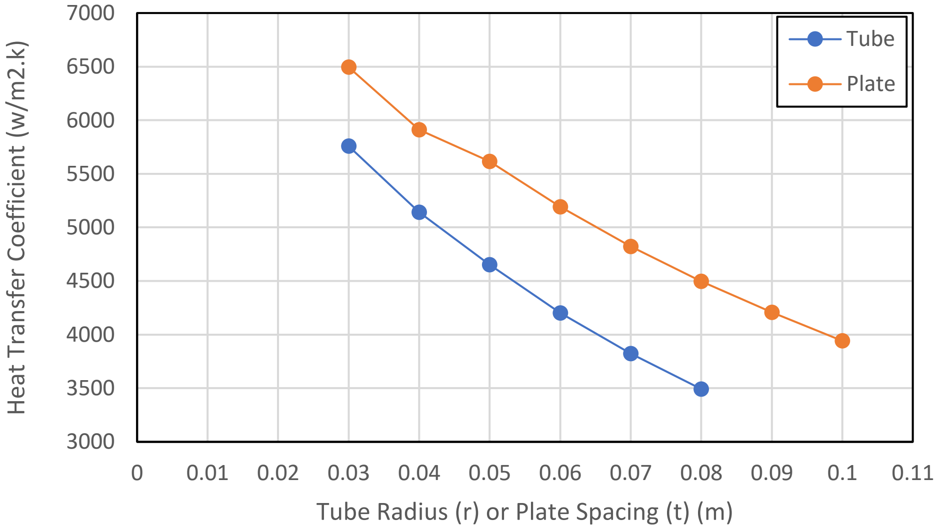

Figure 5-35 Comparison of the heat transfer Coefficients of a tube and plate at different radii and plate spacings respectively

As it can be seen from Figure 5-35, the heat transfer coefficients for a plate reactor was higher than the tube reactor at all plate spacings/radii by a large margin. This behaviour explains such good heat transfer and prevents the thermal runaway in the plate reactors more than the tube reactor.

Different heat transfer behaviour and CO conversions were bound to bring differences in the product distribution of the two geometries. Following section describes these differences for the two geometries for increasing plate spacing/radii.

5.4.1.3 Product Distribution

Figure 5-36 represent the product distribution for paraffins from C_2 to C_{20} and for olefins from C_3 to C_{20} respectively for the two geometries. Product distribution for the paraffin-methane (C_1) and olefin- Ethene (C_2) has been plotted and discussed separately in Figure 5-37. The dotted lines represent the temperature profiles for the plate type reactors and solid lines were for the tubular reactors. The temperature profiles of a tube and a plate of a particular radii and corresponding plate spacing respectively were represented by same colour.

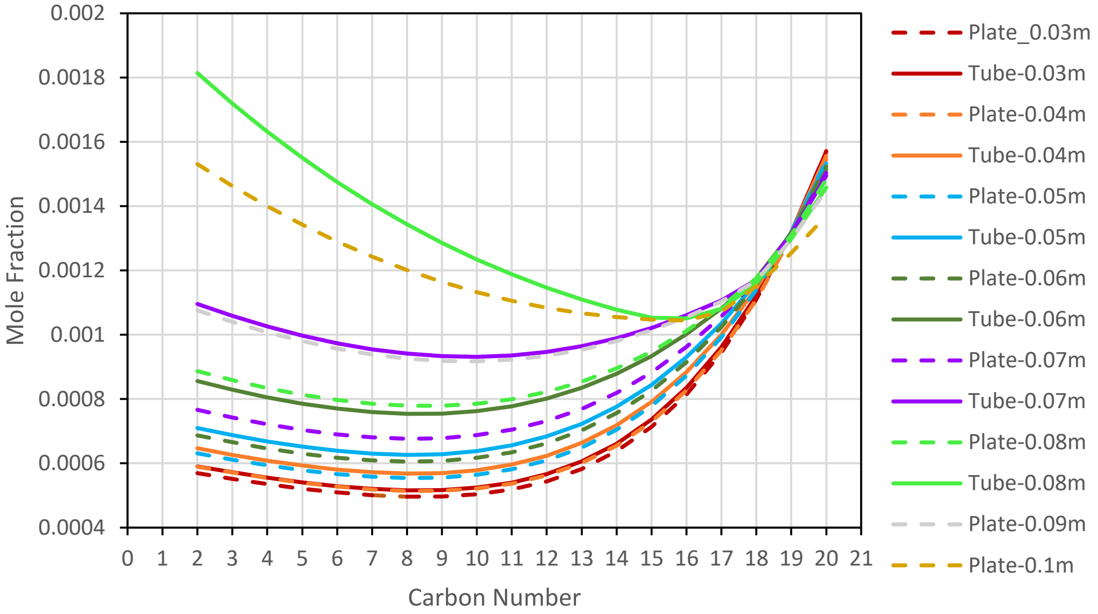

(a)

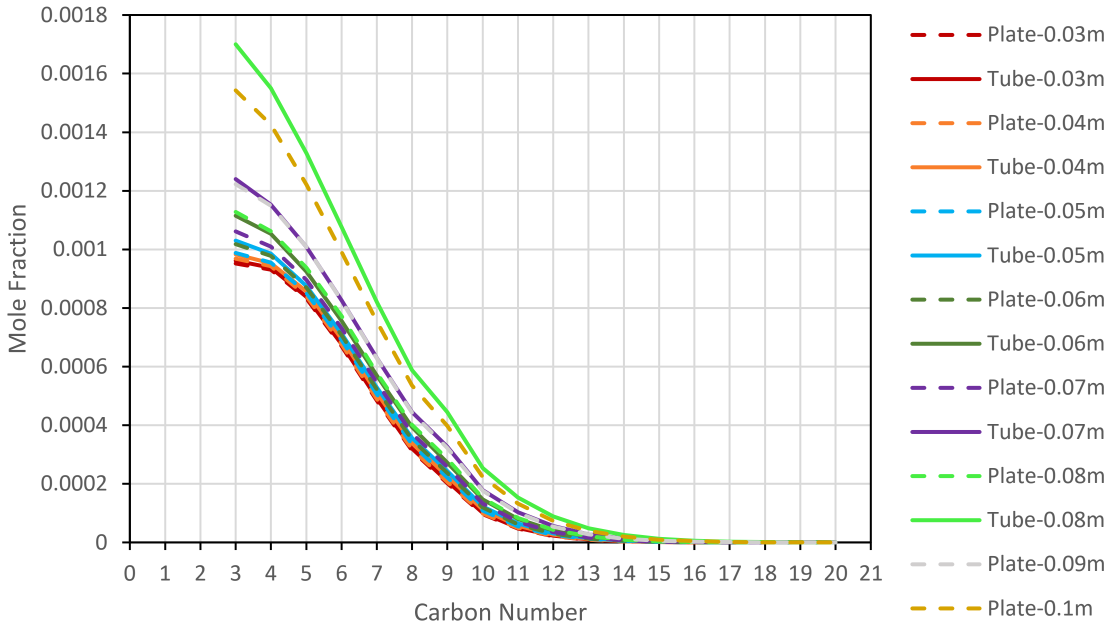

(b)

Figure 5-36 Product Distribution of (a) paraffins and (b) olefins of tubes and plates at different radii and plate spacings respectively

From *Figure 5-36* the mole fractions of the paraffins and olefins for the plate type reactor can be seen to be lower than corresponding tube reactors. This behaviour was in accordance with lower CO conversions observed for plate reactors compared to the tube reactors. However, CO conversion was not the only factor responsible for these differences. If the tube and plate with maximum CO conversions i.e. tube of 0.08m radius and the plate of 0.1m were to be considered, there CO conversions do not differ by a large difference. The CO conversions for the tube and plate were 57.151% and 55.584% respectively. However, their product distributions for the paraffins as well as olefins differ by a large amount. This confirms that the different heat transfer behaviour in the two geometries produces different product distributions for large tube radius and plate spacings. This also indicates the role of different flow patterns for the two geometries having a role in producing different product distributions.

For small tube radius and plate spacing, the product distributions for the tube and plate reactors has very little differences. For small tube radius and plate spacing, the differences in temperature rise ΔT and CO conversions in *Figure 5-21* and *Figure 5-22* were also small. Therefore, for a small tube radius and plate spacing, a tube and a plate reactor behave similarly.

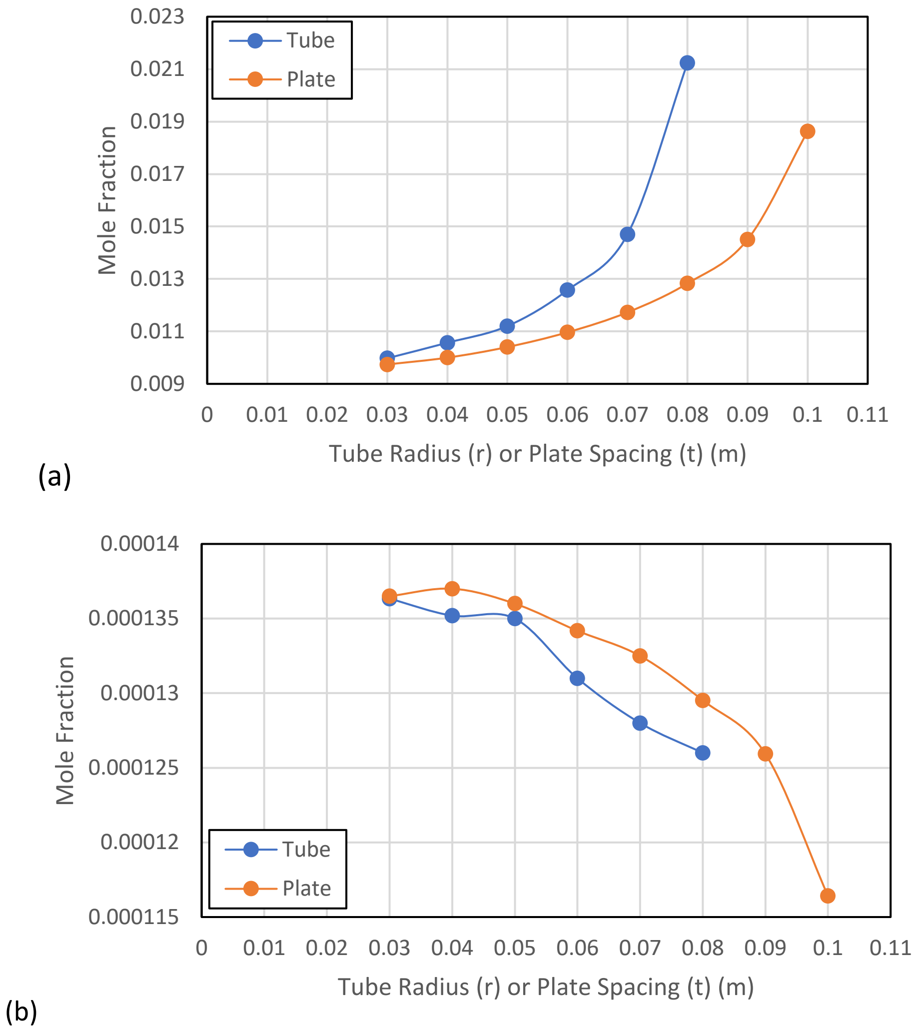

Figure 5-37 Product distribution for (a) Methane (b) Ethene for a tube and a plate type reactor at increasing plate spacing/radii

Figure 5-37 show product distributions for paraffin- Methane (CH_4) and Olefin- Ethene (C_2H_4) for tube and plate reactors for increasing plate spacing/radii. The species Methane and Ethene were plotted separately to overcome the issue of different scales as they have too high and too low concentrations respectively compared to the other members in both the series. The difference between the plots of the two geometries for olefins was small, but the paraffins show significant differences. The difference between the two plots for the paraffins increases with the plate spacing/radii, which was in accordance with the increasing temperature in the system.

5.4.2 Comparison on the Basis of Tube-to-Particle Diameter Ratio

Figure 5-38 shows the temperature profiles of a tube of diameter 0.04m and plate of plate spacing 0.04m thus having equal tube-to-particle diameter ratio. The profiles were plotted at the central axis for both the geometries.

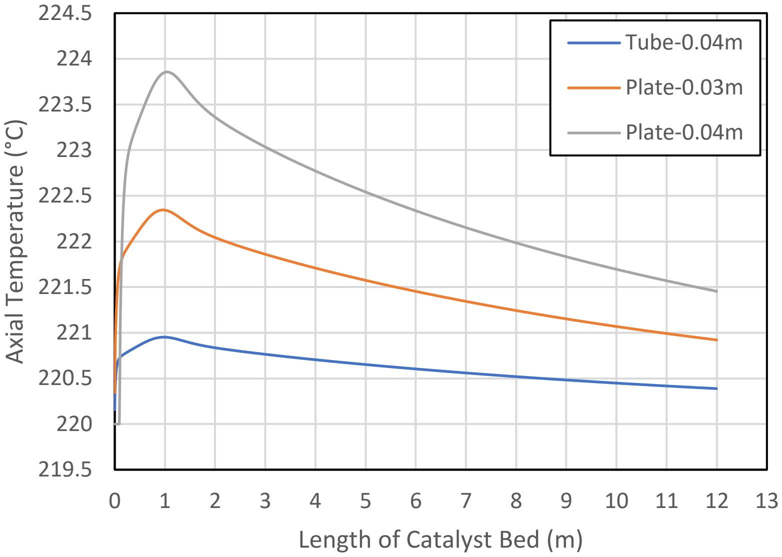

Figure 5-38 Comparison between Tube and plate reactors having same Tube-particle ratio.

The temperature plots for tube and plate can be seen to have large differences. For larger diameters this difference was expected to increase. This can be confirmed from Figure 5-31. The tube has much lower temperatures across the entire reactor length compared to the plate reactor. To present a better comparison, the temperature profile for a plate of plate spacing 0.03m has also been plotted in the same graph. As it can be observed, the tube reactor presents better temperature control than the plate reactor of plate spacing 0.04m despite having a larger tube-to-particle diameter ratio. Hence, the tube exhibits better heat transfer capabilities compared to the corresponding plate type reactor. This establishes superiority of tubular reactors over the plate reactors if compared on the basis of tube-to-particle ratio.

However, if the comparison was to be made on the basis of fluid flow and heat dissipation surface area per volume, the plate reactors provide a better performance over the tubular reactors. Hence, the superiority of one reactor over the other was dependent on the criterion they were being compared for.

5.4.3 Plate Representation in COCO

After comparing the plate type reactors and the tube reactors in Ansys, the tubular model in COCO was tuned to represent a plate type reactor. It was practically not possible to model a plate type geometry in COCO. Therefore, the tubular geometry in COCO having the same length as the plate geometry and the radius of same length as the plate spacing in Ansys was tuned using the results of Ansys plate type reactor to represent a plate type reactor in COCO.

The heat dissipation behaviour of a plate type geometry in Ansys was used as a reference to tune the heat transfer behaviour of the tubular plug flow reactor in COCO. It was done by tuning the overall heat transfer coefficient, based on maximum temperature (hotspot temperature), in COCO so that the hotspot temperature in COCO matches with the plate type reactor's hotspot temperature in Ansys at various plate spacings/radii from 0.03m to 0.09m. A plot of CO conversion observed for the plate type reactor in Ansys and for the tuned tubular reactor in COCO was shown in *Figure 5-39*.

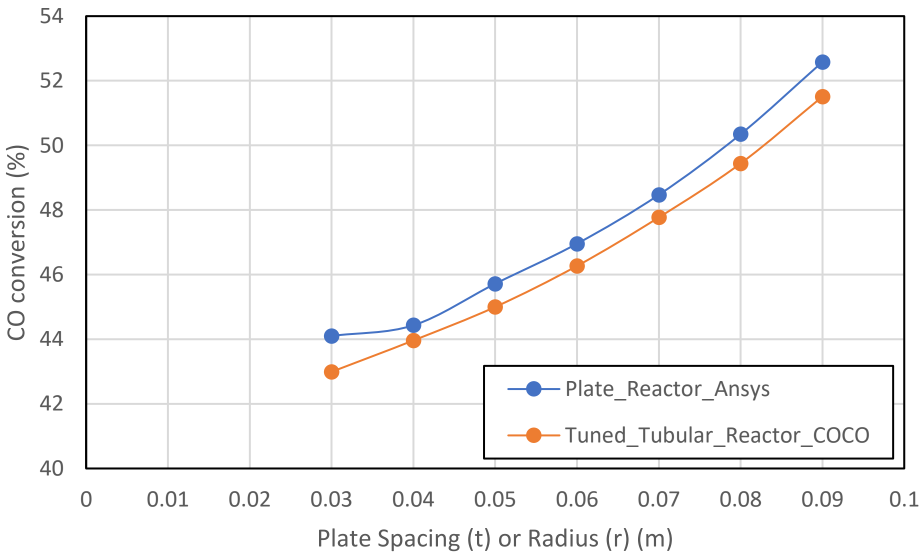

Figure 5-39 Plot comparing CO conversions obtained for a plate type reactor in Ansys and COCO

The CO conversion values were quite close for both cases at various plate spacings/radii. Such close resemblance in the two cases show that the tuned tubular model in COCO can efficiently represent a plate geometry. Heat transfer coefficient tuning can thus also be used to model various other geometries in COCO.

6 Chapter - Conclusions and Recommendations

6.1 Conclusions

The objectives of this project, as given in Chapter 1, were realised and a complete CFD model was developed. This CFD simulation was based on an approach of employing thermodynamics and kinetics in an integrated manner. The reaction mechanism that was followed to develop the rate expressions represented the chain behaviour of FTS reactions. Such a CFD model hasn't been developed yet and this model was novel in that manner.

In the first part of the project, mass balance and energy balance were analysed to ensure the conservation of mass and energy in the system. The 2D CFD reactor model was compared with a 1D model reproduced in COCO for the same operating conditions. Results obtained from both the softwares showed close agreement and, hence, assured that the kinetics was working properly.

The other part of the project deals with the plate type reactors. The plate type heat exchangers have been claimed to be better than the shell and tube heat exchangers in terms of their heat transfer capabilities by various sources in literature. Taking a motivation from such claims, heat transfer capabilities of the plate type reactors were explored relative to the tubular reactors.

6.1.1 Developing the 2D CFD model for Tubular Reactor

The 2D CFD model for tube reactor was simulated for isothermal and non-isothermal conditions. For isothermal conditions, the CO conversion kept increasing with increasing steam temperature.

For non-isothermal conditions, the CO conversions obtained were a little higher than the isothermal conditions. Good heat dissipation was observed. The hotspot temperature was seen to rise with increasing steam temperature. The product distribution observed was similar to the isothermal case.

6.1.2 Comparison between 1D and 2D model

Comparing temperature profiles from Ansys and COCO revealed that latter reports volume-averaged value of temperature profile. As a result, the hotspot temperature reported by the 1D model was an averaged and hence, underestimated value. The other reason behind this observation was the use of a constant $U_{overall}$ value for the entire reactor geometry in COCO.

Different product distributions at non-isothermal conditions and almost identical product distributions at isothermal conditions for Ansys and COCO confirmed the same.

6.1.3 Effect of Conversion and Temperature

To study the effect of temperature, product distributions were compared at same conversions for different temperatures. Similarly, to study the effect of conversion, product distributions were obtained at different conversions for a steam temperature of 220°C. Conversion was found to increase the mole fraction of the species but not change the shape of the distribution while increasing temperature was found to change the shape of the distribution.

6.1.4 Tube Reactor vs. Plate Type Reactor

A parametric study was carried out taking the plate spacing and radius as parameters for the plate and tube reactors respectively on the basis of two criteria. One criterion was based on the physical similarity of the two reactors. This included equating the Reynolds number and the surface area to volume ratio. Another criterion was based on tube-to-particle diameter ratio.

6.1.4.1 Comparison on the basis of Surface Area to Volume Ratio

Both the parameters were found to have a huge role on the heat dissipation, and as a result, on the temperature control inside the reactor. The hotspot temperatures were found to increase with increasing plate spacing and radii.

The location of hotspot was found to shift towards the inlet with increasing radii and the plate spacing for both the reactors.

After a certain value of plate spacing and radius, thermal runaway was observed for both the reactors. However, it occurred in the tube reactor for a shorter radius compared to corresponding plate spacing. The temperature runaway occurred at a radius between 0.08m and 0.09m for the tube reactor while for the plate reactor it occurred between 0.1m and 0.11m.

At a particular plate spacing/radii, entire temperature profile along the reactor axis was found to have higher temperature than corresponding plate reactor temperature profile. Since the temperature inside the tube reactor was higher than the plate reactor at each plate spacing/radii, the CO conversions observed for the tube reactor was also higher than the plate reactor.

The product distributions at the isothermal and the non-isothermal conditions revealed that heat dissipation mechanisms were the dominant factor behind the differences in the heat transfer characteristics as the two geometries had almost identical product distribution at isothermal conditions, whereas the non-isothermal product distributions showed significant differences.

The radial temperature profiles were obtained for the two geometries at different plate spacings and radii. The profiles indicated that different heat transfer mechanisms were being employed in the two geometries as the profiles differed in shapes when compared for similar hotspot temperatures.

Overall, a plate type reactor was observed to exhibit better heat transfer behaviour than the tube reactor when compared for same heat dissipation surface area per unit reactor volume. A comparison between the heat transfer coefficients for the two geometries confirmed the same.

6.1.4.2 Comparison on the Basis of Tube-to-Particle Diameter Ratio

Tube reactor outperformed the plate reactor in terms of heat transfer when compared on the basis of tube-to-particle diameter ratio.

6.1.5 Plate Representation in COCO

The 1D tubular model in COCO was tuned for its overall heat transfer coefficient using the heat transfer coefficients from the plate type reactor model in Ansys to represent a plate type reactor in COCO. The 1D model could successfully represent a plate type reactor as CO conversions obtained in Ansys and 1D PFR (COCO) model at different plate spacings/radii were close.

6.2 Recommendations

The study carried out in this thesis provides a scope for further investigations that can be done using the model developed here.

There were numerous ways in which the current model can be improved to provide a more realistic picture of the FT reactor. The area of reaction kinetics and reactor design were two such areas that were discussed here. Reaction Kinetics refers to the kinetic model employed to describe the reaction mechanism and derive expressions for the reaction rates while reactor design revolves around a variety of factors like catalyst configuration inside the reactor, the design of plates, plate orientation etc.

Some improvements and potential future investigations using the current model in the domain of reaction kinetics and domain were enlisted below.

6.2.1 Reaction Kinetics

1. The model can be extended to larger number of product species by including more members of the paraffin and the olefin series. In the current model, 20 product species of each series have been considered. Truncation of the product spectrum at N = 20 has led to altering the product distribution. Extending the number of species can lead to providing a better representation of the product distribution achieved in the real reactors.

2. Even though the formation of liquid occurs in small quantities in FTS, it has a significant effect on the product distribution and selectivity (Mthombeni, 2009; Davies and Möller, 2021a). It can also have a considerable effect on the catalyst effectivity. The formation of liquid can wet the catalyst the particles and fill the catalyst pores. When the liquid fills the catalyst pores, the presence of the liquid phase may also lead to the partial catalyst deactivation by filling and hence blocking some of the pores. When the liquid was present in the void spaces between the catalyst particles, it plays a very important role by manipulating the effective thermal conductivity coefficient of the bed (Zhu *et al.*, 2010). Therefore, it may impose internal and external mass transfer limitations to the reactions (Caldwell and Vuuren, 1986; Visconti and Mascellaro, 2013 & Visconti, 2014). Since the liquid can affect the reaction in so many ways, the formation of liquid phase should be taken into account and the equilibrium between gas and liquid phase should be modelled to study the effect of VLE on the production selectivity, yield, and the heat dissipation behaviour using the current model.

3. While the formation of branched and isomeric compounds was completely ignored in this project, it can be taken into account to obtain a more realistic product distribution. This can be useful for gaining insights into the conditions which maximise the

production of a particular class of desired compounds, for example gasoline and naptha.

4. While only LTFT was considered in this project, the developed model can also be expanded to simulate the HTFT process.

6.2.2 Reactor Design

1. The reactions considered in this project were assumed to occur in the entire volume of the catalyst bed and the geometry of catalyst particles was not included in the reactor geometry. The solid catalyst particles' geometry can be created inside the reactor. This will provide us gain insight into the actual catalyst area present for reactions and the actual pressure drop that occurs in the catalyst zone created by the catalyst particles. In this way the current model can be used to model the catalyst particles geometry while retaining the chain reaction behaviour of the FT reactions.
2. Plate type reactors which have a plate of a shape of a rectangle was used for study in this project. Plates of other shapes and sizes can be studied for their heat transfer properties and the effect of shape and size of a plate on the heat transfer capabilities of the plate reactor system can be analysed.
3. In most Plate Heat exchangers, the plates have corrugations that exert a strong influence on the thermal-hydraulic performance of the device. An example of a zigzag corrugation was shown in *Figure 6-1*. The plate used for the current study was assumed to be flat with no corrugations.

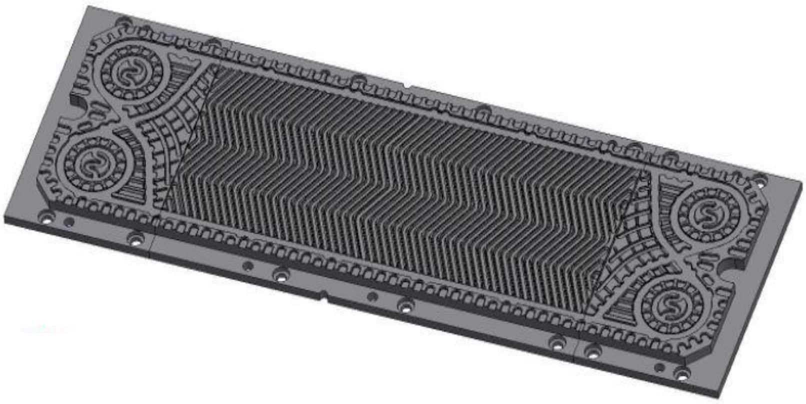

Figure 6-1 A corrugated plate from a Plate Type Heat exchanger

Several other types of corrugations were used in the PHEs. Some of the main types of plate corrugations were shown in

Figure 6-2. The channels formed between the adjacent plates impose a swirling motion to the fluids and also increase the surface area available for the heat dissipation (Mota, Caravalho and Ravagnani, 2015).

These modifications when adapted in the plate type reactor, can enhance the heat dissipation which can result in a better temperature control inside the reactor. This was already in practice for the tubular reactors which are currently in practice in industries. High performance tube reactors were rough on the outside to improve heat transfer.

However, corrugations on the inside surface raise some problems with the packing and removing catalyst. Therefore, the practical side of this modification needs to be explored in detail. The current model can, however, be used to computationally study the effect of such modifications in a reactive system by including the corrugations in the design of the tube or plate reactor geometry.

4. The project was carried out keeping the Reynolds number constant for all the comparative studies. It can be varied to determine the Re number at which the agreement between the two models ceases to exist. A plot of Reynolds-Peclet number region could be made to understand the transition zone where flow pattern begins to have impact on the product distribution as well as heat transfer in the reactor.

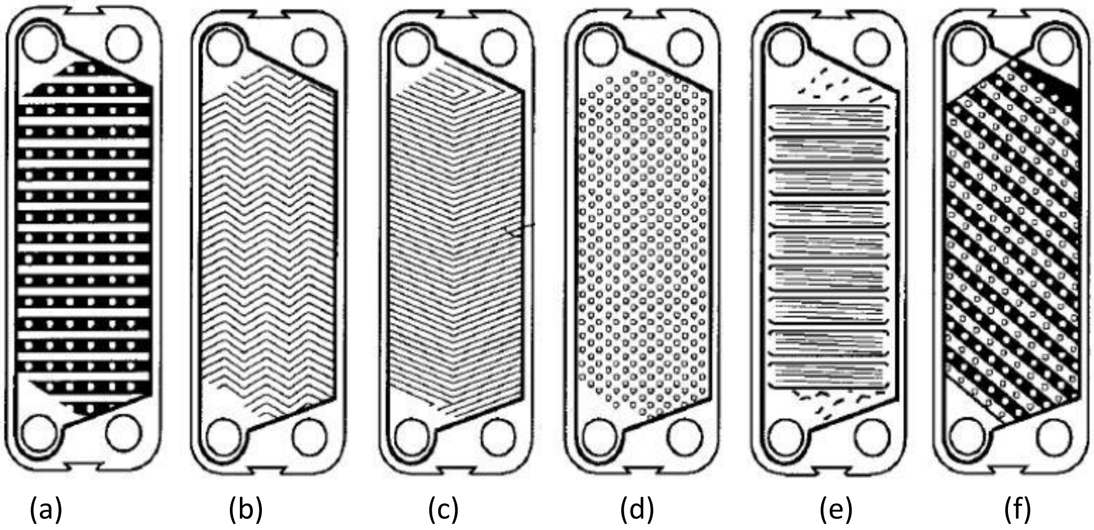

Figure 6-2 Typical categories of plate corrugations (a) Washboard (b) Zigzag (c) Chevron or herringbone (d) Protrusions and depressions (e) Washboard with secondary corrugations (f) Oblique washboard, reproduced from the reference Mota, Caravalho and Ravagnani, 2015

5. Only a single plate type reactor and single tube reactor was analysed in the current project. However, in the real reactor system, usually a combination of tubes is used to reach the target yield. A group of such reactors can be modelled to find out how the heat dissipation in a combination of reactors work out and also a comparative study between a single tube/plate reactor and a network of reactors can be carried out to understand the difference between both.

7 Bibliography

Ahón, V. R., Costa, E. F., Monteagudo, J. E. P., Fontes, C. E., Biscaia, E. C., Lage P. L. C. (2005) 'A comprehensive mathematical model for the Fischer-Tropsch synthesis in well-mixed slurry reactors', *Chemical Engineering Science*, 60(3), pp. 677–694. doi: 10.1016/j.ces.2004.08.039.

Alba Mena Subiranas and Schaub, G. (2009) 'Combining Fischer-Tropsch (FT) and Hydrocarbon Reactions under FT Reaction Conditions : Model Compound and Combined-Catalyst Studies', *INTERNATIONAL JOURNAL OF CHEMICAL REACTOR ENGINEERING*, 7.

Aligolzadeh, H., Jebreili Jolodar, A. and Mohammadikhah, R. (2015) 'CFD analysis of hot spot formation through a fixed bed reactor of Fischer-Tropsch synthesis', *Cogent Engineering*. Cogent, 2(1). doi: 10.1080/23311916.2015.1006016.

Allie, F. and Nyathi, J. (2019) *Micro-kinetic comparison of CO and CO2 hydrogenation over Fe (100)*.

Almeida, L. C., Echave, F. J., Sanz, O., Centeno, M. A., Arzamendi G., Gandia, L. M., Sousa-Aguiar, E. F., Oriozola, J. A., Montes, M. (2011) 'Fischer-Tropsch synthesis in microchannels', *Chemical Engineering Journal*, 167(2–3), pp. 536–544. doi: 10.1016/j.cej.2010.09.091.

AMBARITA, H., Kishinami, K., Daimaruya, M., Tokura, I., Kawai, H., Suzuki, J., Kobiyama, M., Ginting A., (2009) 'The Optimum Plate to Plate Spacing for Maximum Heat Transfer Rate from a Flat Plate Type Heat Exchanger', *Thermal Science and Engineering*, 17(1), pp. 1–8. doi: 10.11368/tse.17.1.

Andre, S. and Dry, M. E. (2004) *Fischer-Tropsch technology*, *Fischer-Tropsch technology*. Amsterdam ; Elsevier (Studies in surface science and catalysis, v. 152).

Anfray, J., Bremaud, M., Fongarland, P., Khodakov, A., Jallais, S., Scheweich, D. (2007) 'Kinetic study and modeling of Fischer – Tropsch reaction over a Co / Al 2 O 3 catalyst in a slurry reactor', 62, pp. 5353–5356. doi: 10.1016/j.ces.2006.12.035.

Ansys (2010) 'ANSYS Meshing User's Guide'.

Ansys (2013a) 'ANSYS Fluent Theory Guide', 15317(November), pp. 724–746.

Ansys (2013b) 'ANSYS Fluent User's Guide', 15317(November), pp. 724–746.

Arzamendi, G., Dieguez, P. M., Montes, M., Oriozola, J. A., Sousa-Aguiar, E. F., Gandia, L. M. (2010) 'Computational fluid dynamics study of heat transfer in a microchannel reactor for low-temperature Fischer-Tropsch synthesis', *Chemical Engineering Journal*, 160(3), pp. 915–922. doi: 10.1016/j.cej.2009.12.028.

Bar-Cohen, A. and Rohsenow, W. M. (1984) 'Thermally Optimum Spacing of Vertical Natural Convection Cooled Parallel Plates', *ASME JOURNAL OF HEAT TRANSFER*, 106, pp. 116–123.

Basha, O. M. (2016) 'COMPUTATIONAL FLUID DYNAMICS MODELING WITH EXPERIMENTAL VALIDATION OF THE COMPLEX SPATIO-TEMPORAL PHENOMENA IN SLURRY BUBBLE COLUMN REACTORS FOR FISCHER-TROPSCH SYNTHESIS'.

Blaum, E. (1974) 'Zur dynamik des katalytischen festbettreaktors bei katalysatordesaktivierung—I.', *Chemical Engineering Science*, 29(12), pp. 2263–2277. doi: https://doi.org/10.1016/0009-2509(74)80002-3.

Bodoia, J. R. and Osterle, J. F. (1962) 'The Development of Free Convection Between Heated Vertical Plates', *ASME JOURNAL OF HEAT TRANSFER*, 84, pp. 40–44.

Borkink, J. G. H. and Westerterp, K. R. (1992) 'Influence of tube and particle diameter on heat transport in packed beds', *AIChE Journal*, 38(5), pp. 703–715. doi: 10.1002/aic.690380507.

Botao, T., Jie, C., Haijun, W. A. N., Jiqing, L. U., Shaocheng, Z., Ya, L. I. U., Ying, L. I. U., Xiaohui, G. U. O. (2007) 'A Corrected Comprehensive Kinetic Model of Fischer – Tropsch Synthesis', 28(8), pp. 687–695.

Bright Hub Engineering (2010) *The Flat Plate Heat Exchanger in Comparison with Other Types of Heat Exchangers*. Available at: https://www.brighthubengineering.com/hvac/61791-features-and-characteristics-of-the-flat-plate-heat-exchanger/.

Brunner, K. M., Perez, H. D., Peguin, R. P. S., Duncan, J. C., Harrison, L. D., Bartholomew, C. H., Hecker, W. C. (2015) 'Effects of particle size and shape on the performance of a trickle fixed-bed recycle reactor for fischer-tropsch synthesis', *Industrial and Engineering Chemistry Research*, 54(11), pp. 2902–2909. doi: 10.1021/ie503174v.

Bukur, D. B., Pan, Z., Ma, W., Jacobs, G., Davis, B. H. (2012) 'Effect of CO conversion on the Product Distribution of a Co/Al2O3 Fischer-Tropsch Catalyst Using a Fixed Bed Reactor', *Catalysis Letters*.

Caldwell, L. and Vuuren, D. S. Van (1986) 'PHASE IN FISCHER-TROPSCH', 41(1), pp. 89–96.

Chabot, G., Guilet, R., Cognet, P., Gourdon, C. (2015) 'A mathematical modeling of catalytic milli-fixed bed reactor for Fischer-Tropsch synthesis: Influence of tube diameter on Fischer Tropsch selectivity and thermal behavior', *Chemical Engineering Science*, 127, pp. 72–83. doi: 10.1016/j.ces.2015.01.015.

Chandra, V., Vogels, D., Peters E. A. J. F., Kuipers, J.A.M. (2021) 'A multi-scale model for the Fischer-Tropsch synthesis in a wall-cooled packed bed reactor', *Chemical Engineering Journal*. Elsevier B.V., 410(January), p. 128245. doi: 10.1016/j.cej.2020.128245.

Claeys, M. and van Steen, E. (2004) 'Basic studies', in *Studies in Surface Science and Catalysis*. Elsevier, pp. 601–680.

Copelli, S., Croci, S., fumagalli, A., Derudi, M., Rota, R., Barozzi, M. (2016) 'Runaway problems in unsteady state tubular reactors', *Chemical Engineering Transactions*, 53, pp. 85–90. doi: 10.3303/CET1653015.

Davies, I. and Möller, K. P. (2021a) 'Development of a kinetic model for low temperature Fischer-Tropsch synthesis', *Chemical Engineering Science*. Elsevier Ltd, 241, p. 116666. doi: 10.1016/j.ces.2021.116666.

Davies, I. and Möller, K. P. (2021b) 'Development of a kinetic model for low temperature Fischer-Tropsch synthesis', *Chemical Engineering Science*, 241(October). doi: 10.1016/j.ces.2021.116666.

Davis, B. H. and Occelli, M. L. (no date) ‘Fischer-Tropsch Synthesis , Catalysts , and Catalysis’.

Designs, C. (2021) *Plate and Frame Heat Exchanger*. Available at: https://www.csidesigns.com/blog/articles/types-of-heat-exchangers.

Dry, M. E. (2002) ‘The Fischer – Tropsch process : 1950 – 2000’, 71, pp. 227–241.

Emig, G., Holfmann, H., Hofmann, U., Fiand, U. (1980) ‘Experimental Studies on Runaway of Catalytic Fixed-Bed Reactors’, *Chemical Engineering Science*, pp. 249–257.

Ermolaev, V. S., Gryaznov, K. O., Mitberg, E. B., Mordkovich, V. Z., Tretyakov, V. F. (2015) ‘Laboratory and pilot plant fixed-bed reactors for Fischer–Tropsch synthesis: mathematical modeling and experimental investigation’, *Chemical Engineering Science*. Elsevier. doi: 10.1016/j.ces.2015.07.036.

Espinoza, R. L., Steynberg, A. P., Jager, B., Vosloo, A. C. (1999) ‘Low temperature Fischer-Tropsch synthesis from a Sasol perspective’, *Applied Catalysis A: General*, 186(1–2), pp. 13–26. doi: 10.1016/S0926-860X(99)00161-1.

Fernandes, F. A. N. (2005) ‘Polymerization Kinetics of Fischer-Tropsch Reaction on Iron Based Catalysts and Product Grade Optimization’, (8), pp. 930–938. doi: 10.1002/ceat.200500036.

Fernandes, F. A. N. (2006) ‘Modeling and Product Grade Optimization of Fischer - Tropsch Synthesis in a Slurry Reactor’, pp. 1047–1057. doi: 10.1021/ie0507732.

Fogler, H. S. (1999) *Elements of Chemical Reaction Engineering*.

Fratalocchi, L., Visconti, C. G., Groppi, G., Lietti, L., Tronconi, E. (2018) ‘Intensifying heat transfer in Fischer-Tropsch tubular reactors through the adoption of conductive packed foams’, *Chemical Engineering Journal*. Elsevier, 349(May), pp. 829–837. doi: 10.1016/j.cej.2018.05.108.

Froment, G. F. and Bischoff, K. B. (2004) ‘Chemical Reactor Analysis and Design Fundamentals’, *Chemical Engineering Science*, 59(10), pp. 2123–2124. doi: 10.1016/j.ces.2003.12.030.

Geerlings, J. J. C., Wilson, J. H., Kramer, G. J., Kuipers, H. P. C. E., Hoek, A., Huisman, H. M. (1999) ‘Fischer – Tropsch technology — from active site to commercial process’, 186, pp. 27–40.

Glasser, D., Hilderbrandt, D., Liu, X., Lu, X., Masuku, C. M. (2012) ‘Recent advances in understanding the Fischer – Tropsch synthesis (FTS) reaction’, *Current Opinion in Chemical Engineering*. Elsevier Ltd, 1(3), pp. 296–302. doi: 10.1016/j.coche.2012.02.001.

Guettel, R., Kunz, U. and Turek, T. (2008) ‘Reactors for Fischer-Tropsch Synthesis’, *Chemical Engineering & Technology: Industrial Chemistry-Plant Equipment-Process Engineering-Biotechnology*. Wiley Online Library, 31(5), pp. 746–754.

Baten, J. van, Baur, R., Kooijman, H., Taylor, R., Jr., W. M. Barrett ‘cape open to cape open simulation environment’. Available at: https://www.cocosimulator.org/index.html.

Robota, H. J., Richard, L., Doshmukh, S., LeViness, S. (2014) ‘Fischer-Tropsch synthesis in a microchannel reactor: the influence of CO/SiO2 catalyst structure on Fischer-Tropsch synthesis performance', *International Petroleum Technology Conference*.

Van Helden, P., Berg, J. A. V. D., Petersen, M. A., Janse Van Rensburg, W., Ciobica, I. M., Van De Loosdrecht, J. (2017) 'Computational investigation of the kinetics and mechanism of the initial steps of the Fischer-Tropsch synthesis on cobalt', *Faraday Discussions*, 197, pp. 117–151. doi: 10.1039/c6fd00197a.

HFMPHE (2018) *Comparison Between Plate Heat Exchanger And Shell-and-tube Heat Exchanger*. Available at: http://www.hfmphe.com/news/comparison-between-plate-heat-exchanger-and-sh-16511005.html.

Huang, H. and Jaworski, A. (2019) 'Numerical simulation of the effect of plate spacing on heat transfer characteristics within a parallel-plate heat exchanger in a standing wave thermoacoustic system', *E3S Web of Conferences*, 116. doi: 10.1051/e3sconf/201911600028.

Irani, M. (2014) 'Investigating the production of liquid fuels from synthesis gas (CO + H2) in a bench-scale packed-bed reactor based on Fe–Cu–La/SiO2 catalyst: experimental and CFD modeling', *International Journal of Industrial Chemistry*, 5(1), pp. 1–9. doi: 10.1007/s40090-014-0011-y.

Jager, B. and Espinoza, R. (1995) 'Advances in low temperature Fischer-Tropsch synthesis', *Catalysis Today*, 23(1), pp. 17–28. doi: 10.1016/0920-5861(94)00136-P.

Jess, A. (2012) 'Influence of Particle Size and Single-Tube Diameter on Thermal Behavior of Fischer-Tropsch Reactors', (2), pp. 369–378. doi: 10.1002/ceat.201100615.

Jess, A. and Kern, C. (2009) 'Modeling of multi-tubular reactors for Fischer-Tropsch synthesis', *Chemical Engineering and Technology*, 32(8), pp. 1164–1175. doi: 10.1002/ceat.200900131.

Jess, A. and Kern, C. (2012) 'Influence of particle size and single-tube diameter on thermal behavior of Fischer-Tropsch reactors: Part I: Particle size variation for constant tube size and vice versa', *Chemical Engineering and Technology*, 35(2), pp. 369–378. doi: 10.1002/ceat.201100615.

Kaskes, B., Vervloet, D., Kapteijn, F., Ommen, J. R. V. (2016) 'Numerical optimization of a structured tubular reactor for Fischer – Tropsch synthesis', *CHEMICAL ENGINEERING JOURNAL*. Elsevier B.V., 283, pp. 1465–1483. doi: 10.1016/j.cej.2015.08.078.

Kauchali, S., McGregor, C. and Hildebrandt, D. (2000) 'Binary distillation re-visited using the attainable region theory', *Computers & Chemical Engineering*. Elsevier, 24(2–7), pp. 231–237.

Kibby, C., Jothimurugesan, K., Das, T., Lacheen, H. S., Rea, T., Saxton, R. J. (2013) 'Chevron's gas conversion catalysis-hybrid catalysts for wax-free Fischer-Tropsch synthesis', *Catalysis Today*. Elsevier B.V., 215, pp. 131–141. doi: 10.1016/j.cattod.2013.03.009.

Kim, S. H., Anand, N. K. and Fletcher, L. S. (1991) 'Free Convection Between Series of vertical Parallel Plates With Embedded Line Heat Sources', *ASME JOURNAL OF HEAT TRANSFER*, 113, pp. 108–115.

Kshetrimayum, K. S., Jung, I., Na, J., Park, S., Lee, Y., Park, S., Lee, C. J., Han, C. (2016) 'CFD Simulation of Microchannel Reactor Block for Fischer-Tropsch Synthesis: Effect of Coolant

Type and Wall Boiling Condition on Reactor Temperature', *Industrial and Engineering Chemistry Research*, 55(3), pp. 543–554. doi: 10.1021/acs.iecr.5b03283.

Laan, G. P. Van Der (1999) *Kinetics , Selectivity and Scale Up of the Fischer-Tropsch Synthesis*.

Van Der Laan, G. P. and Beenackers, A. A. C. M. (1999) 'Hydrocarbon selectivity model for the gas-solid Fischer-Tropsch synthesis on precipitated iron catalysts', *Industrial and Engineering Chemistry Research*, 38(4), pp. 1277–1290. doi: 10.1021/ie980561n.

Laan, G. P. Van Der and Beenackers, A. A. C. M. (1999) 'Hydrocarbon Selectivity Model for the Gas - Solid Fischer - Tropsch Synthesis on Precipitated Iron Catalysts', pp. 1277–1290. doi: 10.1021/ie980561n.

Laan, G. P. Van Der and Beenackers, A. A. C. M. (2011) 'Kinetics and Selectivity of the Fischer – Tropsch Synthesis : A Literature Review Kinetics and Selectivity of the Fischer – Tropsch Synthesis : A Literature', 4940. doi: 10.1081/CR-100101170.

Van der Laan, G. P., Beenackers, A. A. C. M. and Krishna, R. (1999) 'Multicomponent reaction engineering model for Fe-catalyzed Fischer-Tropsch synthesis in commercial scale slurry bubble column reactors', *Chemical Engineering Science*, 54(21), pp. 5013–5019. doi: 10.1016/S0009-2509(99)00225-0.

Lacroix, M., Dreibine, L., Pham-huu, C., Edourad, D., Savin, S., Luck, F., Schweich, D. (2009) 'Effect of structure and thermal properties of a Fischer – Tropsch catalyst in a fixed bed'. doi: 10.1016/j.cattod.2009.07.058.

Ledakowlcz, S., Nettelhoff, H., Kokuun, R. J., Deckwer, W. D. (1985) 'Kinetics of the Fischer-Tropsch Synthesis in the Slurry Phase on a Potassium Promoted Iron Catalyst', *Industrial and Engineering Chemistry Process Design and Development*, 24(4), pp. 1043–1049. doi: 10.1021/i200031a025.

Lee, T. (2011) *NUMERICAL MODELING AND SIMULATION OF FISCHER-TROPSCH PACKED-BED REACTOR AND ITS THERMAL MANAGEMENT*. University of Florida.

Lee, T. S. and Chung, J. N. (2012) 'Mathematical Modeling and Numerical Simulation of a Fischer − Tropsch Packed Bed Reactor and Its Thermal Management for Liquid Hydrocarbon Fuel Production using Biomass Syngas'. doi: 10.1021/ef201667a.

Levy, E. K. (1971) 'Optimum Plate Spacing for Laminar Natural Convection Heat Transfer From Parallel Vertical Isothermal Flat Plates', *ASME JOURNAL OF HEAT TRANSFER*, 93, pp. 463–465.

Lozano-Blanco, G., Thybaut, J. W., Surla, K., Galtier, P., Marin, G. B. (2006) 'Fischer-Tropsch synthesis: Development of a microkinetic model for metal catalysis', *Oil and Gas Science and Technology*, 61(4), pp. 489–496. doi: 10.2516/ogst:2006026a.

Marine Engineering Study Materials (2014) *Advantages and Disadvantages of Shell and Tube and Plate type Heat Exchangers*. Available at: https://marineengineeringonline.com/advantages-disadvantages-shell-tube-plate-type-heat-exchangers/.

Méndez, C. I., Ancheyta, J. and Trejo, F. (2017) 'Modeling of Catalytic Fixed-Bed Reactors for Fuels Production by Fischer-Tropsch Synthesis', *Energy and Fuels*, 31(12), pp. 13011–13042. doi: 10.1021/acs.energyfuels.7b01431.

Miroliaei, A. R., Shahraki, F., Atashi, H., Karimzadeh, R. (2012) ‘Comparison of CFD results and experimental data in a fixed bed Fischer-Tropsch synthesis reactor’, *Journal of Industrial and Engineering Chemistry*. The Korean Society of Industrial and Engineering Chemistry, 18(6), pp. 1912–1920. doi: 10.1016/j.jiec.2012.05.003.

Moganiwa, B. and Oladiran, M. T. (2016) ‘Developing A 2D CFD Model of A Fixed Bed Reactor For Fischer Tropsch Synthesis On A Promoted Iron Catalyst’, *INTERNATIONAL JOURNAL OF SCIENTIFIC PROGRESS AND RESEARCH (IJSPR)*, 29(01).

Mota, F. A. S., Caravalho, E. P. and Ravagnani, M. A. S. S. (2015) ‘Modeling and Design of Plate Heat Exchanger’, in *Heat Transfer Studies and Applications*. doi: DOI: 10.5772/60885.

Mthombeni, B. (2009) *Modelling Fischer Tropsch Synthesis in two-phase, continuous, well-mixed slurry reactors*. University of Cape Town.

Norval, G. W. (2008) ‘Notes on the Issues of Equilibrium in the Fischer-Tropsch Synthesis’, 86(December), pp. 1062–1069. doi: 10.1002/cjce.20110.

Norval, G. W. and Phillips, M. J. (1990) ‘Application of Equilibrium Analysis to a Fischer-Tropsch Product’, 91, pp. 5–9.

Oberkampf, W. L. and Trucano, T. G. (2002) *Verification and validation in computational fluid dynamics*.

Ostadi, M., Rytter, E. and Hillestad, M. (2016) ‘Evaluation of kinetic models for Fischer–Tropsch cobalt catalysts in a plug flow reactor’, *Chemical Engineering Research and Design*. Institution of Chemical Engineers, 114(September), pp. 236–246. doi: 10.1016/j.cherd.2016.08.026.

Park, N., Kim, J., Yoo, Y., Lee, J., Park, M. (2014) ‘Modeling of a pilot-scale fixed-bed reactor for iron-based Fischer – Tropsch synthesis : Two-dimensional approach for optimal tube diameter’, *FUEL*. Elsevier Ltd, 122, pp. 229–235. doi: 10.1016/j.fuel.2014.01.044.

Patzlaff, J., Liu, Y., Graffmann, C., Gaube, J. (1999) ‘Studies on product distributions of iron and cobalt catalyzed Fischer – Tropsch synthesis’, 186, pp. 109–119.

Paul Mueller Company Engineering Staff (2016) *Which Heat Exchanger Is Best? The Three Main Types Explained...* Available at: https://academy.paulmueller.com/different-heat-exchanger-types.

Rafiq, M. H., Jakobsen, H. A., Schmid, R., Hustad, J. E. (2011) ‘Experimental studies and modeling of a fixed bed reactor for Fischer-Tropsch synthesis using biosyngas’, *Fuel processing technology*.

Raje, A. P. and Davis, B. H. (1996) ‘Effect of Vapor - Liquid Equilibrium on Fischer - Tropsch Hydrocarbon Selectivity for a Deactivating Catalyst in a Slurry Reactor’, (4), pp. 552–560. doi: 10.1021/ef950213n.

Rofer-depoorter, C. K. (1981) ‘A Comprehensive Mechanism for the Fischer-Tropsch Synthesis’, pp. 447–474. doi: 10.1021/cr00045a002.

Rohmah, N., Pikra, G., Purwanto, A. J., Pramana, R. I. (2015) ‘The effect of plate spacing in plate heat exchanger design as a condenser in organic Rankine cycle for low temperature heat source’, *Energy Procedia*. Elsevier B.V., 68, pp. 87–96. doi:

10.1016/j.egypro.2015.03.236.

Saeidi, S., Nikoo, M. K., Mirvakili, A., Bahrani, S., Amin, N. A. S., Rahimpour, M. R. (2015a) 'Recent advances in reactors for low-temperature Fischer-Tropsch synthesis : process intensification perspective', *Reviews in Chemical Engineering*, 31(3), pp. 209–238. doi: 10.1515/revce-2014-0042.

SAVREE (2020) *Plate Heat Exchanger (PHE)*. Available at: https://savree.com/en/encyclopedia/plate-heat-exchanger-phe.

Schulz, H. and Claeys, M. (1999) 'Kinetic modelling of Fischer – Tropsch product distributions', 186, pp. 91–107.

Schulz, H., Steen, E. Van and Claeys, M. (1994) 'Selectivity and mechanism of Fischer-Tropsch synthesis with iron and cobalt catalysts', pp. 455–460.

Schwan, P. (2001) *Transient Analysis of Diffusion and Adsorption under Reaction Conditions*. University of Cape Town.

Sharrock, C. J. and Coetzert, R. (2007) 'Selecting robust kinetic models on noisy data using the bootstrap', *International Journal of Chemical Reactor Engineering*, 5. doi: 10.2202/1542-6580.1479.

Shin, M. S., Park, N., Park, M. J., Cheon, J. Y., Kang, J. K., Jun, K. W., Ha, K. S. (2014) 'Modeling a channel-type reactor with a plate heat exchanger for cobalt-based Fischer-Tropsch synthesis', *Fuel Processing Technology*. Elsevier B.V., 118, pp. 235–243. doi: 10.1016/j.fuproc.2013.09.006.

Sie, S. T. and Krishna, R. (1998) 'Process development and scale up: III. Scale-up and scale-down of trickle bed processes', *Reviews in Chemical Engineering*, 14(3), pp. 203–252. doi: 10.1515/REVCE.1998.14.3.203.

Sparks, D. E., Vallee, S., Jia, Z., Shafer, W. D., Davis, B. H. (2017) 'Fischer-Tropsch synthesis. Evaluation of an aluminum small channel reactor', *Faraday Discussions*. Royal Society of Chemistry, 197, pp. 403–419. doi: 10.1039/c6fd00179c.

van Steen, E., Claeys, M., Möller, K. P., Nabaho, D. (2018) 'Comparing a cobalt-based catalyst with iron-based catalysts for the Fischer-Tropsch XTL-process operating at high conversion', *Applied Catalysis A: General*. Elsevier, 549(September 2017), pp. 51–59. doi: 10.1016/j.apcata.2017.09.019.

Van Steen, E. and Schulz, H. (1999) 'Polymerisation kinetics of the Fischer-Tropsch CO hydrogenation using iron and cobalt based catalysts', *Applied Catalysis A: General*, 186(1–2), pp. 309–320. doi: 10.1016/S0926-860X(99)00151-9.

Subiranas, A. M. (2008) *Combining Fischer-Tropsch Synthesis (FTS) and Hydrocarbon Reactions in one Reactor*.

Tu, J., Yeoh, G.-H. and Liu, C. (2018) *Computational Fluid Dynamics*.

Tumuluri, K. (2018) 'Comparison of Shell and Tube and in Plate Heat Exchanger', *International Journal of Pure and Applied Mathematics*, 116(January).

van Baten, J., Baur R., Kooijman, H., Taylor, R., Jr., W. M. B., (2022) 'cape open to cape open simulation environment'. Available at: https://www.cocosimulator.org/index.html.

Versteeg, H. K. and Malalasekera, W. (2005) *An Introduction to Computational Fluid Dynamics*, *IEEE Concurrency*. doi: 10.1109/mcc.1998.736434.

Vessia O. (2002) ‘Fischer-Tropsch reactor fed by syngas’. Available at: http:/www.zero.no/transport/bio/fischer-tropsch-reactor-fed-by-syngas.

Visconti, C. G., Tronconi, E., Lietti, L., Zennaro, R., Forzatti, P. (2007) ‘Development of a complete kinetic model for the Fischer – Tropsch synthesis over Co / Al 2 O 3 catalysts’, 62, pp. 5338–5343. doi: 10.1016/j.ces.2006.12.064.

Visconti, C. G. (2014) ‘Vapor − Liquid Equilibria in the Low-Temperature Fischer − Tropsch Synthesis’.

Visconti, C. G. and Mascellaro, M. (2013) ‘Calculating the product yields and the vapor – liquid equilibrium in the low-temperature Fischer – Tropsch synthesis’, *Catalysis Today*. Elsevier B.V., 214, pp. 61–73. doi: 10.1016/j.cattod.2012.10.016.

Yadav, A. (2019) ‘A . Hydraulic Mean Depth , Hydraulic Radius and Hydraulic Diameter i . Hydraulic Mean Depth , Hydraulic Radius’, (November).

Yagi, S. and Kunii, D. (1957) ‘Studies on Effective Thermal Conductivities in Packed Beds’, (20), pp. 373–381.

Yang, J., Liu, Y., Chang, J., Wang, Y., Bai, L., Xu, Y., Xiang, H., Li, Y., Zhong, B. (2003) ‘Detailed Kinetics of Fischer - Tropsch Synthesis on an Industrial Fe - Mn Catalyst’, pp. 5066–5090.

Welty, J. R., Wicks, C. E., Wilson, R. E., Rorrer G. L. (2000) *Fundamentals of Momentum, Heat, and Mass Transfer*. 5th edn.

Zhu, X., Lu, X., Liu, X., Hilderbrandt, D., Glasser, D. (2010) ‘Study of Radial Heat Transfer in a Tubular Fischer - Tropsch Synthesis Reactor’, pp. 10682–10688. doi: 10.1021/ie1004527.

Zijlstra, B., Broos, R. J. P., Chen, W., Filot, I. A. W., Hensen, E. J. M. (2020) ‘First-principles based microkinetic modeling of transient kinetics of CO hydrogenation on cobalt catalysts’, *Catalysis Today*. Elsevier, 342(March 2019), pp. 131–141. doi: 10.1016/j.cattod.2019.03.002.

Appendix A

Kinetic Model

Thermodynamic Aspect of the Kinetic Model

Rate determining step is shown to be the hydrogenation of CO to CH_2 (Van Helden *et al.*, 2017 ; Allie and Nyathi, 2019 & Zijlstra *et al.*, 2020). Introduction of the monomer CH_2 allows the FT reactions to be driven by an equilibrium approach (Norval, 2008).

The thermodynamic basis of the ASF distribution is the linear variation of the ideal gas Gibbs free energy of formation with the carbon numbers in the homologous series of n-paraffins and olefins due to the increment of a CH_2 group with each member in both the series (Norval and Phillips, 1990). Hence, the Gibbs free energy for CH_2 can be calculated from the gradient of the linear relationship with carbon number at constant temperature. Calculation of Gibbs energies are required to calculate the equilibrium constants $K_{a,n}$ using equation (A-1). This satisfies criterion 2, together with separate chain growth reactions for paraffins and olefins.

$$K_{a,n} = exp\left(-\frac{\triangle G^{\circ}{}_{rxn,n}}{RT}\right) \tag{A-1}$$

Calculation of Activity of Monomer CH_2

Since the net rate of formation of the monomer CH_2 is equal to zero, this implies that the rate of consumption of CO by the FT reactions only, on a carbon basis, is equal to the rate of formation of organic compounds i.e. the n-paraffines and 1-olefins, as shown in equation (A-2) (Claeys and van Steen, 2004).

$$-r_{CO}{}^{FT} = r_{C,org} \tag{A-2}$$

The rate of CO consumption is equivalent to the rate of reaction step 1 which leads to the monomer formation. Substituting this in equation (A-2) would give us the rate of formation of the monomer equal to the rate of the formation of the organic compounds as shown in equation (A-3)

$$r_{1,CH_2} = r_{C,org} \tag{A-3}$$

It implies that the slow rate of monomer formation is compensated by fast rate of consumption of monomer. This indicates high reactivity of the monomer (Fogler, 1999). The approximation of the pseudo-state is, thus, safe to be applied.

The rate of formation of organic compounds means the sum of the rate of the monomer consumption in methanation, initiation and the formation of n-paraffins and 1-Olefins on a carbon basis as shown in equation (A-4) on a carbon basis.

$$r_{1,CH_2} - r_{C,org} = r_1 - r_2 - r_3 - \sum_{n=2}^{N-1} r_{n+2} - 2\mathrm{r}_{\mathrm{N+2}} - \sum_{\mathrm{n=2}}^{\mathrm{N-1}} \mathrm{r}_{\mathrm{N+n+1}} = 0 \qquad \text{(A-4)}$$

If the rate equations which are expressed in species' partial pressures are substituted in equation (A-4), it would look like equation (A-5)

$$\begin{aligned} k_1\left(a_{CO}{a_{H_2}}^2 - \frac{a_{CH_2}a_{H_2O}}{K_{a,1}}\right) - k_2\left(a_{CH_2}a_{H_2} - \frac{a_{CH_4}}{K_{a,2}}\right) - k_3\left(a_{CH_2}a_{CH_4} - \frac{a_{C_2H_6}}{K_{a,3}}\right) \qquad \text{(A-5)} \\ - \sum_{n=2}^{N-1} k_4\left(a_{CH_2}a_{C_nH_{2n+2}} - \frac{a_{C_{n+1}H_{2(n+1)+2}}}{K_{a,n+2}}\right) \\ - 2\mathrm{k}_5\left({\mathrm{a}_{\mathrm{CH_2}}}^2 - \frac{\mathrm{a}_{\mathrm{C_2H_6}}}{\mathrm{K}_{\mathrm{a,N+2}}}\right) \\ - \sum_{\mathrm{n=2}}^{\mathrm{N-1}} \mathrm{k}_5\left(\mathrm{a}_{\mathrm{CH_2}}\mathrm{aC_nH_{2n}} - \frac{\mathrm{a}_{\mathrm{C_{n+1}H_{2(n+1)}}}}{\mathrm{K}_{\mathrm{a,N+n+1}}}\right) = 0 \end{aligned}$$

a$_i$ represents the partial pressure of specie i. Equation (A-5) is a linear equation in a_{CH_2} and can be solved to find out the partial pressure of CH$_2$.

Appendix B

A CFD simulation consists of three steps:

1. Pre-processor
2. Solver
3. Post-processor

Pre-Processor:

The main parts in the process of pre-processing consists of:

1. Defining of the computational domain which would be the representative of the reactor geometry (region of interest)
2. Grid Generation: Sub-Division of the computational domain into smaller, finite grid of non-overlapping cells
3. Setting up of the physical and chemical processes that need to be included in the kinetic and reactor model
4. Setting up the properties of the fluid used
5. Defining the appropriate mathematical conditions at the boundaries of the cells whose sides form the domain boundary

The equations are solved for the values at nodes of each cell only. Thus, having more nodes in the domain, which would be a result of having a greater number of cells would result in a more accurate solution. But increasing the number of cells makes the simulation computationally expensive. However, after a certain number of cells, the accuracy is unaffected by the number of cells and the mesh is called an independent mesh.

Solver:

There are three different routes that can be taken for solving the governing equations based on the nature of equations and robustness of the solution required: (a) Finite Difference Method (b) Finite Element Method and (c) Finite Volume Method.

Finite Volume Method has been employed for solving the flow equations in the present study. The basic methodology followed for solving equations include:

1. Integration of the governing equations of the fluid flow over all the control volumes
2. Discretisation- CO conversion of the resultant integral equations into a system of algebraic equations
3. Solution of the algebraic equations using an iterative approach

The solution algorithm for CFD is iterative in nature. In a converged solution, the residual quantities which represent the errors in the conservation of the flow characteristics are extremely small quantities.

Post-Processor:

The converged solution thus obtained can be used to display graphics in the form of contours, vectors, surface, graphs, pathlines and animations which can be helpful to understand transient variations in the system (Versteeg and Malalasekera, 2005).

The schematic of the general overview of a CFD model is shown in Figure *B*-1.

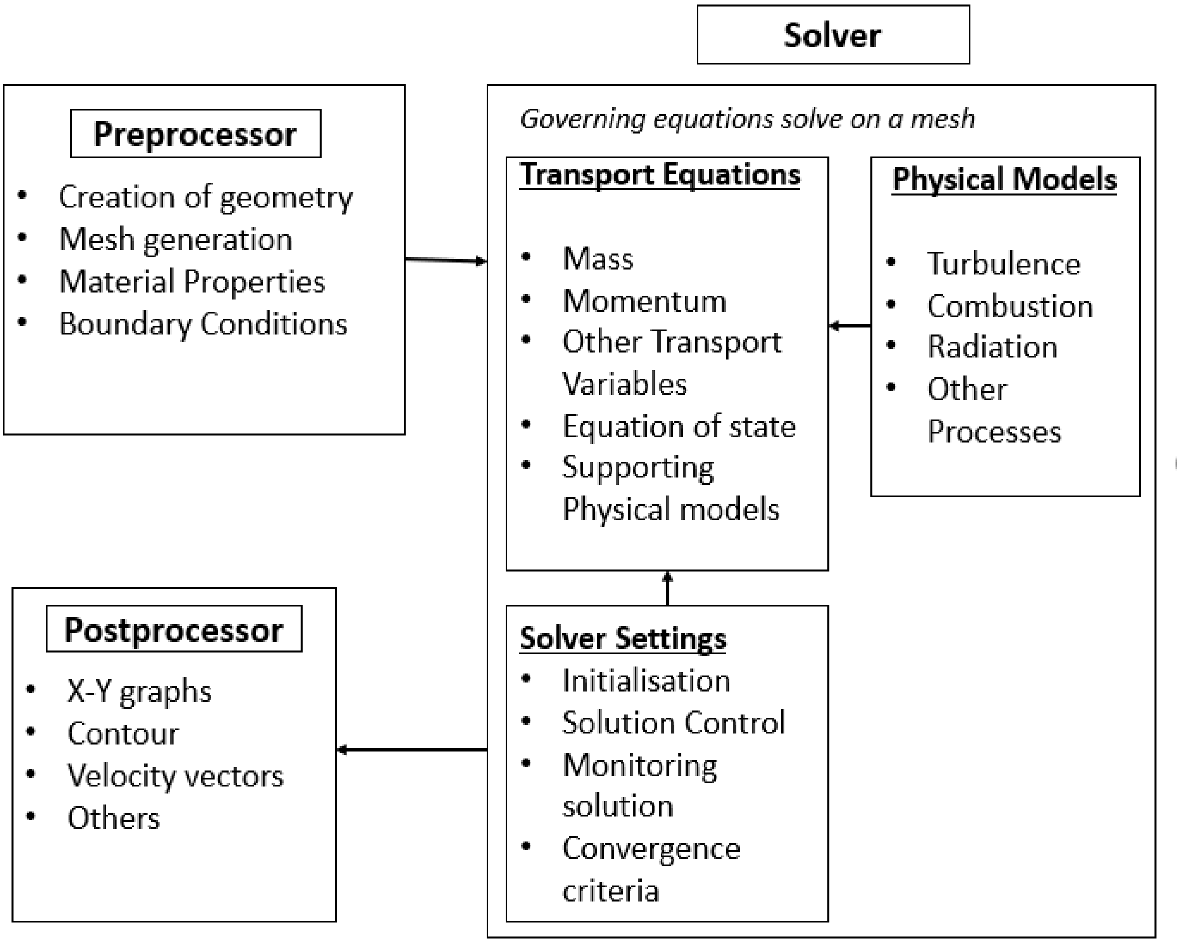

Figure *B*-1 The interconnectivity functions of the three main elements within a CFD analysis framework, reproduced from (Tu, Yeoh and Liu, 2018)

B.1 Conservation Equations

The fundamental equations for the continuum mechanics are based on the conservation laws of:

1. Mass
2. Momentum
3. Energy

The fundamental equations may be arrived at using various discretisation approaches which will be discussed in the section 4.1. This section introduces the fundamental laws of fluid mechanics that form the basis of numerical solution of any CFD simulation.

General Transport Equations

The transport equation describes the transportation of a scalar quantity in space. Generally, it is applied to the transport of a scalar field i.e., concentration, temperature etc. in an incompressible system. Mass, momentum, and energy equations can all be derived from a generalized equation which is based on conservation of any scalar quantity. It is a second order partial differential equation (PDE) given as:

$$\frac{\partial \phi}{\partial t} = \nabla \cdot (D \nabla \phi) - \nabla \cdot (\mathrm{v}\phi) + R \qquad \text{(B-1)}$$

Here ϕ is the variable of interest. It can be mass concentration for mass transfer, temperature for energy transfer, and velocity for momentum transfer. D is the diffusivity coefficient; it can be a mass diffusivity or a thermal diffusivity for heat transport. v is the Velocity field of the scalar quantity. R denotes the source or sinks of quantity c. ∇ represents gradient and $\nabla \cdot$ represents divergence. The term on the LHS is the unsteady term. The first term on the RHS describes the diffusional flux, the second one gives the flux due to advection and the third one is for additional source terms.

B.1.1. Conservation of Mass

The equation for conservation of mass can be derived by substituting ϕ with specific mass i.e., ρ. The general mass balance looks like:

$$\frac{\partial \rho}{\partial t} + \nabla \cdot (\rho u) = 0 \qquad \text{(B-2)}$$

In the Fischer-Tropsch synthesis, syngas is converted to products in the gaseous as well as liquid phases and very little quantities of solid wax. The presence of solid and liquid products has not been taken into account.

B.1.2. Conservation of Momentum

Similar to the continuity equation, the momentum equation for the general mixture model employs mixture properties viz. density and viscosity and mass-averaged velocity defined above.

$$\begin{aligned}\frac{\partial(\rho_m\vec{v}_m)}{\partial t} &+ \nabla.(\rho_m\vec{v}_m\ \vec{v}_m) \\ &= -\nabla p + \nabla.\left[\mu_m\left(\nabla\vec{v}_m + \nabla\vec{v}_m^{\,T}\right)\right] + \rho_m\vec{g} + \vec{F} + \nabla.\left(\sum_{k=1}^{n}\alpha_k\rho_k\vec{v}_{dr,k}\right)\end{aligned} \tag{B-3}$$

Here $\vec{F}$ denotes a momentum source or sink term due to packed bed.

B.1.3. Conservation of Species

The mass balance for a particular specie is given by:

$$\frac{\partial(\rho_k\chi_k Y_{k,i})}{\partial t} + \nabla\cdot(\rho_k\chi_k\overrightarrow{v_k}Y_{k,i}) = -\nabla\cdot\chi_k\vec{J}_{k,i} + \sum_j \Re_j\gamma_{ji}M_{W,ji} \tag{B-4}$$

Where $Y_{k,i}$ is the mass fraction of the ith chemical species. $\vec{J}_{k,i}$ denotes the diffusional flux of the ith species due to the concentration gradients, $\Re_j$ represents the reaction rate for jth reaction, γ_{ji} and $M_{W,ji}$ denote the stoichiometric coefficient and molecular weight, respectively. N-1 species transport equations are solved if N is the total number of species.

Appendix C

Solver Type

C.1 Density Based Approach

The density-based solver solves the governing equations of continuity, momentum, and species transport simultaneously and the other scalars like turbulence are solved afterwards sequentially in a segregated manner. The overview of the procedure shown in Figure C.1 is repeated in every iteration.

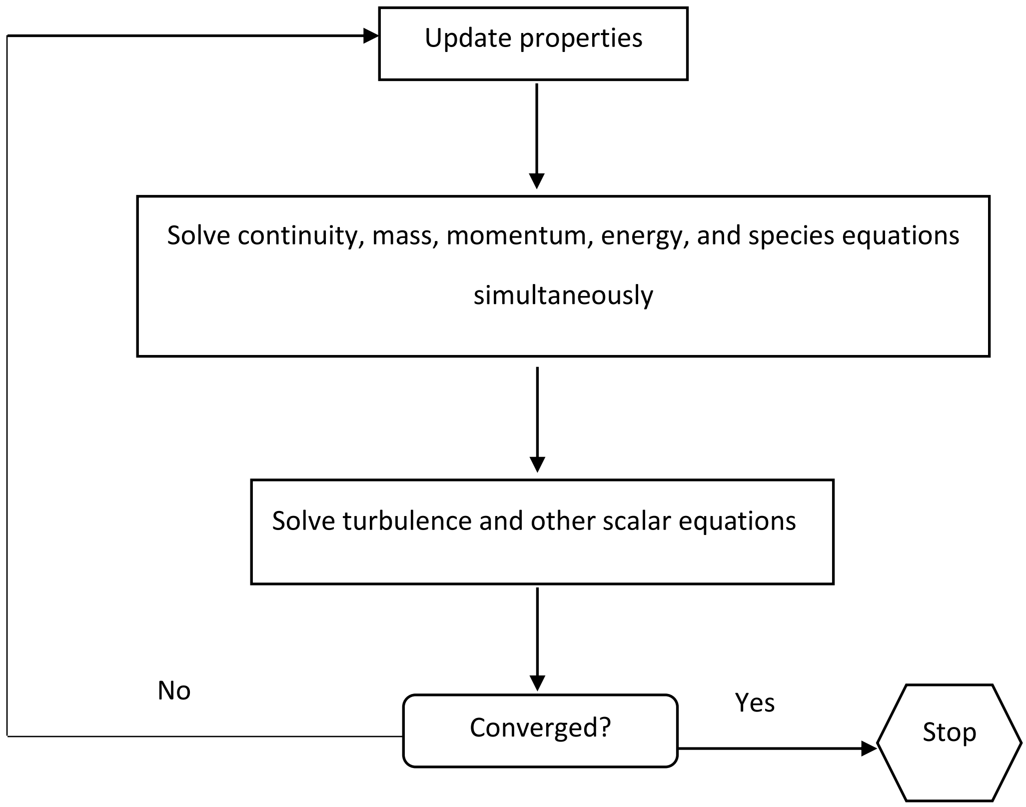

Figure C.1 Overview of density based approach, reproduced from (Ansys, 2013)

C.2 Pressure Based Approach

Pressure-based approach solves the pressure correction equation (D-4) to satisfy the continuity equation. Figure C.2 shows the solution procedure for the pressure-based approach for segregated as well as coupled method.

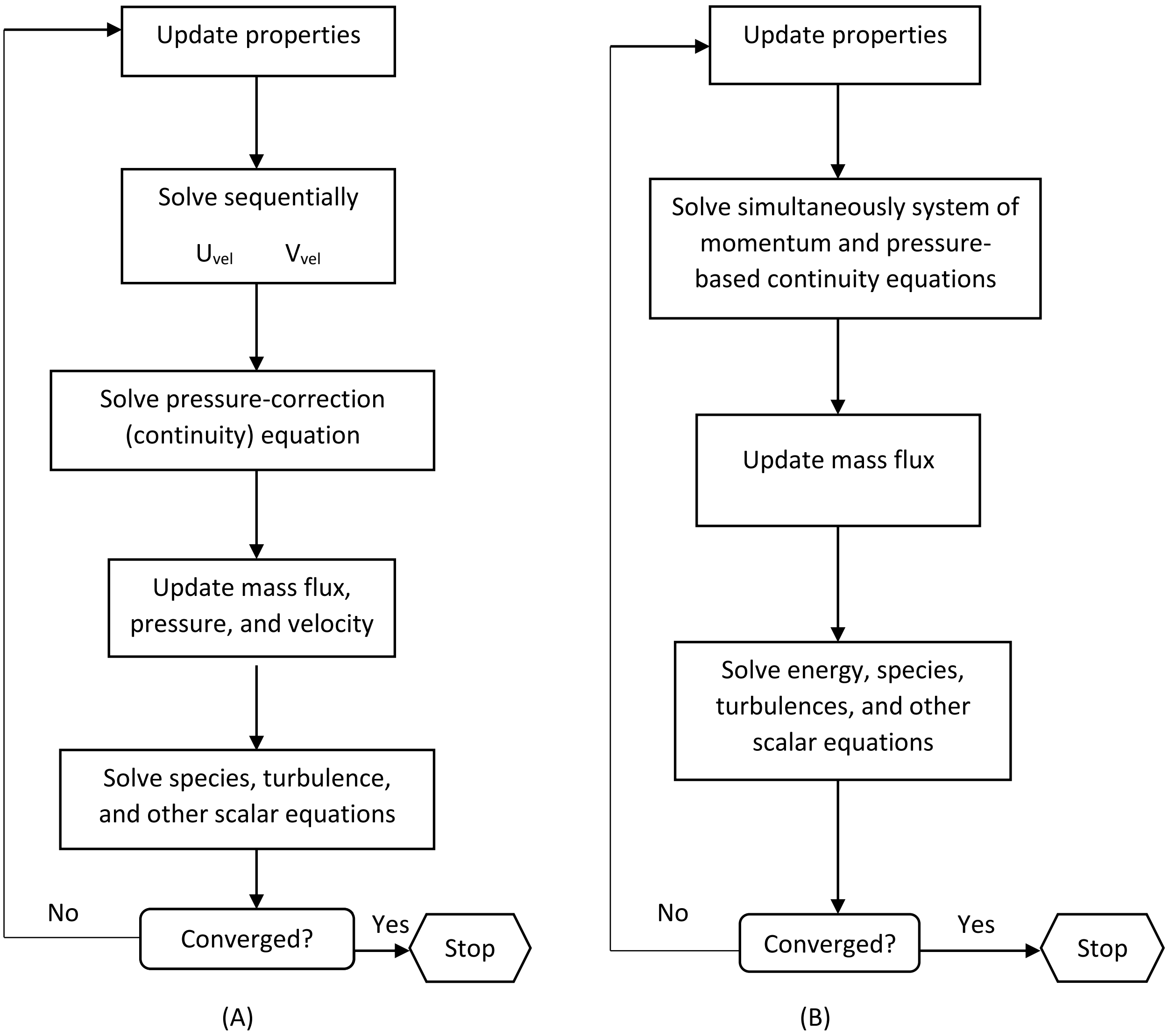

Figure C.2 (A) Pressure-based segregated Algorithm (B) Pressure based coupled Algorithm

U_{rel} and V_{rel} represent the velocities in the x-axis and y-axis respectively.

Appendix D

Finite Volume Method & Initialisation

D.1 Finite Volume Method

In this approach, the fluid flow is divided into several control volumes and mathematical expressions are developed for each control volume. This method involves integrating the transport equation for each control volume which results in a discrete equation that expresses the governing equations on a control volume basis.

A scalar transport equation for a variable ϕ is discretised here for an example. The integral form for any arbitrary control volume *V* is:

$$\int_V \frac{\partial \rho\phi}{\partial t} dV + \oint \rho\phi\vec{v} \cdot d\vec{A} = \oint \Gamma_\phi \nabla \phi \cdot d\vec{A} + \int_V S_\phi dV \tag{D-1}$$

where

ρ = density

$\vec{v}$ = velocity vector (= $u\hat{\imath} + v\hat{\jmath}$ in 2D)

$\vec{A}$ = surface area vector

Γ_ϕ = diffusion coefficient for ϕ

$\nabla \phi$ = gradient of ϕ = $(\partial\phi/\partial x)\vec{\imath} + (\partial\phi/\partial y)\vec{\jmath}$ in 2D

S_ϕ = source of ϕ per unit volume

The discretised version of equation (D-1) would yield:

$$\frac{\partial \rho\phi}{\partial t} V + \sum_{f}^{N_{faces}} \rho_f \overrightarrow{v_f} \phi_f \cdot \overrightarrow{A_f} = \sum_{f}^{N_{faces}} \Gamma_\phi \nabla \phi_f \cdot \overrightarrow{A_f} + S_\phi V \tag{D-2}$$

where

N_{faces} = number of faces enclosing a cell

ϕ_f = value of ϕ convected through face f

$\rho_f \overrightarrow{v_f} \cdot \overrightarrow{A_f}$ = mass flux through the face

$\overrightarrow{A_f} = area\ of\ face, |A|\ (= |A_x\hat{\imath} + A_y\hat{\jmath}|\ in\ 2D)$

$\nabla\ \phi_f = gradient\ of\ \phi\ at\ face\ f$

V = cell volume

$\frac{\partial\rho\phi}{\partial t}V$ is defined in temporal discretisation. Since the model in this project was solved for a steady state solution, $\frac{\partial\rho\phi}{\partial t}V$ term was abolished as per the steady state assumption. A 2D cell in Figure D-1 is an example of the control volume.

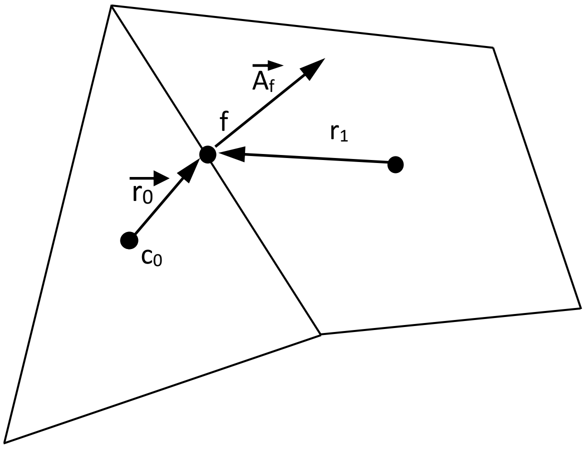

Figure D-1 A control volume showing discretisation of a scalar transport equation, reproduced from (Ansys, 2013)

Equation (D-2) contains the unknown scalar variable ϕ defined at the cell centers and the corresponding neighbouring values in surrounding neighbour cells. A linearised form of equation (D-2) is:

$$a_{P\phi} = \sum_{nb} a_{nb}\phi_{nb} + b \tag{D-3}$$

here nb represents neighbouring cells, and a_P and a_{nb} are the linearized coefficients for ϕ and ϕ_{nb}. Fluid is treated as a continuum, where properties such as density, pressure, velocity etc., are defined as averages over fluid elements, neglecting the behaviour of individual molecules.

The resulting statements express the (exact) conservation of relevant properties for each finite size cell. This clear relationship between the numerical algorithm and the underlying physical conservation principle forms one of the main attractions of the finite volume method and makes its concepts much simpler to understand than the finite element and spectral methods. The conservation of a general flow variable, e.g., a velocity component or enthalpy, within a finite control volume can be expressed as a balance between the various processes tending to increase or decrease it.

The underlying physical phenomena namely, convection and source terms make the PDEs complex and non-linear, so an iterative solution approach is required. The most popular solution procedures are by the TDMA (tri-diagonal matrix algorithm) line-by-line solver of the algebraic equations and the SIMPLE algorithm to ensure correct linkage between pressure and velocity.

PV Coupling

SIMPLE

In the SIMPLE approach, the initial pressure field is guessed (the values specified during initialising the solution) p^*, and the momentum equation is solved using it. This enables calculating the mass flux $J_f{}^*$ from the equation. The calculated flux $J_f{}^*$ does not satisfy the continuity equation (B-2) and, hence, a correction term $\mathrm{J_f}'$ is added to the face flux $\mathrm{J_f}^*$ so that the corrected face flux, $\mathrm{J_f}$ satisfy es the continuity equation. According to the SIMPLE algorithm, $\mathrm{J_f}'$ is postulated to be

$$\mathrm{J_f}' = \mathrm{d_f}(\mathrm{p_{c0}}' - \mathrm{p_{c1}}') \quad \text{(D-4)}$$

where p' is the cell pressure correction.

The algorithm substitutes the flux into the continuity equation to obtain the pressure correction term p’ in the cell. The SIMPLE approach was chosen to obtain a robust solution while also taking care of the mesh skewness.

D.2 Initialisation

There are two main methods by which initial fields can be defined in Ansys Fluent:

1. Standard Initialisation
2. Hybrid Initialisation

Standard Initialisation

Standard Initialisation allows the flow field to be set using the values set as boundary conditions for any zone. All the values are computed and updated for all the variables in all the cells. The field variables can also be manually initialised by specifying the values by the user.

Hybrid Initialisation

Hybrid initialisation iterates the initial solution for a very coarse version of the actual mesh. It produces the velocity and pressure fields using the Laplace equation. This generated pressure field connects the extreme pressure values in a smooth manner. The temperature field and the turbulent fields are initialised to the domain averaged constant values. The species fractions are initialised based on the inlet boundary condition values.

Appendix E

Numerical Simulation

Figure E-1 gives an overview of the methodology that is followed in solving each iteration.

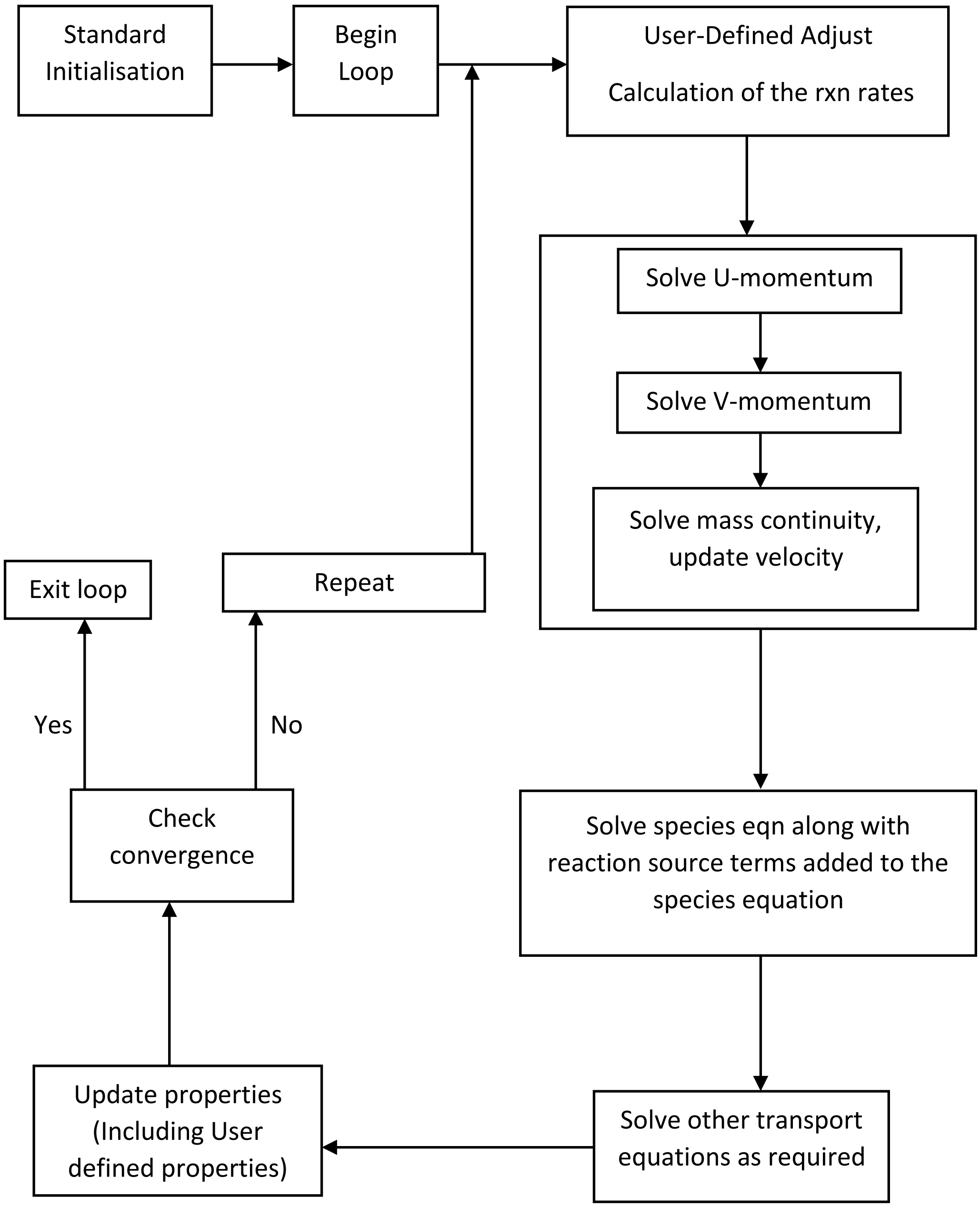

Figure E-1 Block flow diagram of model development procedure

The solution process for the pressure-based segregated solver begins with the standard initialisation process as described in Appendix C. The initialisation is executed outside of the iteration loop.

Every iteration begins with the execution of DEFINE ADJUST UDFs. All the reaction rates are calculated based on the instanteous inputs from the solution process for each iteration. The momentum equations for u, v velocities are solved next in the sequential manner. Thereafter, the species equation is solved. This is where the DEFINE_VR_RATE UDF get implemented for each reaction and the source term for each specie is added to corresponding specie conservation equation. The properties are updated after the conservation equations are solved. A check for convergence is done and the loop either continues or stops based on the convergence condition. Once the data is obtained for a particular iteration, the next iteration imports the values from the previous iteration and the process continues.

Appendix F

The kinetic model used in this project has been imported from the work of Davies and Möller, 2021. Originally in the work of Davies and Möller, it was developed for 160+ species including 80 paraffins and 80 olefins using a software Scilab. The model showed excellent compliance with experimental results present in the literature. It could produce the product distribution described by the ASF distribution and could also overcome the shortcomings of the ASF distribution model by accounting for the deviations observed in the product distribution described by ASF distribution. The product distribution obtained by this kinetic model is described in detail in the work of Davies and Möller.

The 2D CFD model developed in the current project has 40+ species and is quite complex compared to the 1D model of Davies and Möller, former being a CFD model. It is difficult to include more species and therefore, this model was reproduced as a 1D model on Scilab with 160+ species including 80 paraffins and 80 olefins to study the effect of series truncation on the product distribution. *Figure* F-1, *Figure F-2* and *Figure F-3* show the product distribution for paraffins and olefins individually as well as collectively.

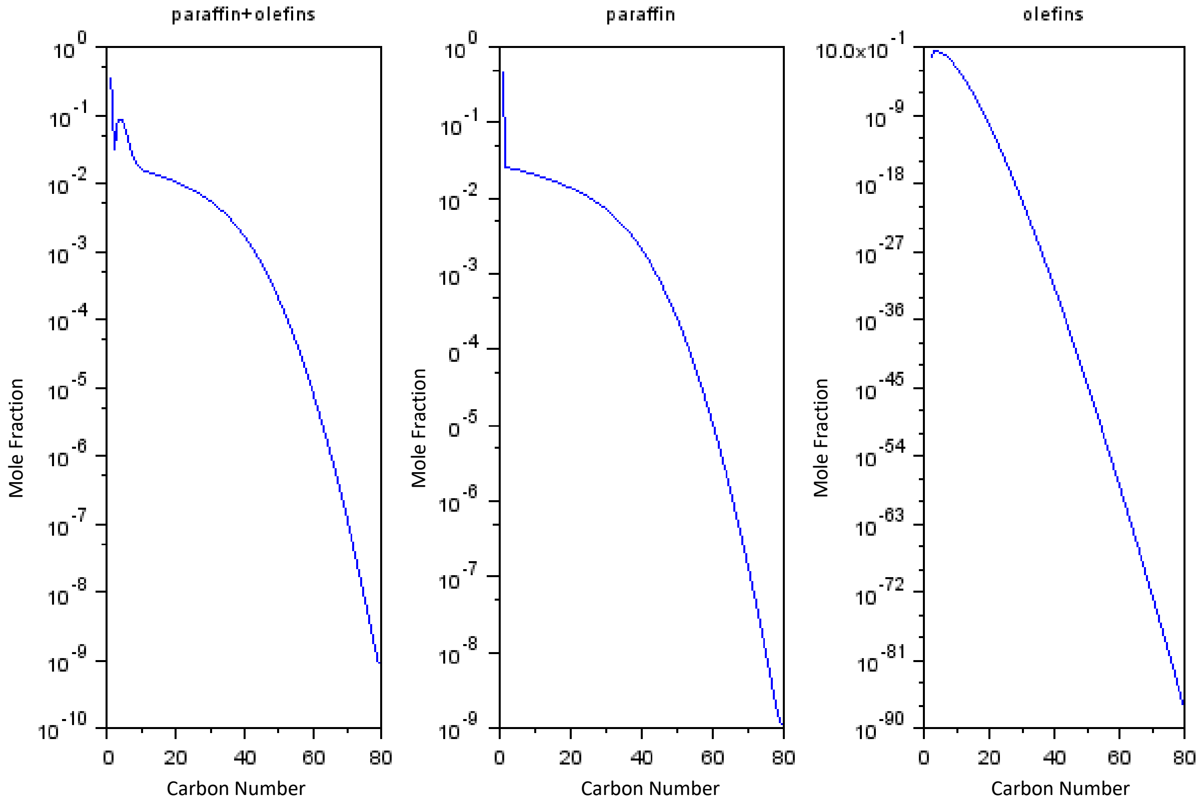

Figure F-1 Product distribution for paraffins and olefins with n = 80

Figure F-1 shows the product distribution for n = 80, where n is an index to denote the number of members in each of the homologous series for Paraffins and Olefins. Figure F-2 is a cropped version of *Figure F-1,* zoomed in to show the first 20 species of the spectrum for paraffins and olefins. Figure F-3 shows the product distribution for n = 20. However, comparing Figure F-2 and Figure F-3 shows clear differences in the patterns for product distribution for paraffins as well as olefins near the upper end of the homologous series. This indicates that the behavior of product distribution of the current model is dependent on n and that truncation does affect the product distribution. Since, in a real FT reactor, the formation of species in the homologous series occurs in a continuum and the species' mole fractions are supposed to decrease asymptotically to zero, breaking the series abruptly at C_{20} in the computational model might lead to increased concentrations of the upper end species, representing the accumulated infinite tail of the series, which got diminished at C_{20}.

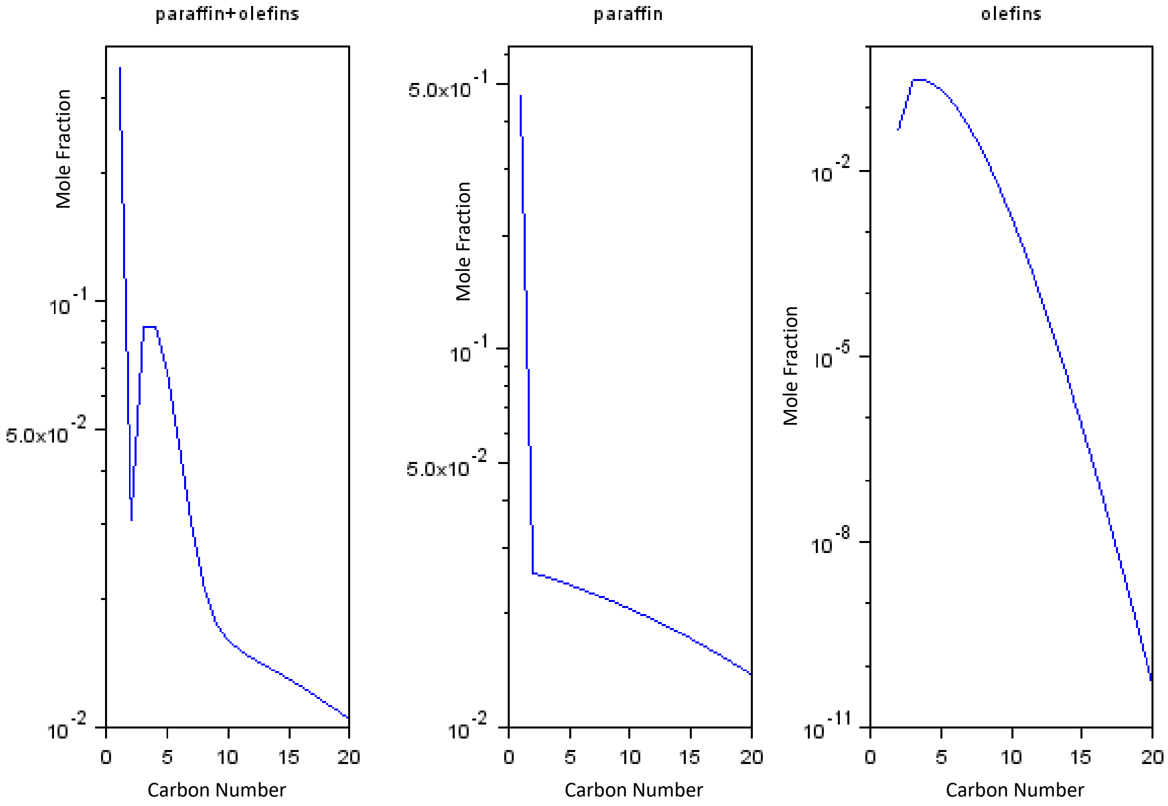

Figure F-2 Product distribution of paraffins and olefins with n= 80, zoomed in to show 20 species

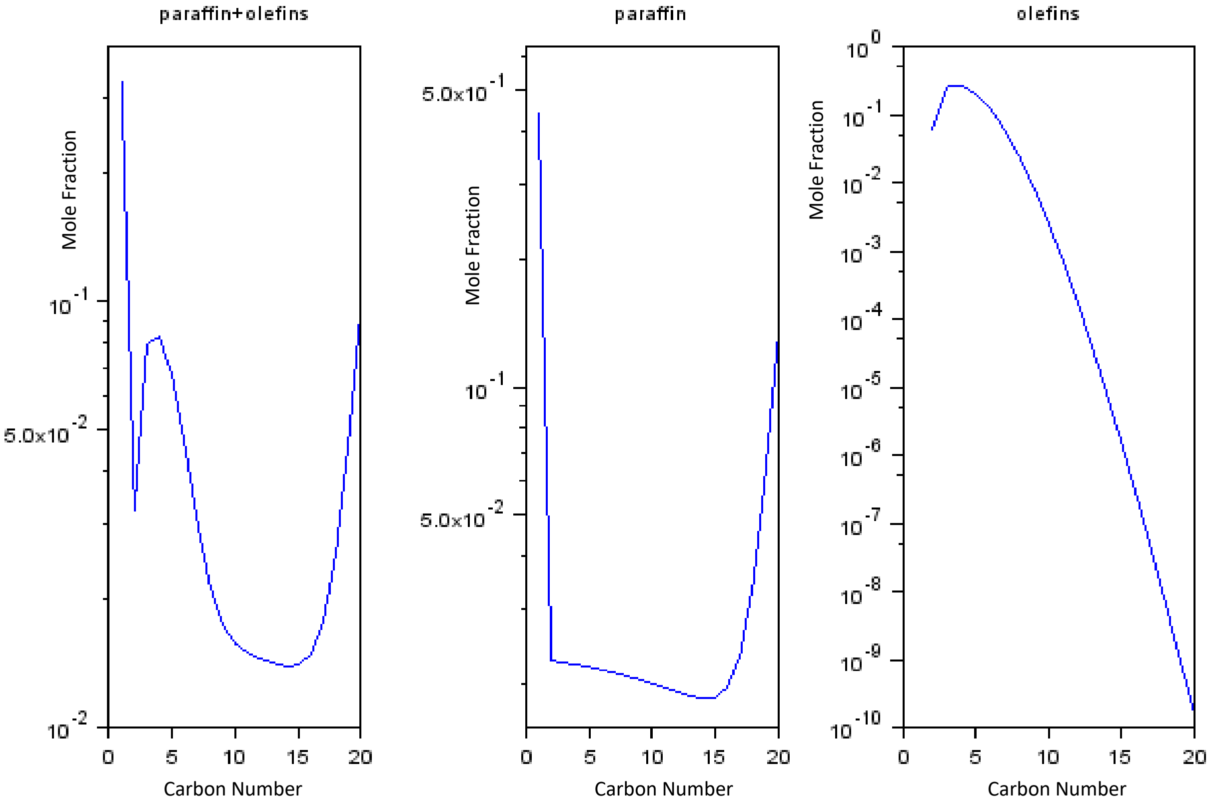

Figure F-3 Product distributions of Paraffins and Olefins for n = 20

Therefore, it can be concluded that the truncating the series at n= 20 produces deviations when compared to the product distribution described by ASF model. However, including more species would complicate the current CFD model and is beyond the scope of this project.

The viability of this kinetic model has already been proven in the work of Davies and Möller, 2021. Even though the current CFD model has n = 20, it serves as a prototype and can always be expanded to include more species and represent a more realistic product distribution. However, since the truncation does not affect other aspects of the reactor, it can be used to demonstrate the effect of geometry and steam temperature on the reactor performance.

Appendix G

Calculation of Heat Transfer Coefficient for a Tube reactor using the CFD Model

According to Newton's law of cooling, heat flux due to convection at a point is given by equation (G-1)

$$\dot{Q} = h * A * (T_{bulk} - T_{steam}) \tag{G-1}$$

The heat transfer coefficient for the entire tube for heat transfer from the reacting mixture to the surroundings is described in equation (G-2)

$$h = \frac{\int \dot{Q} dz}{\int A * (T_{bulk} - T_{steam}) dz} \tag{G-2}$$

$$h = \frac{\int \dot{Q} dz}{\int T_{bulk} * A dz - \int T_{steam} * A dz} \tag{G-3}$$

The overall heat transfer coefficient (from the reacting mixture to the coolant steam) used in COCO was calculated from Ansys using the formula in equation (G-3). Numerator on the R.H.S. of (G-3) was taken to be the surface Integral of the heat flux for the catalyst zone only. The integral value gives the amount of heat getting dissipated through the catalyst zone to the coolant steam. T_{bulk} was taken to be the volume averaged integral of temperature for the catalyst zone. Volume integral of Temperature represents the bulk temperature of the catalyst zone. The volume in Ansys is assumed by taking 1m of reference length into the plane as explained in Chapter 4. T_{steam} denotes the steam temperatures used for different simulations. A denotes the surface area of the catalyst zone available for heat dissipation. The calculations are shown in Table G-1.

Table G-1 Calculation of Overall Heat transfer coefficients at different steam temperatures

Steam Temp (°C)	Surface Integral of Heat Flux, $\dot{Q}$ (w)	Volume Integral of Temperature , T_{bulk} (K)	ΔT = Volume Integral Temp - Steam Temp $(T_{bulk} - T_{steam})$ (K)	Area, A (m2)	Integral of Heat Flux /Area, $\dot{Q}$/A (w/m2)	Heat Transfer Coefficient , h (w/m2.k)
200	5242.35	473.65	0.50	1.51	3478.20	6917.66
220	9417.74	494.04	0.89	1.51	6248.50	7051.68
240	13463.96	514.35	1.2	1.51	8933.09	7458.54

Calculation of Heat Transfer Coefficients for Tube and Plate reactors for the Parametric Study

Table G-2 and Table G-3 show the calculation of the heat transfer coefficients for the tube and plate reactor respectively.

Table G-2 Calculation of heat Transfer Coefficient for a Tube reactor from the CFD Model

Tube Radius	Integral of Heat Flux (w)	Volume-weighted average	Steam Temperature (K)	ΔT = Volume Integral Temp - Steam Temp (K)	Area(m2)	Integral of Heat Flux /Area (w/m2)	Heat Transfer Coefficient (w/m2.k)
0.03	21564.75	494.81	493.15	1.65	2.26	9538.55	5758.25
0.04	39110.09	495.67	493.15	2.52	3.01	12974.42	5142.66
0.05	62584.6	496.72	493.15	3.57	3.76	16609.5	4651.87
0.06	92816.96	498.03	493.15	4.88	4.52	20527.46	4202.57
0.07	130938.6	499.64	493.15	6.49	5.27	24821.54	3823.52
0.08	179660.8	501.68	493.15	8.53	6.03	29800.42	3492.62

The heat flux value reported from Ansys was for one wall. Therefore, for a plate reactor in Table G-3, unlike tube reactor in Table G-2, double the value of surface integral of the heat flux has been used, as there are two plates. Similarly, the area A calculated in Table G-3 was also calculated for 2 plates.

Table G-3 Calculation of heat Transfer Coefficient for a Plate reactor from the CFD Model

Plate Spacing	Integral of Heat Flux (w)	2 x Integral of Heat Flux (w)	Volume-weighted average Temperature	Steam Temperature (K)	ΔT = Volume Avg. Temp - Steam Temp (K)	Area (m2)	Integral of Heat Flux /Area (w/m2)	Heat Transfer Coefficient (w/m2.k)
0.03	113928.6	227857.2	494.61	493.15	1.46	24	9494.05	6494.77
0.04	152614.1	305228.2	495.30	493.15	2.15	24	12717.84	5911.43
0.05	196333.9	392667.8	496.06	493.15	2.91	24	16361.16	5616.79
0.06	240684.9	481369.8	497.01	493.15	3.86	24	20057.08	5191.83
0.07	287856.9	575713.8	498.12	493.15	4.97	24	23988.08	4821.92
0.08	338527.2	677054.4	499.42	493.15	6.27	24	28210.6	4497.22
0.09	393988.2	787976.4	500.95	493.15	7.80	24	32832.35	4207.28
0.1	459527.2	919054.4	502.86	493.15	9.71	24	38293.93	3942.22

Appendix H

Comparison between the tube reactor and the plate reactor was carried out based on two criteria given below. The radius and the length of the tube reactor is denoted by r_t and L respectively. For the plate type reactor, the spacing between the plates is denoted by t and the length of the plates is L. L is same for both the reactors as mentioned in chapter 4. The width for the plate type reactor is 1m into the plane as explained in Chapter 4.

To be able to compare the heat transfer capabilities of two geometries, the two most important factors are the fluid flow properties and the surface area available for heat dissipation. A prominent role is played by a non-dimensional number, Reynolds Number (Re), in predicting the flow regime of a fluid flow. Technically, it is described as the ratio of inertial to viscous forces in a fluid flow. It indicates if the fluid flow is laminar or turbulent which in turn affects the heat transfer properties.

For a packed bed, Re depends on the flow superficial velocity, density, viscosity, porosity, and particle diameter. For a given fluid of density ρ_f and viscosity μ which is flowing with a superficial velocity $\overrightarrow{v_s}$ around particles of diameter d_p, Re at a point is given by equation (H-1).

$$Re = \frac{\rho_f * \overrightarrow{v_s} * d_p}{\mu(1-\varepsilon)} \tag{H-1}$$

Since all the parameters density ρ_f, viscosity μ, superficial velocity $\overrightarrow{v_s}$, particle diameter d_p, and porosity ε in equation (H-1) are identical for both the geometries, the Reynolds number for both geometries are going to be equal at every point.

However, having equal Reynolds number for two geometries does not mean having identical fluid flow behaviour. Even though Re is equal for the tube and the plate geometry, the difference in the shape of the reactor will arise differences in the fluid flow patterns. Equal Re will just ensure that the fluid flow in both geometries have same flow regimes (Li, 2004).

For comparing two reactors with different geometries but with similar fluid flow regimes, the volume available for heat generation along with the surface area available for heat dissipation are important factors to consider. Since the volume as well as the surface areas are different for both the geometries, the heat dissipation surface area per unit heat generating volume was equated for both the reactors for comparison.

Equating the heat dissipation Surface Area per unit heat generating Volume

The heat dissipation surface area per unit heat generating volume for the plate type reactor is given by equation (H-2)

$$\frac{surface\ area\ of\ 2\ plates}{Total\ Volume\ of\ plate\ reactor} = \frac{2 * L * 1}{t * L * 1} \tag{H-2}$$

The heat dissipation surface area per unit heat generating volume for the tube reactor is given by equation (H-3)

$$\frac{surface\ area\ of\ tube}{Total\ Volume\ of\ tube\ reactor} = \frac{2 * \Pi * r_t * L}{\Pi * {r_t}^2 * L} \tag{H-3}$$

For having equal surface per unit volume, the expressions in equation (H-2) and equation (H-3) need to be equated as shown in equation (H-4).

$$\frac{2 * L * 1}{t * L * 1} = \frac{2 * \Pi * r_t * L}{\Pi * {r_t}^2 * L} \tag{H-4}$$

$$\frac{2}{t} = \frac{2}{r_t} \tag{H-5}$$

$$r_t = t \tag{H-6}$$

The plate spacing t should be equal to the tube radius or half the pipe diameter according to Equation (H-6).

This condition also ensures equal hydraulic diameters for the two geometries, provided the plate spacings are much smaller than plate width. This condition holds true for the current project. A hydraulic diameter is used to calculate many quantities in the same way as for a round tube for non-circular channels. Following section shows how the same condition is obtained when the hydraulic diameters for the two geometries are equated.

Equating the Hydraulic Radius of the two geometries

Hydraulic Diameter, D_H, is a commonly used term when handling flow in non-circular tubes and channels. The hydraulic diameter transforms non-circular ducts into pipes of equivalent diameter. If the cross-sectional area remains uniform, Hydraulic diameter for a non-circular channel is given by equation (H-7) (Yadav, 2019)

Hydraulic Diameter = 4 x Cross-sectional Area (A) / Wetted Perimeter (P)

$$D_h = \frac{4 * A}{P} \tag{H-7}$$

Wetted Perimeter as the name suggests, denotes the total length of the cross-sectional perimeter that comes in direct contact with the fluid or 'gets wetted' by the fluid. Since in the current project, the fluid flow was assumed to cover the entire cross-section for both the tube as well as the plate, the wetted perimeter was taken to be the entire perimeter of the cross-section.

The hydraulic diameter for the tube reactor is the tube diameter. The hydraulic diameter for the plate reactor can be calculated using the formula mentioned in equation (H-7) as shown in equation (H-8)

$$D_H = \frac{4 * t * 1}{2 * (t + 1)} \tag{H-8}$$

The plate spacing t is much smaller compared to 1, t<<1 as mentioned in Chapter 4. This condition reduces equation (H-8) to equation (H-9)

$$D_H = \frac{4 * t * 1}{2 * 1} \tag{H-9}$$

$$D_H = 2 * t \tag{H-10}$$

$$r_H = t$$

Hence, taking t = r as given in in equation (H-6) also equates the hydraulic diameters of the two geometries.